5-17-2014

Electron Impact Excitation-Cavity Ringdown Spectroscopy

Peeyush Sahay

Electron impact excitation-cavity ringdown spectroscopy

By

Peeyush Sahay

A Dissertation
Submitted to the Faculty of
Mississippi State University
in Partial Fulfillment of the Requirements
for the Degree of Doctor of Philosophy
in Engineering with an Emphasis in Applied Physics
in the Department of Physics and Astronomy

Mississippi State, Mississippi

December 2013

Electron impact excitation-cavity ringdown spectroscopy

By

Peeyush Sahay

Approved:

_____

Chuji Wang
(Major Professor)

_____

David L. Monts
(Committee Member)

_____

Henk F. Arnoldus
(Committee Member)

_____

Matthew J. Berg
(Committee Member)

_____

Robert B. Reese
(Committee Member)

_____

Achille Messac
Dean
James Worth Bagley College of Engineering

Name: Peeyush Sahay

Date of Degree:December 14, 2013

Institution: Mississippi State University

Major Field: Engineering with an Emphasis in Applied Physics

Major Professor: Dr. Chuji Wang

Title of Study: Electron impact excitation-cavity ringdown spectroscopy

Pages in Study: 152

Candidate for Degree of Doctor of Philosophy

Electron impact excitation phenomena play an important role in atomic and molecular physics. The different energy levels of an atom or molecule interact differently with incoming electrons with different energies and that affects the excitation of the energy levels of the atoms and molecules. Studies involving electron impact excitation process are generally conducted with optical emission techniques or by the electron energy loss method. In the present study, for the first time, cavity ringdown spectroscopy (CRDS) has been used to investigate electron impact excitation phenomena of electron-atom collision processes. The technique, i.e., electron impact excitation-cavity ringdown spectroscopy (EIE-CRDS), was employed for the purposes of fundamental study and of real-time applications. The fundamental study which was carried out in terms of determining electron impact excitation cross section (EIECS) has been demonstrated by measuring EIECS of a few excited levels of mercury (Hg) atom. For the application side, the EIE-CRDS technique has been employed for trace element detection.

This dissertation first describes the fundamentals of electron impact excitation-cavity ringdown spectroscopy (EIE-CRDS); afterwards its applications are demonstrated.

A novel method of measuring excitation cross sections using this EIE-CRDS technique has been explained. In this method, first the excitation of atoms are achieved by electron impact excitation process, subsequently, CRDS measured absolute number density is utilized to determine the absolute EIECS values. Steps of the method are described in detail. Applicability of the method is demonstrated by measuring EIECS of three different energy levels of Hg, namely 6s6p $^3P_0$, 6s6p $^3P_1$, and 6s7s $^3S_1$, and the obtained values are in agreement with those reported in the literature.

Secondly, the EIE-CRDS technique was employed to investigate the absorption spectrum of mercury atom in the vicinity of 404.65 nm, corresponding to the transition 6s7s $^3S_1$ → 6s6p $^3P_0$ levels of mercury. Elemental mercury was measured using a laser of wavelength 404.65 nm. The technological feasibility of developing a portable size instrument for mercury detection was explored. Subsequently, a portable size, dual-mode, plasma-CRDS based prototype instrument, capable of real-time trace element monitoring, was developed. The design, functioning, and specifications of the instrument are also explained.

DEDICATION

To my Family

ACKNOWLEDGEMENTS

I would like express my deepest gratitude to Prof. Chuji Wang for giving me opportunity to pursue PhD research under his supervision. Throughout my work he provided constant support, and was always available for any professional and personal guidance. Discussions with him were quite valuable, and I learned a lot working under his supervision.

In addition, I would like to extend my gratitude to my committee members, Dr. David L. Monts, Dr. Henk F. Arnoldus, Dr. Matthew J. Berg, and Dr. Robert B. Reese, for their valuable suggestions time to time. They all were always available for discussion and guidance. Their suggestions helped me significantly in my research work.

I would also like to thank Dr. Susan T. Scherrer, who as a senior colleague helped me lot all through my PhD work. I am also thankful to my lab members with whom I had a good time in all these years.

TABLE OF CONTENTS

LIST OF TABLES

LIST OF FIGURES

CHAPTER I

INTRODUCTION

1.1 Introductory Background

Electron impact excitation (EIE) plays an important role in electron-atom collision processes and has always remained an area of interest of study. Natural phenomena, such as lightning, polar auroras, coronas, etc., occur as a result of electron impact excitations of different gases present in the atmosphere, followed by spontaneous emissions which result in beautiful colors. Similarly, utilities, such as incandescent bulbs, low pressure fluorescent lamps, and the higher pressure arc lamps all work on the principles of electron impact excitation processes. In such instruments, gaseous atoms are housed in a closed environment, known as discharge tube. The electron-atom collision process is triggered by applying voltages across two electrodes mounted inside the tube. Inside the discharge tube, energetic electrons collide with atoms and excite them to higher energy levels; when the excited atoms de-excite to lower energy levels, photons of different wavelengths (colors) that are characteristic of the enclosed gaseous atoms, are emitted. The Figure 1.1 shows picture of natural lighting in the sky, corona at sun's surface, and polar auroras, respectively.

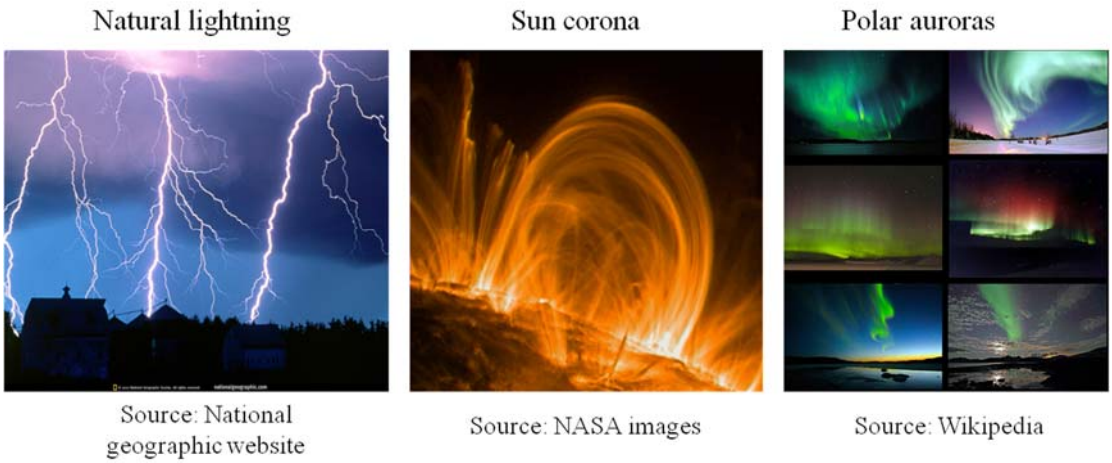

Figure 1.1 Pictures of natural lighting, solar corona, and polar auroras

Two other important examples where electron-impact excitation process plays significant roles are in the generation of lasers and plasmas. As we know, in terms of applications, both lasers and plasmas have enormous applications, ranging from academic research to industrial. Both lasers and plasmas have emerged as powerful tools to study fundamentals of spectroscopy at atomic and molecular levels. On the other hand, their industrial applications include semiconductors industries, biomedical, and petroleum to name a few. Continuous strides are being made to improve their performance, enhance efficiency, and broaden the application areas. Before we proceed further on this topic, let us look on how lasers and plasma systems are produced.

(i) Lasers: In the generation of lasers, especially gas lasers, (e.g., He Ne laser), fast moving electrons collide with gaseous atoms enclosed inside a discharge tube and are excited to higher energy levels (the process is called pumping), to achieve population inversion condition, i.e., a situation in which a particular higher energy level is more populated than a particular lower energy level. The photons emitted, as a result of

stimulated de-excitation of the atoms are collected and subsequently collimated to obtain a laser beam. An uninterrupted and efficient excitation process is therefore important to maintain a uniform laser beam [1]. (ii) Plasma: A plasma is a collection of partially ionized gas, which is produced when highly energetic electrons collide with gaseous atoms in their vicinity, resulting in the excitation and/or ionization of those atoms. In the presence of high electric and/or magnetic fields when fast moving electrons collide randomly with the gaseous atoms, it can result in the excitation as well as ionization of the atoms. The short lived excited atoms de-excite to lower energy levels, either spontaneously or by again colliding with the moving electrons; similarly, the ions re-combine with the moving electrons to form neutral atoms again. In all these processes, photons of different wavelengths are emitted; this is collectively called plasma emission. The extent of excitation and ionization of the gaseous atoms depends on the excitation efficiency of the energetic electrons, which in turn depends on the excitation cross sections. Maintaining a sustained plasma requires a continuous (/or uninterrupted) energizing of the free electrons, which is typically done by supplying electrical energy of MHz to GHz frequency rate [2].In view of the growing needs of the potential applications of lasers, plasmas, and other electron impact excitation based devices, continuous efforts are being made to improve their performances. In this regard, the optimization of lasers, plasma diagnostics, modeling of electric discharges, etc., requires clear understanding and control of electron-atom collision processes taking place in the system. One such parameter which is used to diagnose an electron-atom collision process is the Electron Impact Excitation Cross Section (EIECS). From the fundamental physics point of view, EIECS provide spectroscopic information about the energy levels involved in the

transition; consequently, it helps in understanding the transition process. EIECS data are helpful when modeling new electric discharges and optimizing laser systems. In plasmas, EIECS information is used in determining plasma parameters, such as temperature, electron energy distribution functions, etc. Therefore, the knowledge of excitation cross sections and control of the electron impact excitation process can have useful applications. In this dissertation, a new application of the electron impact excitation process, namely in Ultra-trace element detection and analysis, and a new method, to measure the electron impact excitation cross section, have been discussed. Also discussed is the aspect of using Cavity Ringdown Spectroscopy (CRDS) as an alternative tool for study of electron-atom collision processes.

1.2 Motivation

One of the motivations behind the present study was to explore the potential applications of combining cavity ringdown spectroscopy with the electron impact excitation (EIE) processes. The idea arises from the fact that both EIE and CRDS have their own merits. For example, excitation of atoms by electron impact mechanism in electron-atom collision processes is not restricted by selection rules, i.e. both optical transitions and non-allowed optical transitions can occur. Instead by carefully controlling the energy of the colliding electrons, any particular energy level of the atom can be predominantly (selectively) populated. On the other hand, CRDS is a highly sensitive laser absorption technique; it is typically 1000 times more sensitive than the conventional single-pass laser absorption technique. In addition, the CRDS technique allows one to measure absolute number density of the absorbing particles. Therefore, if CRDS could be combined with an electron impact excitation system, it may find interesting applications.

Alternatively, CRDS can be thought of as an additional tool to study electron-atom collision processes. To the best of our knowledge this study is the first of its kind with the objective as described above.

Although, it is believed that this novel idea will find new utilizations in future, two interesting applications of the combined EIE-CRDS technique are being described here. Two categories of studies were conducted: namely (a) measurement of the electron impact excitation cross sections, and (b) trace element detection and analysis. The importance and the merits of the both works are described in detail in subsequent Chapters 3 -6; yet an introductory brief description is presented below. In the sections below, the following topics have discussed: (i) advantages of EIE-CRDS in element detection and analysis, (ii) introduction of EIECS and (iii) on the choice of mercury as sample element to study.

It would be worthwhile to mention here that excitation of the atoms is the first and key step in this process. Therefore, a choice of appropriate excitation source is important. In different experimental techniques, different excitation sources are used for example, inductively coupled plasma (ICP) torch, electron gun, etc. However, we have used a microwave plasma torch (MPT) as the excitation source. The microwave plasma torch not only acts as an excitation source, but also as a source of atomization, which is an important requirement for trace element detection and analysis work. Elemental mercury (Hg) was used as the sample to be studied. Being a low power plasma source (avg. energy ~ 5 eV) the MPT act as an efficient source of excitation for Hg which has ionization potential of 10.43 eV.

1.3 Electron Impact Excitation Cross Section Measurement

1.3.1 What is an Electron Impact Excitation Cross Section?

Electron impact excitation cross sections can be understood as a hypothetical cross section offered to an incoming electron by an energy level of an atom, for interaction to take place. In an electron-atom collision process, when an electron approaches an atom, different energy levels of that atom offers different cross-sectional areas for interaction for the energy transfer process to take place. In other terms, it gives a measure of probability that electrons moving towards an atom would 'collide' or 'interact' and subsequently impart energy to the electrons orbiting in different energy levels only if it passes through a particular virtual cross-sectional area. The electrons not falling in that cross section region do not 'collide', and thus do not impart energy to the orbiting electrons. It should be noted that the EIECS of a particular energy level is a function of energy of the incoming electrons. Similarly, different energy levels offer different excitation cross sections to the same incoming electrons. The higher the cross section, the higher are the chances of interaction, and similarly lower the cross section, the lower are the chances of interaction, and thus accordingly exchange of energy. The figure 1.2 shows a visual representation of the hypothetical hard-sphere cross section.

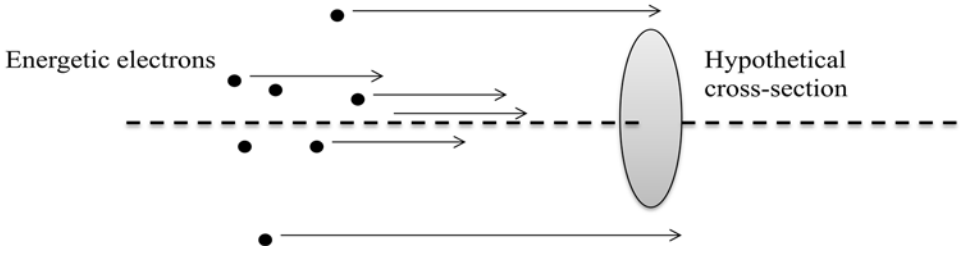

Figure 1.2 Pictorial representation of concept of EIECS

As a result of collisions with electrons, an atom is either excited to a higher energy level or can be ionized. This phenomenon is called electron impact excitation. On the other hand, upon collision with energetic electrons, an excited atom can also be de-excited to lower energy levels. In this work, we will discuss excitation phenomena, and therefore the excitation cross section, i.e., EIECS.

Experimental studies of electron impact excitation processes, including EIECS measurements, are often carried out either with the optical emission technique or the electron energy loss method. In the optical emission technique, the photons emitted as a result of excitations and subsequent de-excitations are recorded (Fig. 1.3). The emitted intensities, e.g. $I(\lambda_1)$ and $I(\lambda_2)$, as shown in the Figure 1.3, are directly proportional to the population density of the excited levels k and l, respectively; whereas the population densities of the excited states, n_k and n_l, are related to the excitation cross sections, Q_k and Q_l, from the lower level to energy levels k and l. Therefore, if the emitted intensities are known, it can be used to determine the excitation cross sections of energy levels [3].

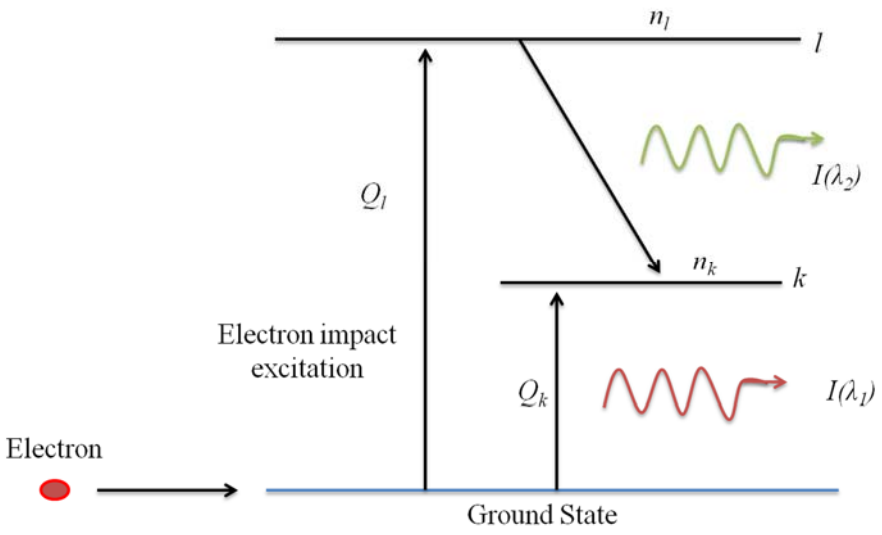

Figure 1.3 Schematic of excitation by electron impact

In the electron energy loss method, a mono-energetic beam of electrons are incident on the collection of gaseous atoms. The difference in the energies of the scattered electrons and the incident electron are compared. Since the energy levels of the sample gaseous atoms are known, the loss in the energies of the scattered electrons is attributed to the excitations to different higher atomic energy levels, which in turn is related to the excitation cross section [4].

Although both methods described above are used to determine EIECS, they suffer the limitation that they require an external calibration process to determine the absolute cross section values. A typical procedure is to obtain an expression for the cross section of the concerned energy level in terms of some known cross sections. Subsequently, the required cross sections are determined upon substituting the known cross section values. A detailed discussion on the methods of measuring EIECS by optical emission or of electron energy loss methods is beyond the scope of this work.

We have a developed a new method, based on EIE-CRDS, to measure absolute excitation cross section values. The cross section values result as an analytical solution of a set of non-linear equations of excitation-de-excitation processes obtained under steady state condition. Consequently, the method does not require an external calibration process to obtain the absolute cross section values. The method has been demonstrated by measuring EIECS of the first few energy levels of mercury under atmospheric conditions. This work demonstrated that the CRDS technique can be used as an alternative tool to measure electron impact excitation cross sections in an electron-atom collision process.

1.4 Element Detection and Analysis: Why with CRDS?

Plasma-based atomic emission spectroscopy (AES) is one of the widely used techniques for element detection and analysis. The types of plasmas that are typically used are inductively coupled plasmas (ICP) and microwave induced plasmas (MIP); combinedly with AES, the technique is termed as ICP-AES or MIP-AES, respectively. As discussed earlier, plasma contains highly energetic electrons which are capable of exciting atoms into various excited states by the process known as electron impact excitation. Owing to high temperature (ranging from several hundred to several thousand of Kelvin), the plasmas are capable of atomizing samples. Therefore, when liquid or gaseous samples are injected into the plasma, they are atomized and subsequently excited to higher energy levels. The atoms de-excite by emitting photons of different wavelengths which are characteristic of the elements present in the sample. The plasma emissions are collected and analyzed to detect the presence of elements by distinguishing their characteristic peaks in the emission spectrum. The concentration of a particular element in the sample is determined by carefully obtaining a calibration curve. The

lowest range in which concentration measurements with AES technique are possible varies from parts per million (ppm) to parts per billion (ppb) [2].

Although, ICP-AES and MIP-AES are widely used for element detection, the instruments are generally big and bulky. They are not suitable for real-time and *in situ* operations. In addition, they also require an external calibration process in order to determine the absolute concentration values. On the other hand and as it has been demonstrated in this study, CRDS being a laser-based absorption technique, can be incorporated with an electron impact excitation device (MPT in this case) to conduct ultratrace element detection and analysis by measuring concentrations in parts per trillion (ppt) range. Another merit of using CRDS for this purpose is its ability to measure the absolute number density. The advantage is that external calibration can be avoided while determining unknown concentrations of the elements. Additionally, with the advent of small size diode lasers in the market, which are now available in a variety of wavelengths range, it is possible to combine CRDS with a MPT, or for that matter any other suitable excitation source, to develop portable size instruments for real-time, *in situ* operation.

The first part of this work demonstrates the proof of principle of the technique, which has been demonstrated by detection and measurement of trace concentrations of mercury (Hg). Further, a compact size, dual-mode (i.e. both the emission and absorption mode of measurements), prototype instrument was developed for real-time, *in situ* operations. The functioning of the dual-mode of the instrument was demonstrated by analyzing a number of elements, such as As, Pb, Cd, Sr, etc., by optical emission spectroscopy facility.

1.5 Choice of Mercury (Hg) as Sample Material

As mentioned earlier, the present study was intended to develop and explore the potential applications of a combined EIE-CRDS system; two possible applications were investigated (i) measurement of EIECS in an electron impact excitation process, and (ii) element detection and analysis.

Mercury is an important element which has direct or indirect effects on human lives. Importance of mercury has two aspects: (i) health aspects and (ii) usefulness in utilities, such as discharge lamps.

Mercury is considered to be one of the important environmental pollutants of water, soil, and air. Mercury (Hg) in its elemental form is toxic in nature; however the organic and inorganic compounds of Hg, such as CH_3Hg and HgS, HgCl, etc., respectively, are even more poisonous. High (acute) exposure of Hg or long time (chronic) exposure of even low concentrations of Hg has severe human health hazardous effects. Acute or chronic exposure of mercury or its compounds are known to cause dyspnea, neuromuscular changes, etc. Release of mercury and its compounds in the environment is mainly attributed to industrial waste, or in some cases natural sources, such as volcanic eruptions [EPA].

The environmental cycle of mercury can be seen Figure 1.4. Fossil fuel burning and industrial wastes release mercury into the environment in soil, air, and water sources.

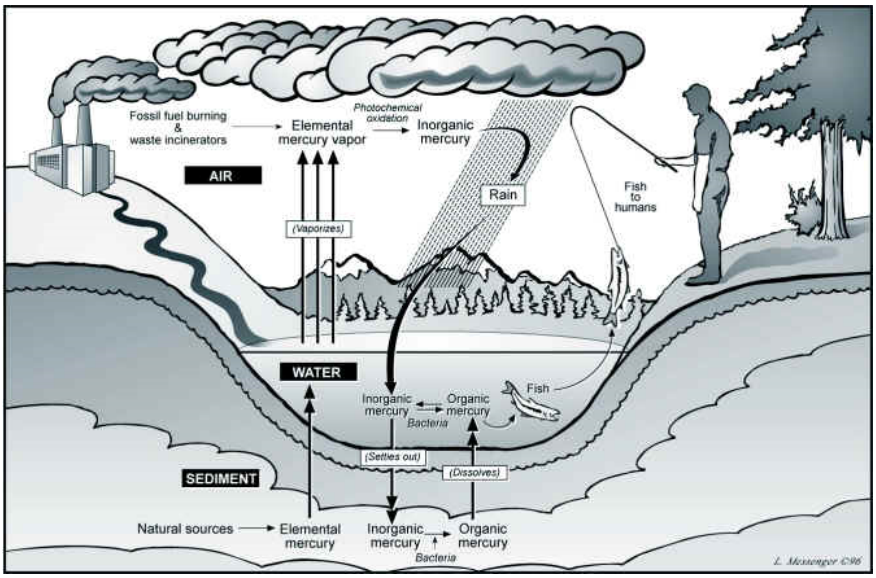

Figure 1.4 Mercury cycle in the environment

(Source: University of Wisconsin, Eau Claire, http://people.uwec.edu/piercech/Hg/mercury_water/cycling.htm

The soil, air and the water sources become contaminated as a result of that. Water species, such as fish, shrimp which are termed as sea foods, etc., swallows mercury from this contaminated water and accumulates Hg inside their body, from where it gets transferred to human beings when these creatures are eaten by humans. On the other hand, elemental mercury vapors causes Hg contents in rain which is absorbed by plants which may be eaten by humans or by animals that are subsequently eaten by humans. Thus, through this pathway also mercury is transferred to human body, which in time accumulates to a significant concentration level.

Agencies, such as the World Health Organization (WHO), Occupational Safety Health Administration (OSHA), etc., consider Hg as an occupational hazard. Therefore, many different countries have regulations on industrial and commercial use of mercury and disposal management of its waste generation. Millions of dollars are spent every year

for the detection, quantification and waste management of environmental pollutants, including mercury. Therefore, mercury is an important element as far as its detection and remediation is concerned.

On the other hand, mercury is also a useful element in the development of arc lamps and discharges. Owing to some strong persisting emission lines in the visible region, such as 404.65 nm (violet), 435.8 nm (blue), 546.1 nm (green) and 578.2 nm (yellow-orange), and a few in UV region, for example 253.65 nm, 365.4 nm, etc. [NIST], which can be excited using only few tens of watts of power, mercury is used extensively in arc lamps and other light sources. The process of optimization of these light sources utilizes the spectroscopic information of Hg, for example electron impact excitation cross sections (EIECS).

Therefore, using mercury as a sample element to study serves both purposes in the present work.

1.6 Research Plan

The results of the research discussed in this dissertation have been arranged as shown in the figure 5.

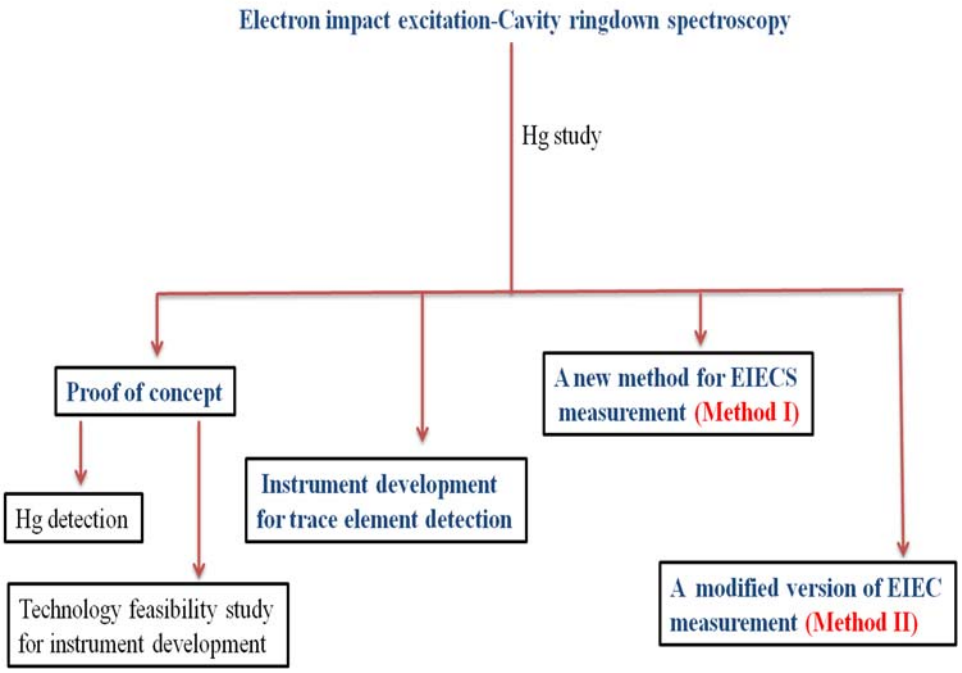

Figure 1.5 Electron impact excitation-Cavity ringdown spectroscopy

1.7 References

[1] Lasers, by A.E. Siegman, 1986, (University Science Books, Sausalito, CA, 94965)

[2] Fundamentals of Plasma Physics, by J. A. Bittencourt, 2004, Springer-Verlag, NewYork Inc.

[3] A.R. Filippelli, C.C. Lin, L.W. Anderson, J.W. McConkey, Adv. At. Mol. Opt. Phys. 33 (1994) 1-62.

[4] A. Chutjian, D.C. Cartwright, Phys. Rev. A 23 (1981) 2178-2193.

[5] T. Hadeishi, Ph.D. Dissertation, University of California, Berkeley, 1962

[6] A.A. Mityureva, N.P. Penkin, Opt. Spektrosk. 55 (1983) 393-395.

CHAPTER II

EXPERIMENTAL METHODOLOGY AND SETUP

In this chapter the experimental technique and the methodology involved in the study have been described in detail. Subsequently, the experimental setup is also explained, although some of the other relevant experimental details are mentioned in respective Chapters III to VI. As mentioned in Chapter I, cavity ringdown spectroscopy (CRDS) has been employed as the primary experimental technique. A microwave plasma torch (MPT) was used as an element atomization and excitation source. Elemental mercury (Hg) was used as the sample for study. A microwave induced plasma generated with MPT in the power range 100 – 150 Watt has an average excitation energy around 5 eV (electron energy distribution in plasma varies from 0.5 – 10 eV) [1]; therefore for mercury atoms, whose first few excited energy level lies in between 4 and 6 eV, the MPT acts as efficient excitation source. The optical emission technique (OES) which was also employed for emission intensity measurement has also been described. A comparison between the conventional laser absorption techniques and CRDS is also presented.

2.1 Conventional Single Pass Laser Absorption Technique

In the conventional single-pass laser absorption method, a laser beam is passed through a sample cell which contains a gaseous or liquid sample, to be studied. The transmitted light is collected, and the laser beam intensity of the transmitted light is

compared with that of the incident beam. The wavelength of the laser beam is chosen so as to match the sample atoms/molecule's absorption line. The decrease in the transmitted intensity depends on the sample's absorption strength and its concentration inside the cell. In addition, the transmitted laser beam intensity also depends on the path length of the laser beam. Path length is defined as the interaction length between the sample atoms and the laser beam. Figure 2.1 shows schematic of a typical single-pass laser absorption technique.

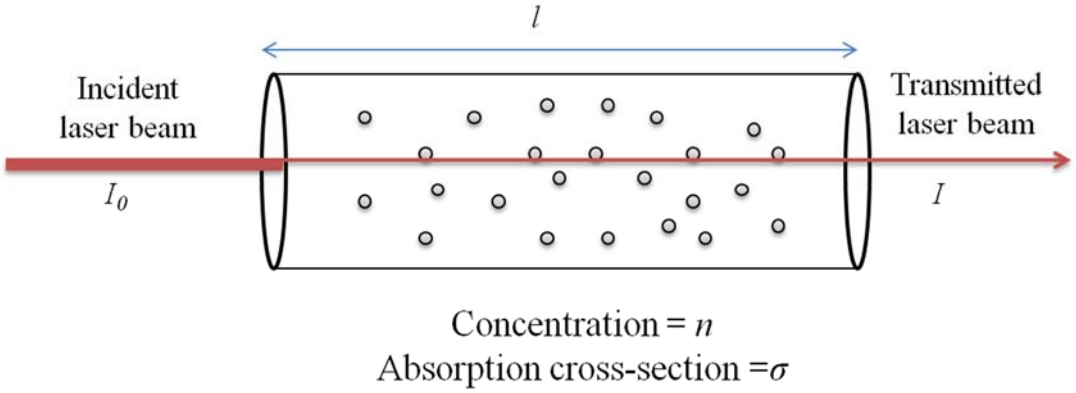

Figure 2.1 Schematic of single pass absorption technique

The transmitted laser intensity I is given by the Beer-Lambert's law as follows:

$$I = I_0 e^{-n\sigma l} \tag{2.1}$$

where I_0 is the intensity of the incident laser beam; n is the concentration of the absorbing material inside the sample cell; σ is the absorption cross section; and l is the path length. As it is evident from Eq. 2.1, the higher the absorption strength or the concentration inside the cell, the greater is the absorption of the laser beam. Similarly, if

the path length is longer, absorption will be more. In the conventional single-pass laser absorption method, the laser beam passes only once through the sample cell. The dimension (length) of the sample cell is typically on the order of centimeters (cm), and therefore, the path length also remains on the order of cm. A minimum detection sensitivity of the order of $\frac{\Delta I}{I} \approx 10^{-3}$ is achieved by the single pass cell. This puts a limitation on the single-pass cell to be used for studying extremely weak absorption cases [2].

The sensitivity of this technique is restricted by the path length inside the sample cell. Therefore, if a mechanism can be developed to increase the path-length of the laser beam by many times, the sensitivity of the system can be increased significantly. A simple way is to make the technique multi-pass in nature. Here comes the advantage of CRDS which is multi-pass in nature and can have path lengths on the order of hundreds of meter.

2.2 Cavity Ringdown Spectroscopy (CRDS) Technique

The cavity ringdown spectroscopy (CRDS) technique was first demonstrated by O'Keefe and Deacon in 1988. With time it has emerged as a powerful laser-based absorption technique which has been applied in many different areas, including fundamental spectroscopy, trace concentration measurement, etc. Details of fundamentals of CRDS, its applications and evolution with time can be found elsewhere [3-6].

Cavity ringdown spectroscopy is a multi-pass laser absorption technique, in which the path-length is increased by trapping a laser pulse inside a high finesse cavity constructed with two highly reflective mirrors. A light pulse injected into the cavity,

constructed with the two plano-concave mirrors (R > 99%), remains trapped between the two mirrors while it reflects back and forth inside the cavity. However, every time when it reflects from a mirror surface, a certain amount of light energy is transmitted out through the mirror's back. The temporal profile of the light intensity collected at the back of any mirror is exponentially decaying. Figure 2.2 shows a schematic of a typical CRDS setup.

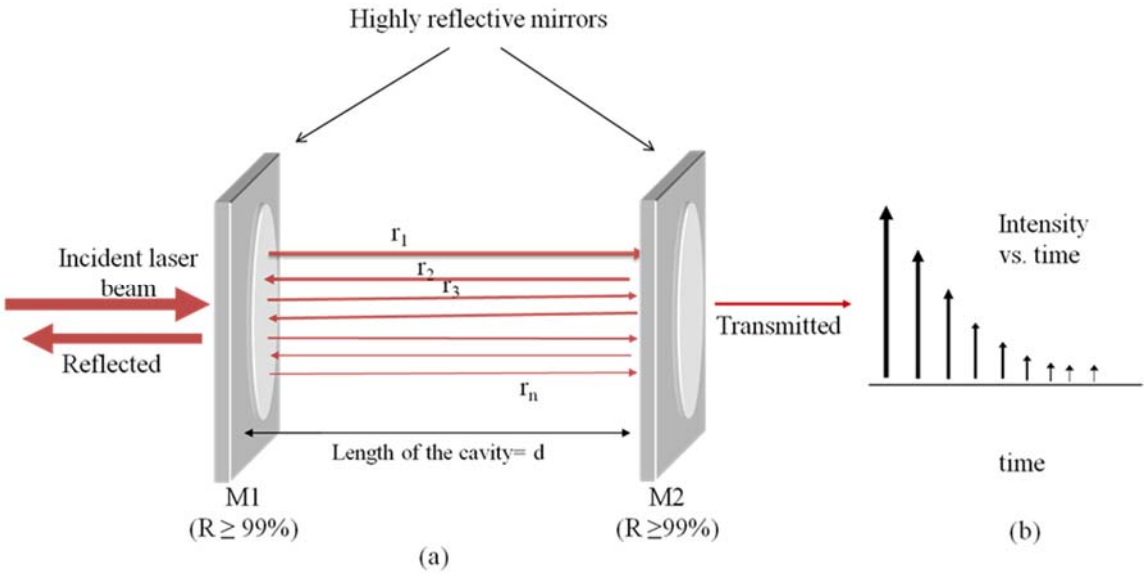

Figure 2.2 Schematic of CRDS

As shown in the figure, when a laser pulse is incident onto mirror M1, a major portion of its energy, depending upon the reflectivity of M1, is reflected back; however a small quantity (typically ≤ 1%) which gets injected (after being transmitted through M1) into the cavity, is reflected by the mirror M2, and moves back towards M1, from where it again is reflected back towards M2. This phenomenon keeps repeating, and the pulse

remains trapped inside the cavity. In Figure 2.2 (a), the lines r_1, r_2, $r_{3....}r_n$ represent the repeated reflections of the laser pulses inside the cavity. The physically separated and decreasing thickness of the lines r_1, r_2, $r_{3....}r_n$ is just to figuratively represent that inside the cavity there takes place numerous back and forth reflections, and upon each reflection some amount of intensity is transmitted out of the cavity which decreases the intensity of light inside the cavity. In actual practice, the laser beam is aligned along the axis of the mirrors, and all the reflection takes place along the axis. A good alignment is a crucial part in CRDS experimental setup. The profile of the transmitted light intensity from the second mirror M2 is exponentially decaying. This exponentially decaying profile resembles very much the decreasing intensity profile of a ringing bell, that's why the technique has been named 'ringdown.'

The time it takes for the transmitted intensity to decrease by 1/e times is termed as 'ringdown time'. The ringdown time is the main measured parameter in CRDS, and is obtained upon fitting the exponential decay intensity profile collected at mirror M2. The ringdown time, represented as τ, is a function of the length of the cavity and reflectivity of the mirror and is given as:

$$\tau = \frac{d}{c(1-R)} \tag{2.2}$$

where, d is the length of the cavity, c is the velocity of light, and R is the reflectivity of the mirrors at a given wavelength. If a CRDS system is perfectly aligned, a single exponential decay profile is obtained for the transmitted intensity; deviation from the single exponential behavior is indicative of alignment error. This exponential decay intensity profile is also termed as 'ringdown curve', and is very sensitive to the mirror

alignment; however by slightly tweaking the mirrors alignment, the ringdown curve can be manipulated.

If there is an absorbing material inside the cavity, the ringdown time expressed in Eq. 2.1. modified to:

$$\tau = \frac{d}{c(1-R+\alpha l_s)} \tag{2.3}$$

where α is the absorption coefficient of the sample molecules/atoms inside the cavity, and l_s is the absorption path length through the sample. In some cases, for example gas filling entire cavity, the cavity length is equal to the path length, i.e., $d=l_s$. The figure 2.3 represents two cases when absorption (α) inside the cavity is zero and non-zero, represented by red and blue colors, respectively; the *ringdown time* for which has been represented by τ_0 and τ, respectively. It can be noted that the ringdown curve at $\alpha \neq 0$ decreases faster in comparison to when $\alpha = 0$; this indicates higher absorption in the former case. This also suggests that the ringdown time in the case of no (or lesser) absorption would be higher, i.e. $\tau_0 > \tau$.

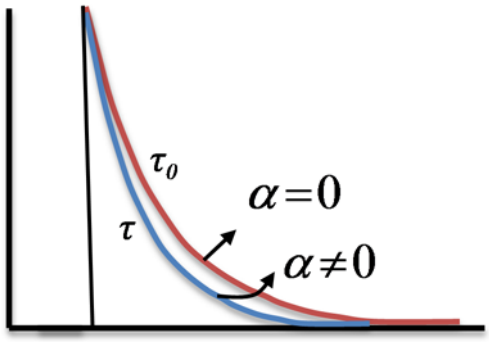

Figure 2.3 Example of ringdown curve

The absorbance A of the material inside the cavity is determined from the two ringdown times measured with ($\alpha \neq 0$) and without ($\alpha = 0$) the absorbing material inside the cavity:

$$A = \frac{d}{c}\left(\frac{1}{\tau} - \frac{1}{\tau_0}\right) = \alpha l_s \tag{2.4}$$

Theoretically the absorbance A is also given as:

$$A = \sigma_{abs}(\nu) n l_s \tag{2.5}$$

where $\sigma_{abs}(\nu)$ represents the wavelength dependent absorption cross section of the sample molecules/atoms, and n is the sample concentration (number density). From Eqs. 2.4 and 2.5, it turns out that the absorbance A measured as a function of two ringdown times, can be used to determine the number density n or alternatively the absorption cross section $\sigma_{abs}(\nu)$ of the absorbing material, if either of them is known.

2.3 Detection Sensitivity of CRDS

The detection sensitivity of a CRDS system is dictated by mirror reflectivity and signal stability for a given cavity length. The stability of ringdown signal is measured in terms of the baseline stability, which is defined as:

$$B.S. = \frac{\sigma_\tau}{\tau} \tag{2.6}$$

where σ_τ is the standard deviation of the ringdown signals and $\bar{\tau}$ is the average ringdown time. The minimum absorbance that can be measured with a CRDS system is given as:

$$A_{\min} = \frac{\sigma_\tau}{\bar{\tau}}(1-R) \tag{2.7}$$

If mirrors of reflectivity R=99.99% are used, then by maintaining a baseline stability of 0.3% or less, a minimum absorbance of on the order of ~ 10^{-7} can be obtained. Therefore, in comparison to single-pass laser absorption spectroscopy, 1000 time higher sensitivity can be obtained with a CRDS system. The minimum detectable absorbance can be chosen based on $3\sigma_\tau$ (three time standard deviation) or $1\sigma_\tau$. Subsequently, the detection limit (*DL*) in measuring number density with a CRDS system can be obtained by modifying Eq. 2.5.

$$DL = n_{\min} = \frac{A_{\min}}{\sigma_{abs}(\nu) l_s} \tag{2.8}$$

where n_{min} represents the minimum detectable concentration; R, $\sigma_{abs}(\nu)$, and l_s are was defined for the above equations. Concentrations up to the order of parts per trillion (ppt) (10^{-12}) can be obtained with a CRDS technique [3-6].

2.4 Electron Impact Excitation-Cavity Ringdown System

As mentioned in Chapter I, the excitation of the atom is the first key step in this process, and the preference of excitation by the electron impact method is due to the reason that this excitation process is not restricted by selection rules unlike the case of optical transitions. The method EIE-CRDS is explained below in a simple way.

Consider a three energy level system as shown in Figure 2.4. The ground state atoms and the atoms in higher (excited) states have been represented by blue and red color, respectively. The energy gap between the ground state and the first two first

excited states is E_1, and the energy gap between 2nd excited state and the ground state is E_2.

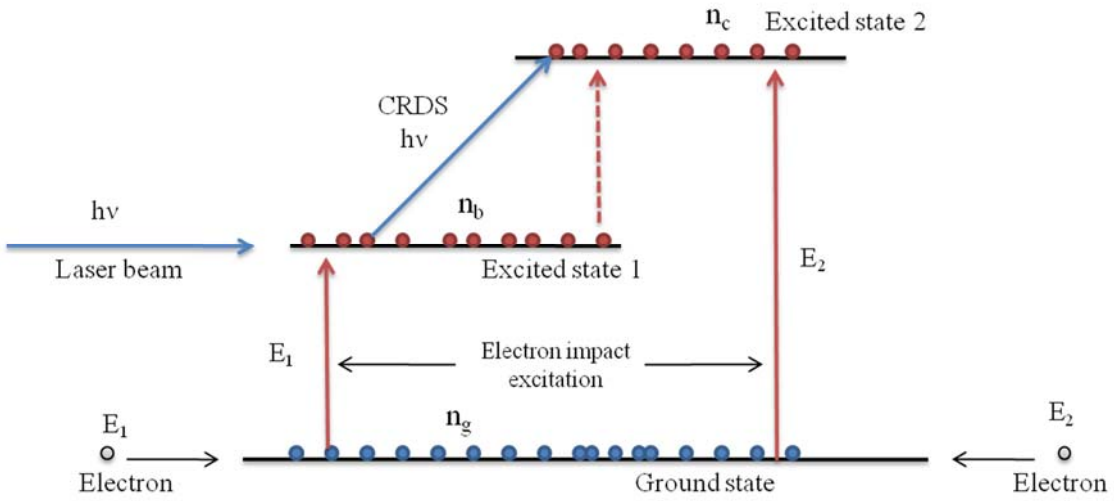

Figure 2.4 Schematic for EIE-CRDS.

The fast moving energetic electrons impart energy to the atoms upon collision. Owing to the collisions with electrons of energies E_1 and E_2, atoms in the ground state can rise directly to the higher excited states 1 and 2, respectively; this is termed as direct electron impact excitation. However, it should be noted that since the process of excitation by electron impact is not restricted by selection rules, if electrons of suitable energies are available, atoms in excited state 1 upon collision with those electrons can also rise to excited state 2.

If a mono-energetic source of electrons is used, a particular excited level of the atom can be predominantly populated; let us say the excited state 1 in Fig 2.4. Subsequently, if a CRDS system is employed with a laser of wavelength equal to the

energy gap $E_2 - E_1$, the absolute number density of the excited state 1 can be measured. Thus, by carefully choosing the electron source, different excited states of the atoms can be populated, and subsequently their atom density can be measured with CRDS technique by using suitable laser wavelengths.

Therefore, a choice of appropriate excitation source is crucial. Depending on the type of the excitation source and the experimental setup, the equations described in the above sub-section 2.2 and 2.3, should be modified when used in combination with a cavity ringdown system. Since, in this study we have used microwave plasma torch (MPT) as the excitation source, the equations would be similar to that used for a plasma-CRDS system.

A microwave plasma torch (MPT) was placed in the middle of the cavity such that the laser beam passes through the plasma plume as depicted in the Figure 2.5. Sample particles are injected into the plasma in the form of aerosols which are generated with the help of nebulizer. Owing to high temperature in MIP (2000-6000 K) the samples injected in the plasma are atomized; subsequently after collision with energetic electrons they are excited to higher energy levels. The wavelength of the laser is chosen to match one of the absorption lines of the sample element. The schematic of the experimental arrangement can be visualized in Figure 2.5.

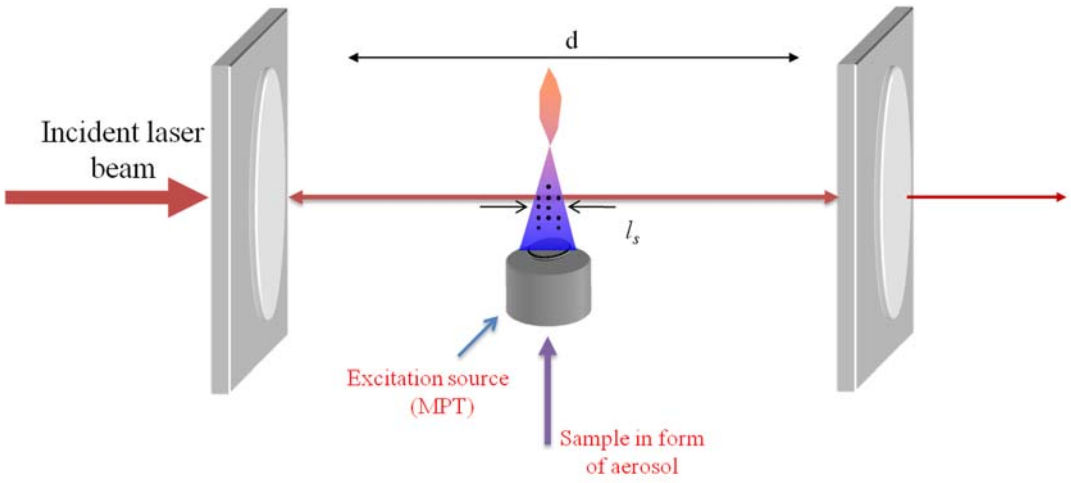

Figure 2.5 Co-arrangement of CRDS and plasma system.

In this case, the path length is the interaction length of laser and plasma, represented by l_s in the figure. The ringdown time is given as:

$$\tau = \frac{d}{c(1 - R + \beta_{plasma} l_s + \beta_{air}(d - l_s) + absorbance)} \tag{2.9}$$

where β_{plasma} and β_{air} are the scattering coefficients of plasma and open air, respectively. Eq. (2.9) can be re-written as:

$$\tau = \frac{d}{c(1 - R_{eff} + absorbance)} \tag{2.10}$$

In general, the scattering coefficients are negligible in comparison to the absorption occurring inside the cavity. Therefore, all the losses other the actual absorption can be incorporated together; the same has been represented as R_{eff} in Eq. (2.10). Similar to as described above in Section 2.2, the ringdown times are measured

with and without sample in the plasma. Subsequently, the absorption cross section or the number density can be determined using the following relation:

$$\sigma(v)n(r)l_s = \frac{d}{c}\left(\frac{1}{\tau} - \frac{1}{\tau_0}\right) \tag{2.11}$$

It should be noted that because of the turbulence of the plasma, the stability of the signal may be slightly comprised when the plasma is on. However, it can still be maintained with baseline stability ≤ 0.5%.

The details about the experimental setup used in different studies and relevant derivations have been discussed in the appropriate chapters. Other useful information, such as sample preparation, calibration process, data recording and analysis methods, etc., have also been discussed accordingly.

2.5 Excitation Source: Microwave Plasma Torch

2.5.1 Why prefer MIP?

It is important to discuss why did we chose a MIP source (i.e. MPT) over ICP or an electron gun as the electron impact excitation source in the present study. In order to understand that, we first need to analyze the motivation behind the present work. Apart from developing methodology to use CRDS in conjunction with an electron impact excitation source, the present study was conducted with the motivation to design a portable size instrument for trace element detection (of a contaminated liquid sample) as well. In this regard, we required an excitation source which can also efficiently atomize the elements in the sample. The instrument is supposed to be operated real time and under *in situ* conditions at the contaminated site itself. An electron gun, which is typically used

in producing mono-energetic beams of electrons, may not be a very suitable choice in this case. Efficient operation of the electron gun requires a sophisticated environment, for example vacuum conditions. Electron guns are typically used in lab based experiments where vacuum conditions can be created and maintained properly. For *in situ* operation, a robust excitation device is needed. The inductively coupled plasma can be one such device that can be used.

Now let us look at specific details of ICP and MIP. Inductively coupled plasma (ICP) and microwave-induced plasma (MIP) are the two most commonly used plasmas in laboratories. In ICP, gaseous atoms are excited typically with a 13.4-MHz radiowave signal and a few hundred watts of power. The ICP is a high-density plasma where the electron density varies from $10^{14}$to 10^{16} electrons cm^{-3}, and the plasma temperature ranges from 5000 to 10000 K. The electron energy distribution in an ICP varies from less than an electron volt to few tens of electron volts. Owing to its high temperature and high electron density, ICP does find applications in element detection, material processing, etc. In conjunction with gas chromatography (GC), atomic emission spectrometry (AES) and mass spectrometry (MS), ICP has been widely used for element detection and analysis for many years. In academic research, ICP-AES is also used for spectroscopic study of atoms and molecules. However, an ICP is a big and bulky instrument; its operating electronics and mechanical arrangements are also complicated. The ICP instruments are usually bench top instruments [7].

In comparison to the ICP, a MIP is a low-power plasma system, which is produced with microwave signals (GHz) and can be operated at a few tens of Watts of power as low as 50 W. The most commonly used microwave generator to produce a MIP

is 2.45-GHz magnetron. Typically, the plasma temperature and electron densities in MIP are on the order of 2000 to 4000 K, and $10^{12}$to 10^{14} electron cm^{-3}, respectively. From an application point of view, similar to ICPs, MIPs are also used in element analysis in conjunction with GC, AES, and MS. However, the instrument configuration of a MIP system can be made portable. The operating electronics and mechanical arrangements are also simple. Additionally, unlike ICP, the MIP being a low-power plasma source does not require radiation shielding [8].

Therefore, an MIP source, namely a microwave plasma torch (MPT) has been used in the present study. After the advent of the robust MPT, it has been possible to think of developing compact size instruments for various applications, including trace element detection. It has already been demonstrated that MPT can be combined with a CRDS system to detect environmentally toxic elements, such as U, Hg, Pb, etc (discussed in detail in Chapter IV). A number of environmentally important elements can be excited from the ground state to few low lying higher energy levels by the electron impact excitation process using MPT, and subsequently can be detected with the CRDS technique. For example, elements such as Hg, Be, As, Cs, Pb, Se, and U can be detected with the EIE-CRDS method by using lasers of wavelength 253.65, 313.04, 419.08, 442.57, 405.78, 241.35, 348.93 nm, respectively. Furthermore, a portable size instrument can be developed in the future when a compact diode laser at these wavelengths becomes available. The Figure 2.6 shows a schematic of the microwave plasma torch that was used in the present study.

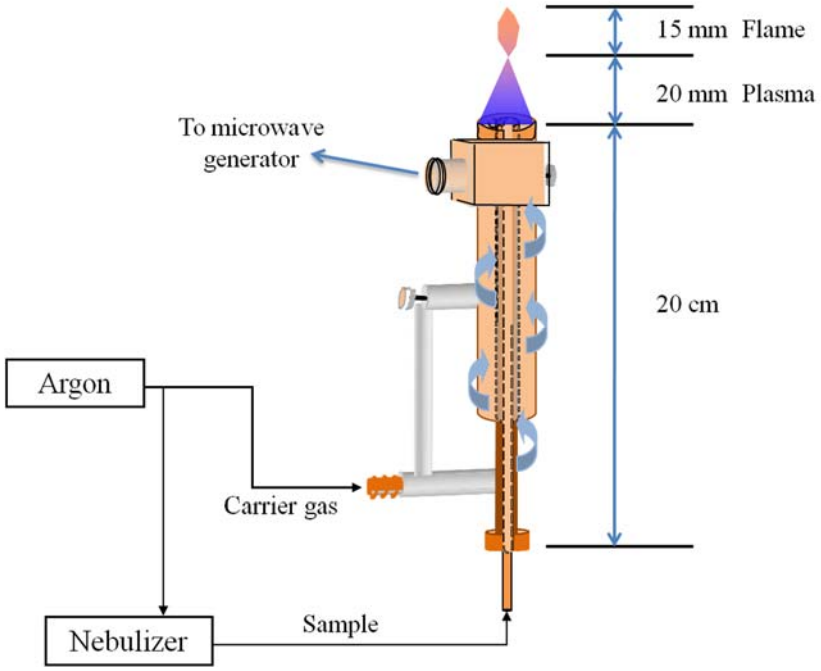

Figure 2.6 Schematic of MPT.

2.5.2 Excitation Mechanism in MPT

Depending on the excitation efficiency, plasma temperature, electron density, instrumentation portability, etc., MPT finds its applications ranging from spectroscopic study to commercial industries, including element detection. Being a low power plasma system (average energy ~ 5 eV) the MPT acts as an excellent source of excitation for a number of elements with high ionization potential (I.P.), such as Hg (I.P. = 10.47 eV), Cd (I.P. = 8.93 eV), Pb (I.P. = 7.41 eV), etc.; the MPT acts more as the source of excitation rather an than ionization source for these elements. As a result, for heavy elements (e.g., Hg, Be, Pb, etc.), excitation to the lower lying energy levels is dominant. Out of many combinations of excitation and de-excitations occurring inside the microwave plasma, some of them are listed below:

$e + A_{gr} \rightarrow A^* + e$	(Excitation from ground state to a higher state)
$e + A_{gr} \rightarrow A^+ + e$	(Ionization from ground state)
$e + A^* \rightarrow A^{**} + e$	(Excitation from one higher state to other)
$e + A^* \rightarrow A^+ + e$	(Ionization from a higher state)
$e + A^{**} \rightarrow A^* + e$	(De-excitation from a higher state upon collision)
$e + A^+ \rightarrow A_{gr}$	(Re-combination to form neutral atom from an ion)
$A^* \rightarrow A + e$	(Spontaneous de-excitation to a lower level)

In this work, the choice of MPT, therefore, was able to serve both the purposes of (i) excitation source (i.e. source of energetic electrons) for the electron impact excitation cross section measurement, and (ii) an efficient atomization and excitation source in the development of a portable size instrument for element.

2.6 Energy Level Diagram of Mercury

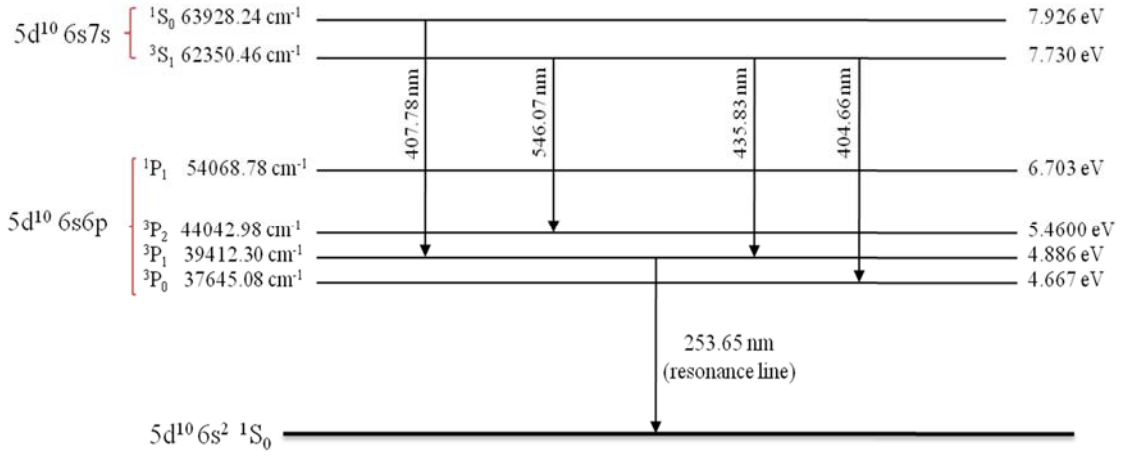

Figure 2.7 Energy level diagram of Hg.

Figure 2.7 demonstrates the energy level diagram of mercury atom (IP= 10.43 eV). The ground state of mercury is the $5d^{10}6s$, level and is represented by $6s^{21}S_0$, as shown in the figure. The subsequent excited states shown belong to different energy levels of $5d^{10}6s6p$ and $5d^{10}6s7s$ levels. The figure depicts the atomic energy level diagram of Hg up to energy level corresponding to 7.926 eV above the ground level. The different transition lines occurring in this energy region are shown in the figure. The strongest transition line of mercury originates as a result of a transition between the ground state and the regular 6s6p $^3P_1$ level which is at E =39412.30 cm^{-1} (equivalent to 4.886 eV). The first metastable state is 6s6p $^3P_0$ at 4.667 eV above the ground level. The 404.65 nm and the 435.83 nm transition lines which results from the transitions 6s7s $^3S_1 \rightarrow$ 6s6p $^3P_0$ and 6s7s $^3S_1 \rightarrow$ 6s6p $^3P_1$, respectively, are the second strongest transition lines in this energy range (NIST atomic database). The transition lines corresponding to 407.78 nm and 546.07 nm are relatively weak.

In the present study we have focused on obtaining CRDS absorption spectra with a 404.65 nm laser wavelength, i.e., for the transition 6s6p $^3P_0 \rightarrow$ 6s7s $^3S_1$. The 6s6p $^3P_0$ energy level being metastable has its own importance; additionally, electron impact excitation cross sections out of metastable levels are of special interest from spectroscopic point of view.

One of the motivations behind using the 404.65 nm transition line is the fact that there have become available small size diode lasers in the market at that wavelength. Therefore, in view of designing a portable size instrument for mercury detection, the 404.65 nm transition is a suitable choice.

2.7 References

[1] Schmidt, M.; Conrads, H. in: R. Hippler, H. Kersten, M. Schmidt, K.H. Schoenbach (Eds.), Low Temperature Plasmas: Fundamentals, Technologies, and Techniques, WILEY-VCH, 1, 2008, pp. 363-383.

[2] Laser Spectroscopy: Basic Concepts and Instrumentation, by W. Demtröder, 2003,Springer-Verlag Berlin Heidelberg.

[3] O'Keefe, A. O.; Deacon, D. A. G. Cavity ring-down optical spectrometer for absorption measurements using pulsed laser sources. Rev. Sci. Instrum. 1988, 59, 2544-2551.

[4] Cavity-Ringdown Spectroscopy: An Ultratrace-Absorption Measurement Technique, edited by K. W. Busch and M. A. Busch, ACS Symposium Series (720 Oxford University Press, 1999).

[5] Berden, G.; Peeters, R.; Meijer, G. Cavity ring-down spectroscopy: Experimental schemes and applications. Int. Rev. Phys. Chem. 2000, 19, 565-607. Wang, C.; Miller, G. [6] Wang, C.; Miller, G. P.; Winstead, C. B. "Cavity ringdown laser spectroscopy," in Encyclopedia of Analytical Chemistry, R. A. Meyers, Ed., New York: John Wiley, 2008.

[7] Inductively Coupled Plasma Spectrometry and its Applications, Edited by Steve J. Hill, John Wiley, 2006.

[8] Microwave Induced Plasma Analytical Spectrometry, by K. J. Jankowski, E. Reszke, RSC Publishing, 2010.

[9] NIST atomic database http://physics.nist.gov/PhysRefData/ASD/lines_form.html

CHAPTER III

A NEW OPTICAL METHOD OF MEASURING ELECTRON IMPACT EXCITATION CROSS SECTION OF ATOMS: CROSS SECTION OF THE METASTABLE 6S6P $^3P_0$ LEVEL OF HG

3.1 Abstract

We report a new method that is potentially applicable to the measurement of electron impact excitation cross sections of any atom. Measurement of the cross section of the metastable 6s6p $^3P_0$ level of mercury is conducted to demonstrate the method, which involves using cavity ringdown spectroscopy to determine the absolute number density of mercury atoms in the 6s6p $^3P_0$ energy level. The measured cross section is 1.7×10^{-17} cm^2 and is in agreement with the literature values. Compared with optical methods that have been used during the last three decades, this new approach not only serves as an alternative optical method, but also is applicable to atoms under both high and low pressure conditions.

Note: The major contents of this chapter have been taken from Physics Letters A 375 (2011) 2366-2370.

3.2 Introduction

The study of electron-atom collision processes is essential to the understanding of physical and chemical fundamentals in many fields, such as atomic physics, plasma physics, and plasma gas kinetics. Atoms under electron impact excitation can be excited, theoretically, to any excited states (or levels) because the excitation process is free of the optical transition selection rules, such as the angular momentum and spin selection rules. One of the key parameters to characterize the electron-atom collision processes is the electron impact excitation cross section (EIECS). Since its introduction in 1981,the laser excitation fluorescence spectroscopy has been the dominant optical method used to measure EIECS [1]. This method was initially implemented in conjunction with optical emission spectroscopy (OES); it has now been evolved to use OES alone to determine the EIECS. Majority of the experimental database on the cross sections of atoms in either regular excited states (spontaneous transitions are allowed) or long lifetime metastable states (spontaneous transitions are forbidden) has been developed based on the aforementioned technique [2-4]. Except for the OES, the electron energy loss technique, and theoretical calculations [5, 6], to date, no other well accepted method has been available to determine the EIECS. The conventional single-pass absorption spectroscopy method was once reported to measure the EIECS [7, 8]; however, this method, due to its low sensitivity, requires number density of the state of interest be sufficiently high. Thus, it has been abandoned.

We report a new method to determine the EIECS of atoms, and this technique will be applicable to the measurement of the EIECS of atoms in either regular excited states or metastable states. Determination of the EIECS of atoms in a metastable state is more

challenging than in a regular excited state because the population number density in a metastable state is typically several orders of magnitude lower than the density in the ground state and no optical emissions from the metastable state are observable. The new method involves the determination of the absolute number density of the atom in the state of interest using cavity ringdown spectroscopy (CRDS) [9]. Due to its high sensitivity stemming from the multiple-pass nature of the technique, CRDS, can be used to measure the absolute number density of atoms in low concentrations; however, its potential for the determination of EIECS of atoms has not be explored to date. In this Letter, we demonstrate the new method by measuring the EIECS of the metastable 6s6p $^3P_0$ level of mercury (Hg), in which the absolute number density of Hg atoms in the 6s6p $^3P_0$ level is measured using the CRDS technique and the population of Hg atoms in the metastable state is achieved through impact excitation of the electrons generated in an atmospheric pressure microwave plasma. We use the measured number density of the metastable 6s6p $^3P_0$ level to solve the four-energy levels' rate equations of Hg to obtain the EIECS of the state.

3.2.1 Optical Method of measuring EIECS: Emission

Figure 3.1 shows a typical excitation scenario with a two energy level system. The energy level *a* is a lower level and the energy level *b* is a higher than *a*. Upon collision with a beam of electrons the atoms in the energy level *a* are excited to the energy level *b*; this excitation process is called excitation out of the level *a*. In practice the level *a* can be any energy level in general including ground state. In the figure the energy levels above b has been denoted by *j* while all the energy levels lying below the energy level *b* has been denoted by *i*.

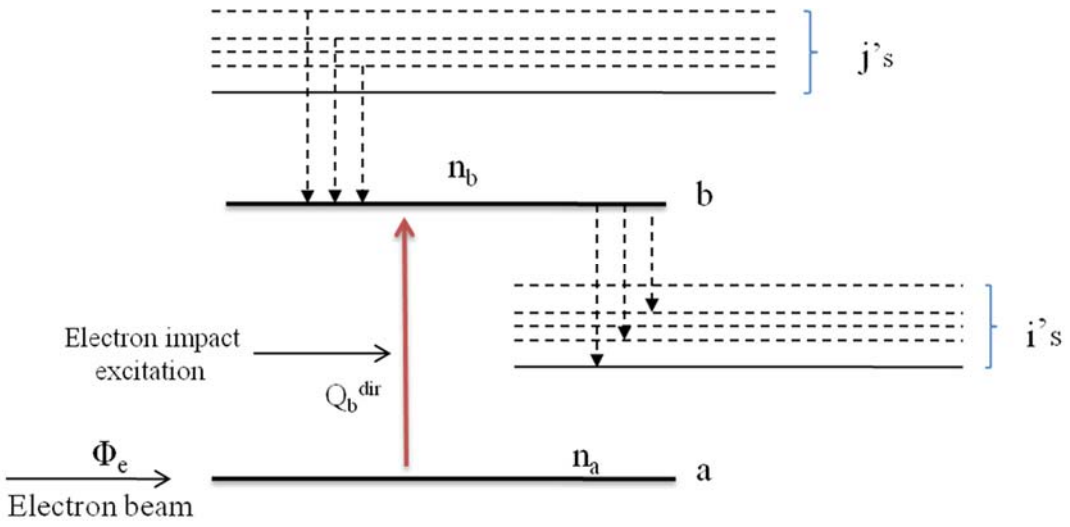

Figure 3.1 A general excitation case shown with two-energy level system.

The population rate equation for the energy level *b* at any given time *t* can be written as,

$$\frac{dn_b}{dt} = \Phi_e n_a Q_b^{dir} + \sum_{j>b} n_j A_{jb} - \sum_{i<b} n_b A_{bi} \tag{3.1}$$

The first term in the right hand side (RHS) denotes the population increase rate of *b* by direct excitation (electron impact) from the energy level *a*; where Φ_e, n_a, and Q_b^{dir} represents the electron flux per unit area, population density of the level *a*, and direct electron impact excitation cross section of energy level *b* out of the level *a*, respectively. The second term on the RHS represents the rate of increase of the population of the energy level *b* as result of spontaneous emission from the all the energy levels above *b* (represented by *j*), and the third term represents the rate of loss of the population density

of the level *b* as a result the spontaneous transition from the level *b* to *a* different levels lower than *b* (represented by *i*).

After the system achieves the steady state condition,

$$\frac{dn_b}{dt} = 0 \tag{3.2}$$

Therefore, at steady state condition, Eq. (3.1) modifies to

$$\Phi_e n_a Q_b^{dir} = \sum_{i<b} n_b A_{bi} - \sum_{j>b} n_j A_{jb} \tag{3.3}$$

$$Q_b^{dir} = \sum_{i<b} \frac{n_b A_{bi}}{\Phi_e n_a} - \sum_{j>b} \frac{n_j A_{jb}}{\Phi_e n_a} \tag{3.4}$$

The terms optical cross sections have been defined as,

$$Q_{bi}^{opt} = \frac{n_b A_{bi}}{\Phi_e n_a} \quad \text{and} \quad Q_{jb}^{opt} = \frac{n_j A_{jb}}{\Phi_e n_a}$$

Subsequently, the Eq. 3.4 further modifies to

$$Q_b^{dir} = \sum_{i<b} Q_{bi}^{opt} - \sum_{j>b} Q_{jb}^{opt} \tag{3.5}$$

Again, by the definition, the first term on the RHS of Eq. (3.5) is called "Apparent cross section" (all optical cross sections out of *b*) and the second term is called "Cascaded cross section" (all optical cross sections into *b*), i.e.,

$$Q_b^{App} = \sum_{i<b} Q_{bi}^{opt} \quad \text{and} \quad Q_b^{Cas} = \sum_{j>b} Q_{jb}^{opt}$$

Therefore, we have from Eq. (3.5),

$$Q_b^{dir} = Q_b^{App} - Q_b^{Cas} \tag{3.6}$$

The Eq. (3.6) suggests that in order to measure the direct cross section to the energy level b, one need to measure all the optical cross section in and out of the energy level *b*. In actual practice it is difficult to measure the contributions from each and every level above and below the level *b*, because of the wide range of emission wavelengths. However, the apparent cross section can be determined if the cascaded contributions can be estimated using the Eq. (3.6) $Q_b^{App} = Q_b^{dir} + Q_b^{Cas}$.

3.2.2 LIF Method to measure EIECS

The method to measure EIECS using the LIF technique is explained in this section. As described in literature [1-4], the methodology is explained with a three energy level system, as shown in Figure 3.2.

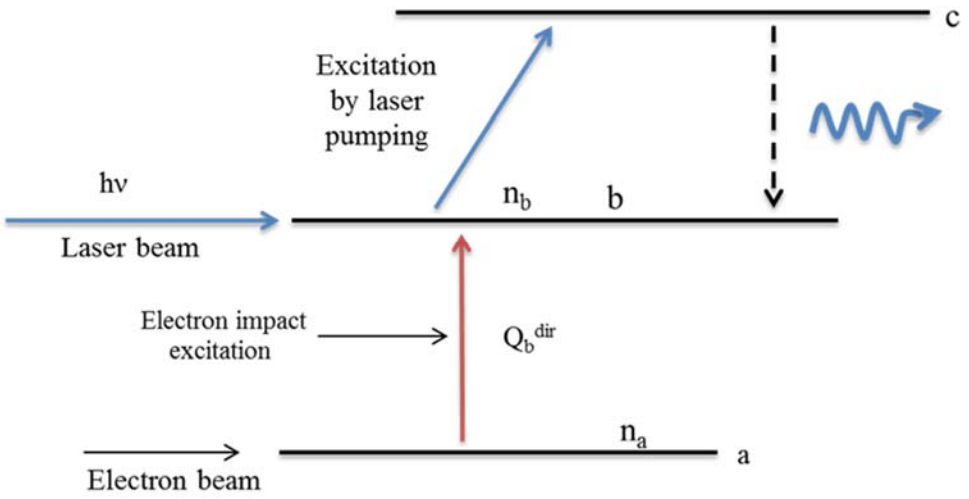

Figure 3.2 Schematic representing LIF method for the measurement of EIECS.

In this particular example, the energy level *b* is a metastable level (optical transition not allowed), whereas energy level *c* is regular level (optical transition allowed). The energy level *a* may be ground level. In general there has been considerable interest in studying excitation 'into' and 'out' of a metastable level, because of its applications in utilities like lasers and other gaseous discharges. In the present case, as shown in the figure, excitation to the energy level *b* from *a* takes place only through the electron impact excitation process. Upon collision with the electrons, atoms in energy level *a* rise to level *b* by direct impact excitation process which is termed as excitation out of the level *a*, or excitation into the metastable level *b*. If energy level *a* is the ground energy level, then this process is termed as excitation out of the ground state. Some of the atoms in other higher levels may in also rise to the energy level *c* through step wise excitation process. Since, the level c is a regular level and as shown in the figure the transition from *c* to *b* is allowed, therefore, the energy level *c* can undergo spontaneous emission from $c \rightarrow b$. If this emission is strong enough it can be recorded in the emission spectrum. The intensity of emission from $c \rightarrow b$ depends on the population density of the energy level *c.* Higher the population density of *c*, more intense would be the emitted intensity.

In LIF method, a laser tuned to wavelength equivalent to the energy gap between *c* and *b* is employed to optically pump the atoms in the energy level *b* to the energy level *c*. As a result, the population of the level *c* increases and so does the intensity of the emitted line $c \rightarrow b$. The increase in the population density of *c* is dependent on the amount that is being pumped out of the level *b* by the laser beam, which in turn depends on population density of the level *b*. On the other hand, solving the steady state population

rate equation of the energy levels *b* and *c*, the population density of the level *b*, i.e. n_b, can be expressed in terms of n_a, optical cross sections and the Einstein's coefficients of various transitions taking place. Subsequently, the differences in the intensities of the transition $c \rightarrow b$ in the two cases, namely laser OFF and laser ON is utilized to determine the concerned excitation cross section. Further, external calibration is used to obtain absolute values. A detailed explanation of this method can be found elsewhere [1-4].

3.3 Experimental Setup of the Present Work

Figure 3.3 shows a schematic diagram of the experimental system, which consists of an atmospheric argon microwave plasma torch (MPT) excited by a 2.45 GHz microwave source, a CRDS system, an OES system, and an Hg sample introduction portion. The MPT was located in the middle of the ringdown cavity with a mirror (R= 99.93 %) separation of 73 cm. A 405 nm laser beam was generated by a narrow linewidth (0.075 cm^{-1} at 500 nm) OPO system (SpectraPhysics, MOPO-HF-FDO 290) with a pulse repetition rate of 10 Hz and output power at 405 nm of 50 mW. The emissions of Hg at 405 and 254 nm were simultaneously recorded by an optical emission spectrometer (Avantes) with a spectral resolution of 0.07 nm at 350 nm. In the experiment, various concentrations of Hg solutions, ranging from 20 ppm to 500 ppm (Absolute Standards, Inc.) were introduced into the MPT through an ultrasonic nebulizer that converted the aqueous solutions into a gaseous vapor carried by argon gas.

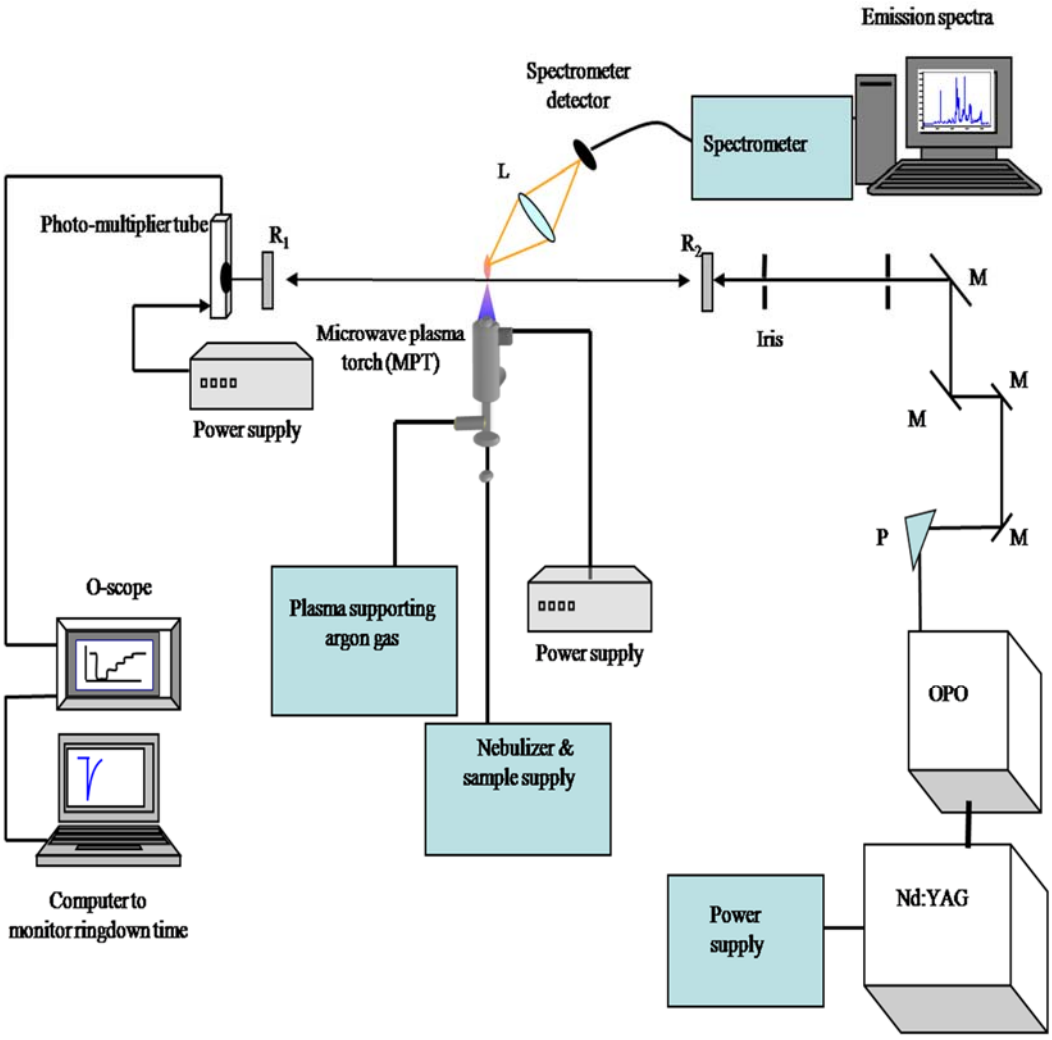

Figure 3.3 Schematic of the combined plasma-CRDS experimental system utilized in the present work.

3.4 Results and Discussion

Measured ringdown spectra of Hg around 405 nm are shown in Figure 3.4. To the best of our knowledge, this is the first report of optical absorption spectra of Hg at 405 nm. This is partially due to the fact that the ground state of the 405 nm transition is a metastable state, whose population requires using a non-optical excitation routine, such as the electron impact excitation described herein.

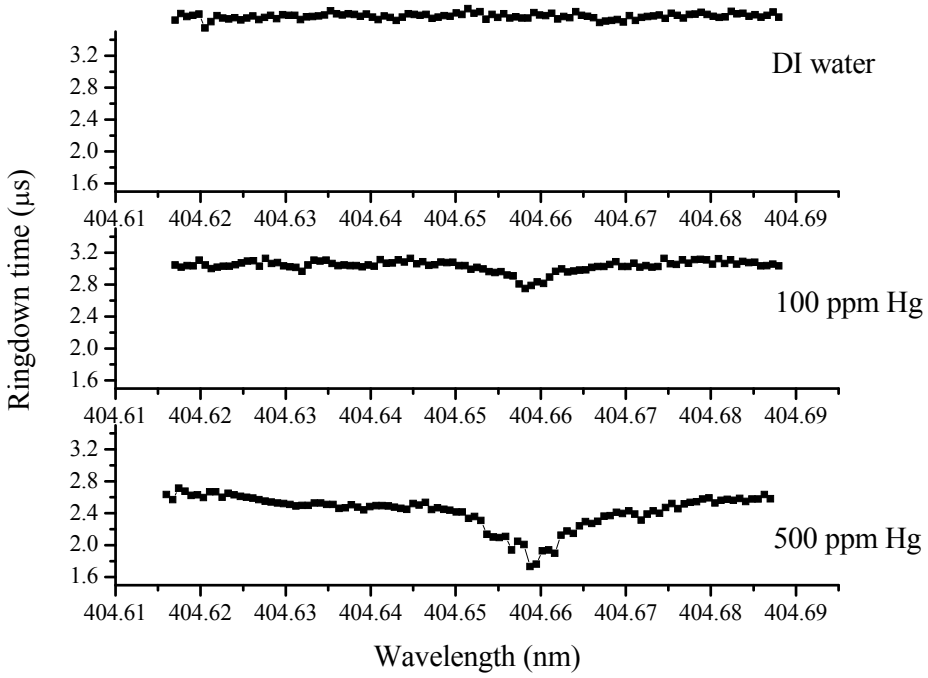

Figure 3.4 Cavity ringdown spectra of Hg around 405 nm.

The population of Hg in the ground state of the 405 nm transition was excited by energetic electrons created in the low power atmospheric pressure microwave plasma torch. Averaging over 100 ringdown events yielded the ringdown baseline stability of 0.4 % when the plasma was turned on. Electron energies in the low power (120 W) MPT ranged from 0.5 to 10 eV, and the estimated electron density was ~10^{12} electron cm^{-3} [10]. The atomic number density of Hg in the metastable 6s6p $^3P_0$ level was measured via the cavity ringdown technique:

$$n = \frac{d}{c\sigma_{abs} l}\left[\frac{1}{\tau} - \frac{1}{\tau_0}\right] \tag{3.7}$$

where σ_{abs} is the absorption cross section of the Hg atom at 404.657 nm, c is the speed of the light, d is the mirror spacing, l is the laser beam path-length in the plasma, and τ and τ_0 are the ringdown times with and without Hg samples in the plasma, respectively [11]. The absorption cross section of the 405 nm line was calculated to be 4.5×10^{-13} cm^2 $atom^{-1}$ based on a Voigt lineshape under the operational condition of the atmospheric plasma, whose plasma gas temperature was 2000 K. When a 50 ppm sample solution was introduced into the plasma torch, the measured ringdown times τ_0 and τ were 3.22 μs and 3.03 μs, respectively, from which the absolute number density of Hg in the 6s6p $^3P_0$ level was determined to be 5.26×10^8 atoms cm^{-3}, which was three orders of magnitude lower than the total Hg number density in the plasma, 3.75×10^{11} atoms cm^{-3}. In order to measure such low number density in the metastable state, the optical path-length needs to be 100 meters or longer if the conventional single-pass absorption spectroscopy is employed.

Using the measured number density of the metastable state and known experimental parameters, we solved the population rate equations for a four-energy system of Hg to obtain the EIECS. Figure 3.5 shows the four lowest energy levels of Hg. The population of Hg atoms in the energy levels higher than 10 eV was neglected since the upper limit of the electron energy in the low power microwave plasma was approximately 10 eV.

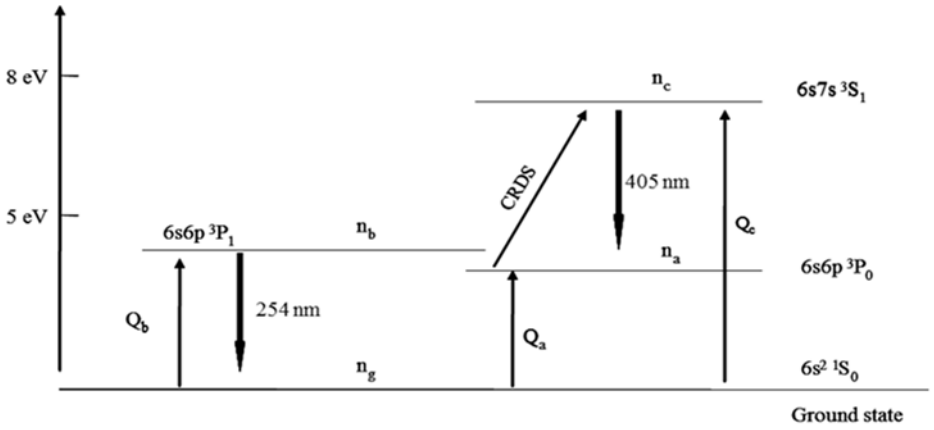

Figure 3.5 Diagram representing the schematic of the four-energy level system of Hg atom.

The rate equations for the four-energy level system, similar to the ones reported by Phillips *et al.* [1], can be written as:

$$\frac{dn_a}{dt} = n_g(n_e v)Q_a + \sum_{\substack{j>a \\ j\neq c}} n_j A_{ja} + n_c A_{ca} - B_{ac}\rho(\nu)n_a + B_{ca}\rho(\nu)n_c - n_a A_a \tag{3.8}$$

$$\frac{dn_b}{dt} = n_g(n_e v)Q_b + \sum_{j>b} n_j A_{jb} - n_b A_b \tag{3.9}$$

$$\frac{dn_c}{dt} = n_g(n_e v)Q_c + \sum_{j>c} n_j A_{jc} - n_c A_c - B_{ca}\rho(\nu)n_c + B_{ac}\rho(\nu)n_a \tag{3.10}$$

$$\frac{dn_g}{dt} = R(p) - n_g(n_e v)(Q_a + Q_b + Q_c) + \sum_{j>g} n_j A_{jg} \tag{3.11}$$

where Q_a, Q_b, and Q_c are the direct electron impact excitation cross sections for the 'a', 'b', and 'c' energy levels, respectively; n_a, n_b, n_c, and n_g are the Hg population densities of the 'a', 'b', 'c', and ground state energy levels; n_e and v are the electron

density in the plasma and electron drift velocity, respectively; $A_{ji}$and B_{ji} are the Einstein coefficients for spontaneous and stimulated transitions from the respective excited level 'j' to the corresponding lower level 'i'; $\rho(v)$ is the laser beam energy density; and $R(p)$ represents the rate at which Hg sample is being pumped into the plasma (atoms cm^{-3} s^{-1}). In the rate equations above, n_a is experimentally measured using CRDS as described above, $R(p)$ and $\rho(v)$ are known from the experiment, and A_{ji} and B_{ji} are calculated using the data from the NIST atomic database.

In this four-energy level rate equation model, the following assumptions were made: (i) Excitation to higher energy levels happen only through electron impact. (ii) De-excitation of an atom from a higher level to a lower level takes place only through optical emissions, namely, spontaneous emissions and/or stimulated emissions when laser radiation is present, e.g., in the case of CRDS measurements. (iii) All of the Hg atoms inside the plasma are distributed only among the four energy levels: 'g', 'a', 'b' and 'c';

$$n_{Total} = n_g + n_a + n_b + n_c \tag{3.12}$$

Therefore, under a steady state condition, the equations reduce to:

$$n_g(n_e v)Q_a^A + n_c A_{ca} - B_{ac}\rho(\nu)n_a + B_{ca}\rho(\nu)n_c - n_a A_a = 0 \tag{3.13}$$

$$n_g(n_e v)Q_b^A - n_b A_b = 0 \tag{3.14}$$

$$n_g(n_e v)Q_c^A - n_c A_c - B_{ca}\rho(\nu)n_c + B_{ac}\rho(\nu)n_a = 0 \tag{3.15}$$

$$R(p) - n_g(n_e v)(Q_a + Q_b + Q_c) + \sum_{j>g} n_j A_{jg} = 0 \tag{3.16}$$

where Q_i^A represents the apparent electron impact excitation cross section of level 'i' (i = a, b, c) and is defined as $Q_i^A = Q_i + \sum_{j>i} Q_{ji}$. In general, the optical emissions correlate to the electron excitation as

$$n_g(n_e v)Q_{ji} = n_j A_{ji} \tag{3.17}$$

Using the relative emission intensity ratio of the Hg 253.652 line to the Hg 404.657 line measured in the emission spectra in this experiment, η = 36, we have

$$\eta = \frac{I(253.652\,nm)}{I(404.657\,nm)} = \frac{n_b A_b}{n_c A_{ca}}. \tag{3.18}$$

When no laser beam is present in the plasma,

$$n_b A_b \propto n_g(n_e v)Q_b^A \tag{3.19}$$

$$n_c A_{ca} \propto [n_g(n_e v)Q_c^A + n_a(n_e v)Q_{ac} + n_b(n_e v)Q_{bc}] \tag{3.20}$$

The left-hand side of Eq. (3.19) represents the rate at which the energy level 'b' decays spontaneously, and the right-hand side represents the rate at which level 'b' is populated by the electron impact process. Similarly, $n_c A_{ca}$ in Eq. (3.20) represents the rate at which the energy level 'c' spontaneously decays to the metastable level 'a', and the terms in the right-hand side are the rates at which level 'c' is being populated by the electron impact excitation from the ground level 'g', energy level 'a', and energy level 'b', respectively. For a given energy level, the apparent electron excitation cross section is always greater than any other cross section (e.g., direct cross section, emission cross section). Along with that, the population density of the ground state energy level (n_g) of

an atom in a low power MPT remains significantly higher than the population density of any other higher energy level of that atom. Therefore, the first term on the right-hand side of Eq. (3.20) is sufficiently dominant than the other terms. Second term and onwards, therefore, can be neglected for their insignificant contribution. From Eqs. (3.19) and (3.20), we have

$$\frac{n_b A_b}{n_c A_{ca}} \cong \frac{Q_b^A}{Q_c^A} \tag{3.21}$$

Thus, from Eqs. (3.18) and (3.21), we have

$$Q_b^A = \eta Q_c^A \tag{3.22}$$

When the laser is switched on for the CRDS measurements, Eq. (3.18) is modified to be:

$$\frac{I(253.652nm)}{I(404.657nm)} = \frac{n_b A_b}{n_c (A_{ca} + B_{ca}\rho)} \tag{3.23}$$

In the case of CRDS experiments with a photon flux of 1.83×10^{17} photon cm^2 s^{-1} inside the cavity, the value of $B_{ca}\,\rho$ ($\sim 10^4$ s^{-1}) is sufficiently smaller than A_{ca}. Therefore, from Eqs. (3.18) and (3.23), we obtain a relation which is applicable to the cases when the laser radiation is present:

$$n_b = \eta(\frac{A_{ca} + B_{ca}\rho}{A_b})n_c \tag{3.24}$$

The calculated B_{ca} and B_{ac} are 5.26×10^{20} m^3 J^{-1} s^{-1} and 1.57×10^{21} m^3 J^{-1} s^{-1}, respectively.

Using the measured number density of the metastable state n_a and the derived relations expressed in Eqs. (3.22) and (3.24), we solved Eqs. (3.12) – (3.16) to obtain the EIECSs of the energy levels a, b, and c, as illustrated in Figure 3.5. The cross sections determined using this method are tabulated in Table 3.1.

Table 3.1 Measured electron impact excitation cross sections of the three lower energy levels of Hg, using the CRDS method (this work) vs. cross sections measured using other methods reported in the literature.

Electronic configuration	Cross section (cm^2) (This work) (Electron energy 0.5 – 10 eV)	Cross section (cm^2) (From literature) (Electron energy 4 – 10 eV)
6s6p $^3P_0$ (4.66 eV)	$(1.7 \pm 0.4) \times 10^{-17}$	$2.2 \times 10^{-17} – 3.1 \times 10^{-17}$ [Ref. 12] [a)] $7.5 \times 10^{-17} – 8.8 \times 10^{-17}$ [Ref. 12] [b)] $1.0 \times 10^{-17} – 3.5 \times 10^{-17}$ [Ref. 13]
6s6p $^3P_1$ (4.88 eV)	$(9.0 \pm 2) \times 10^{-17}$	$6.5 \times 10^{-18} – 1.4 \times 10^{-16}$ [Ref. 14] [c)] $1.0 \times 10^{-18} – 1.8 \times 10^{-16}$ [Ref. 15] [c)] $1.8 \times 10^{-18} – 2.3 \times 10^{-16}$ [Ref. 16] [c)]
6s7s $^3S_1$ (7.73 eV)	$(2.5 \pm 0.6) \times 10^{-18}$	$2.6 \times 10^{-18} – 5.9 \times 10^{-17}$ [Ref. 17] [c)] $2.6 \times 10^{-18} – 1.0 \times 10^{-16}$ [Ref. 18] [c)]

[a] From the distorted wave correction method; [b] From Born approximation method; [c] Taken from the review paper by Heddle *et al.* (Ref. 19).

For the metastable state, no experimental data for the electron energy less than 10 eV are available for a comparison; however, the cross section measured in this work is in good agreement with the theoretical calculations [12, 13]. One point to note is that the available literature data were obtained in a reduced pressure environment with mono-

electron energy in the range of 4 - 10 eV and the cross sections obtained in this work were obtained with averaged electron energy over the range of 0.5 - 10 eV in atmospheric plasma conditions; nevertheless, the measured cross sections in this work are still in good agreement with the values reported in a review article [19] which included cross sections obtained by different groups [14-18].

3.5 Conclusion

In conclusion, this study introduces a new optical method to measure electron impact excitation cross sections of atoms. The method described in this work can certainly be implemented with a mono-energy electron source in future work. The method demonstrated in this work for the Hg four-energy system that includes a metastable state can be readily applicable to a non-metastable three-energy level system for any other atom; in the non-metastable three-energy level system, the relative emission intensity ratio of the two transitions as used in Eq. (3.18) is not needed and the CRDS measurements alone can yield the direct determination of the cross sections of the three energy levels. This new method will be potentially a universal tool to help study electron-atom collision processes in extended experimental conditions, such as atoms in high pressure where implementation of the laser excitation fluorescence spectroscopy method is often hindered by the fluorescence quenching effect.

3.6 Acknowledgements

This work is supported by the National Science Foundation with grant No. CTS 0626302 and the Department of Energy with grant No. DEFC01006.

3.7 References

1. M.H. Phillips, L.W. Anderson, C.C. Lin, Phys. Rev. A 23 (1981) 2751-2753.

2. G.F. Hanne, V. Nickich, M. Sohn, J. Phys. B: At. Mol. Phys. 18 (1985) 2037-2047.

3. A.R. Filippelli, C.C. Lin, L.W. Anderson, J.W. McConkey, Adv. At. Mol. Opt. Phys. 33 (1994) 1-62.

4. R.O. Jung, J.B. Boffard, L.W. Anderson, C.C. Lin, Phys. Rev. A 80 (2009) 062708 1-13.

5. A. Chutjian, D.C. Cartwright, Phys. Rev. A 23 (1981) 2178-2193.

6. K. Blum, Density Matrix Theory and Applications, New York: Plenum, 1981, pp. 37-81.

7. T. Hadeishi, Ph.D. Dissertation, University of California, Berkeley, 1962.

8. A.A. Mityureva, N.P. Penkin, Opt. Spektrosk. 55 (1983) 393-395.

9. G. Berden, R. Englen, Cavity Ring-Down Spectroscopy: Techniques and Applications, Wiley Publications, 2009.

10. M. Schmidt, H. Conrads, in: R. Hippler, H. Kersten, M. Schmidt, K.H. Schoenbach (Eds.), Low Temperature Plasmas: Fundamentals, Technologies, and Techniques, WILEY-VCH, 1, 2008, pp. 363-383.

11. C. Wang, N. Srivastava, T.S. Dibble, Appl. Phy. Lett. 95 (2009) 051501-3.

12. J.N. Bass, R.A. Berg, A.E.S. Green, J. Phys. B: At. Mol. Phys. 7 (1974) 1853-1865.

13. S.D. Rockwood, Phys. Rev. A 8 (1973) 2348-2358.

14. H.M. Jongerius, Ph.D. Dissertation (University of Utrecht), Philips Research Reports Supplements No. 2., 1962.

15. T.W. Ottley, H. Kleinpoppen, J. Phys. B: At. Mol. Phys. 8 (1975) 621-627.

16. O.B. Shpenik, V.V. Souter, A.N. Zavilopulo, I.P. Zapesochnyi, E.E. Kontrosh, Sov. Phys. JETP 42 (1976) 23-27.

17. R.J. Anderson, E.T.P. Lee, C.C. Lin, Phys. Rev. 157 (1967) 31-40.

18. C. Smit, H.M. Fijnaut, Phys. Lett. 19 (1965) 121-122.

19. D.W.O. Heddle, J.W. Gallagher, Rev. Mod. Phys. 61 (1989) 221-278.

CHAPTER IV

DETECTION OF ELEMENTAL MERCURY WITH ELECTRON IMPACT EXCITATION-CAVITY RINGDOWN ABSORPTION SPECTROSCOPY USING 405 NM LASER WAVELENGTH.

4.1 Abstract

In this chapter we describe the measurement of elemental mercury (Hg) using the 405 nm transition line. The 405 nm (404.65 nm to be precise) transition line of Hg originates as a result of optical transition from the metastable state $5d^{10}6s6p\,^3P_0$ to the upper state $5d^{10}6s7s\,^3S_1$ of mercury. Observation of absorption spectra and measurements of the absolute number density of Hg in the metastable state were achieved by stepwise electron impact excitation-cavity ringdown absorption technique. In the first step, the Hg atoms were populated in the metastable state, i.e., $5d^{10}6s6p\,^3P_0$, through the electron impact excitation by energetic electrons (< 10 eV) generated in an atmospheric argon microwave plasma torch. Subsequently the detection of Hg was achieved via cavity ringdown spectroscopy (CRDS). The merit of this work is that it has introduced an -

---

Note: The major contents of this chapter have been adapted from J. Anal. At. Spectrom., 2012, 27, 284-292.

alternative way to measure Hg using a palm-size 405 nm laser source. This can potentially lead to a portable mercury ringdown spectrometer without constraints of importability of 254 nm laser sources. In comparison with the 254 nm line of Hg, the 405 nm line has no plasma-associated spectroscopic interferences, such as absorption of the OH rovibrational lines. One analytical limitation of the detection of Hg at 405 nm is the low detection sensitivity achieved in this exploratory study, 50 μg ml^{-1} in aqueous sample solutions, compared with the previously reported detection sensitivity of 9.1 ng ml^{-1} using the plasma-CRDS technique at 254 nm. Given an improved plasma excitation source-CRDS system, theoretical detection limits at 405 nm are estimated to be 50 ng ml^{-1} and 1.2 ppbv in aqueous samples and in gaseous samples, respectively. These sensitivities are still desirable in many applications when real-time, portable, and in-line analysis all become a major concern.

4.2 Introduction

In plasma cavity ringdown spectroscopy (plasma-CRDS), a plasma source, such as inductively coupled plasma (ICP) or a microwave plasma torch (MPT), is placed inside the ringdown cavity to generate atoms from the analytical compounds that are injected in the plasma and CRDS is utilized as a detector to quantify absolute concentrations of the atoms of interest [1-6]. In addition to the plasma atomization sources, a graphite furnace or a chemical reaction tube have also been implemented as an atomization source and coupled with CRDS to achieve atomic measurements [7-8]. Atoms can be also generated via sputtering, followed by the ringdown detection in the study of material processing [9]. While different atomization sources have been coupled

with CRDS for atomic measurements, a plasma atomization source has proven to be more attractive. To date, the plasma-CRDS technique has been demonstrated for its application to measure several environmentally important elements and isotopes, including Hg, Pb, Sr, Mn, Hg isotopes, ^{235}U, and ^{238}U. Detection sensitivities range from pg ml^{-1} to ng ml^{-1} (1 pg = 10^{-12} g, 1 ng = 10^{-6} g) [1-2, 10-16]. Although improving the detection sensitivity of the plasma-CRDS technique is still under study, one challenging issue that needs to be addressed is the instrumental portability of the plasma-CRDS-based spectrometers. Currently no single *portable* plasma-CRDS spectrometer has been reported, mainly due to the high cost and bulky geometry of the laser source, given the fact that a compact, automated plasma source has recently become available [17]. Using measurements of elementary mercury (Hg (I) or Hg) as an example, we have found that the majority of atomic absorption spectral measurements of Hg have been carried out using the well-known 254- nm transition line. The transition line has been used in cold vapor atomic absorption spectroscopy (CV-AAS) [18], atomic fluorescence spectroscopy (AFS) [19], differential optical absorption spectroscopy (DOAS) [20], laser atomic absorption spectroscopy (LAAS) [21], and atomization source coupled-CRDS [8, 14-15, 22]. A Hg 254-nm lamp is typically used as the light source for low sensitivity atomic absorption analysis; however, for high sensitivity spectral measurements of Hg at 254 nm, a laser source, such as an Nd:YAG-pumped dye laser, a frequency doubled diode laser, a frequency mixing of two diode laser, or a narrow linewidth (OPO) system, must be used. One noticeable barrier in the development of a portable mercury spectrometer is the aforementioned bulky and expensive 254-nm laser source [23], which makes field-deployable instrumentation practically impossible. There are two possible ways to

circumvent this obstacle: the development of a new generation 254 nm compact light source or the use of a different Hg transition line, in which a relatively inexpensive, compact laser source operating at that wavelength is currently available. The objective of this study is to investigate a new absorption spectral method to detect Hg using the 405 nm transition line, in which a palm-sized, single wavelength (405 nm) diode laser has recently become available.

Unlike that of the 254-nm transition, the lower state of the 405-nm transition is a metastable state- $5d^{10}6s6p^3P_0$ [24]; therefore, a technique must be implemented to efficiently populate Hg atoms in the metastable state prior to the absorption of the Hg atoms. Additionally, the atomic number density in a metastable state is typically 10^3 - 10^5 times lower than the number density in the ground state [25]. Thus, direct measurements of number densities of Hg in the metastable state become very challenging if the total Hg number density is low. Very few publications have reported measurements of number density of Hg in the metastable state. Uhl *et al*. attempted to measure Hg at 404.657 nm (the 405 nm line) using the wavelength modulation diode laser AAS method, in which the $5d^{10}6s6p^3P_0$ metastable state were populated through radio frequency-induced low pressure discharge. However, no detectable absorption was observed even though high concentrations of mercury were used [26]. Horiguchi and Tsuchiya claimed that they detected Hg in the $5d^{10}6s6p^3P_0$ metastable state in the study of quenching cross sections of Hg ($5d^{10}6s6p^3P_0$, $5d^{10}6s6p^3P_1$) with various quenching gases in a low pressure gas cell. However, no measured number densities of Hg in the $5d^{10}6s6p^3P_0$ metastable state were reported in the paper [27]. An earlier publication reported a study of the collision process of electrons with Hg atoms in the metastable state using the electron

impact excitation-laser excitation fluorescence technique, but no absolute number density of Hg was quantified [28]. To the best of our knowledge, spectroscopic data, such as absorption cross section, possible spectral interferences, etc., on the Hg 405 nm line are not available; neither a theoretical detection sensitivity nor an experimental one of the detection of Hg at 405 nm using a laser absorption spectral technique has been reported to date.

In the present work, we describe a new approach, namely, a stepwise electron impact excitation-cavity ringdown absorption spectrometry (SEIE-CRAS) to directly measure Hg at 405 nm. Similar approaches have been reported recently to measure fluorine atoms and to study electron impact excitation cross sections of Hg [29-30], but this work focuses on the study of spectroscopic fundamentals in the detection of Hg using SEIE-CRAS at 405 nm and the method of the spectrometry, which is potentially applicable to measuring other environmentally important elements and isotopes. Section 4.2 introduces the principle of the SEIE-CRAS technique to detect Hg at 405 nm. Section 4.3 describes the experimental system, and Section 4.4 reports measurements of Hg at 405 nm using the SEIE-CRAS with a tunable narrow-linewidth OPO laser and a palm-size single wavelength diode laser, and discussion. Subsequently conclusion has been presented. Absolute number densities of Hg in the metastable state are determined using a calculated absorption cross section of the 405 nm line; detection sensitivity, proposed improvement, and potential spectral interferences are discussed.

4.3 4.2 Principle of the Stepwise Electron Impact Excitation-Cavity Ringdown Absorption Spectrometry for Mercury

Figure 4.1 shows a schematic of the four-energy states of elemental mercury relative to the two transition lines at 254 and 405 nm. The lower state of the 405 nm transition, $5d^{10}6s6p^3P_0$, is a metastable state and has an energy of 37645 cm^{-1} (1 eV = 8066.2 cm^{-1}) while the lower state of the 254 nm transition, $5d^{10}6s^{21}S_0$, has an energy of zero cm^{-1} [24]. Observation of the Hg absorption at 405 nm requires excitation of Hg from the electronic ground state, $5d^{10}6s^{21}S_0$, to the metastable state prior to the cavity ringdown measurements of Hg. In the SEIE-CRAS technique, an atmospheric microwave plasma torch is employed as an atomization source to generate Hg atoms from standard analytical Hg solutions and also functions as an electron impact excitation source to excite Hg atoms to the $5d^{10}6s6p^3P_0$ metastable state that is then probed by cavity ringdown spectroscopy. The number density of Hg in the metastable state is dependent on the electron impact excitation cross section of the state and the total Hg number density in the plasma [30-31]. Under a careful control of the experimental parameters, such as plasma power, plasma gas flow rate, sample introduction rate, and laser beam position, the number density of Hg in the metastable state is approximately constant when the Hg energy system reaches a steady state, which can be experimentally achieved. The experimental design is based on the following principles:

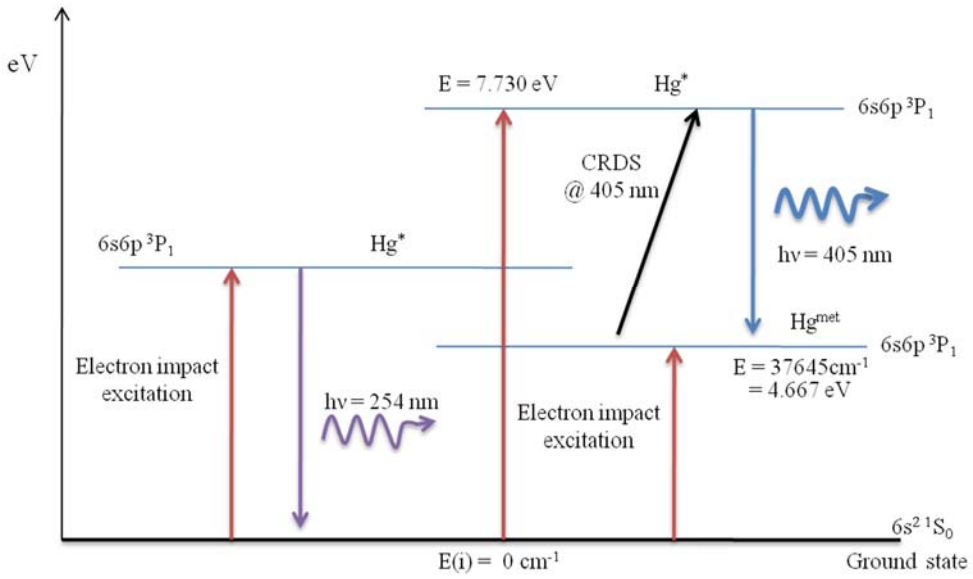

Figure 4.1 Schematic of the four-energy level system related to the transitions of Hg at 254 and 405 nm.

$$e\ (> 4.667\ eV) + Hg\ (5d^{10}6s^2\ {}^1S_0) \rightarrow Hg^{met}\ (5d^{10}6s6p\ {}^3P_0) + e \tag{4.1}$$

$$e\ (> 7.730\ eV) + Hg\ (5d^{10}6s^2\ {}^1S_0) \rightarrow Hg^*\ (5d^{10}6s7s\ {}^3S_1) \rightarrow Hg^{met}\ (5d^{10}6s6p\ {}^3P_0) + h\nu\ (\text{at } 405\ nm) + e \tag{4.2}$$

$$Hg^{met}\ (5d^{10}6s6p\ {}^3P_0) + h\nu\ (\text{at } 405\ nm) \xrightarrow{CRDS} Hg^*\ (5d^{10}6s7s\ {}^3S_1) \tag{4.3}$$

$$n = \frac{d}{c\sigma_{abs}l}\left[\frac{1}{\tau} - \frac{1}{\tau_0}\right] \tag{4.4}$$

where Hg* and Hg^{met} denote the excited state and the metastable state, respectively. 4.667 eV is the excitation threshold energy of the metastable state [24, 32-33]. Electron impact excitation of higher Hg states requires larger electron energies, for instance, >7.730 eV is needed for excitation of the $5d^{10}6s7s\ {}^3S_1$ state. Note that the metastable state population is determined by the apparent excitation cross section which includes the

direct excitation cross section and the cascade excitation cross section [31, 34]. Equation (4.1) relates to the direct excitation process and equation (4.2) relates to the cascade excitation process. Both processes contribute to the net excitation effect of Hg in the metastable state. Equation (4.3) represents the ringdown absorption process. In equation (4.4), n is the atomic number density of Hg in the metastable state to be measured via the cavity ringdown technique. σ_{abs} is the absorption cross section of Hg at 404.657 nm, c is the speed of the light, d is the mirror spacing, l is the laser beam pathlength in the plasma, and τ and τ_0 are the ringdown times with and without Hg sample in the plasma respectively. The entire SEIE-CRAS process is governed by Equations (4.1) to (4.3) and quantification of the atomic number density of Hg in the metastable state is determined via Equation (4.4).

4.4 Experimental System

The schematic of the experimental system used in the experiment have been shown in Fig. 4.2. The major part of the setup consists of two laser units, a microwave plasma source, a cavity ringdown system, an optical emission spectrometer, and a sample introduction portion. The specifications and the arrangement of different parts of the experimental setup are being described in detail in the subsequent section.

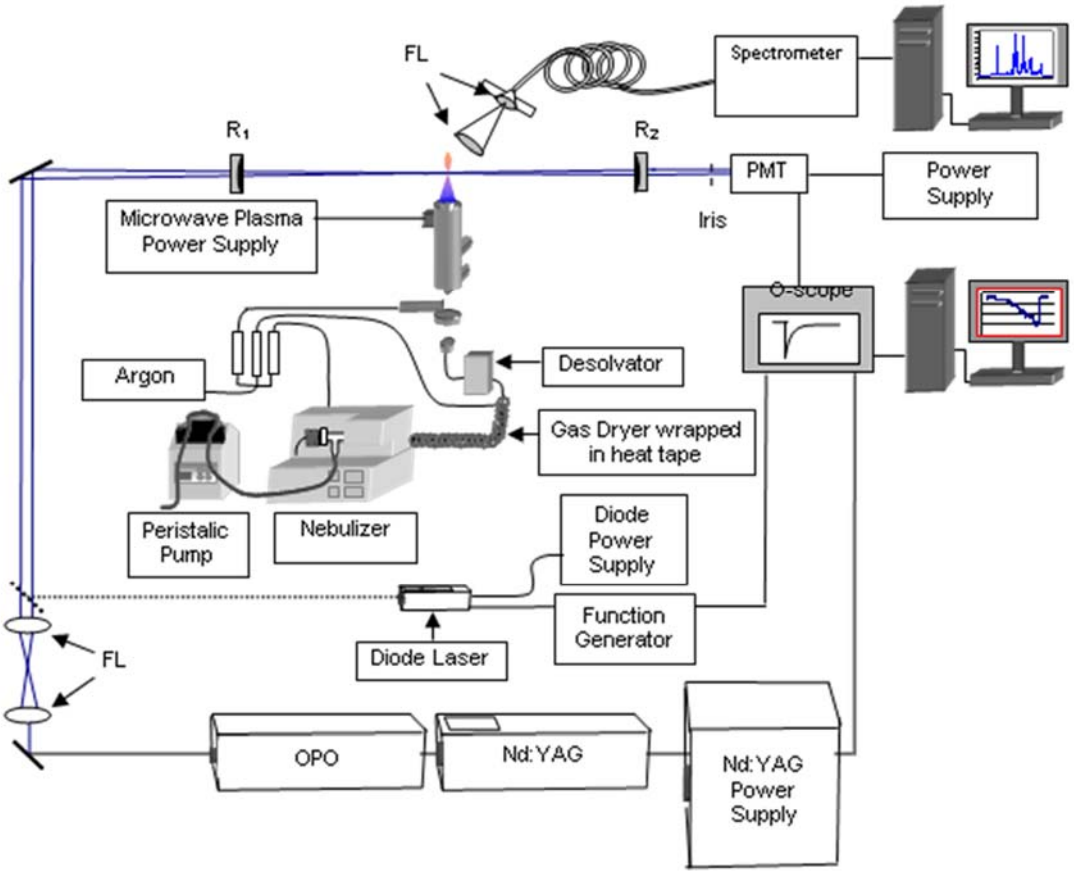

Figure 4.2 Schematic of experimental setup.

(i) Laser systems: Two laser sources, namely MOPO-HF-FDO (SpectraPhysics) and a diode laser (CrystaLaser) were employed to generate laser beams at 405 nm. The MOPO-HF-FDO which was operated at 20 Hz with a narrow linewidth (0.075 cm^{-1} at 500 nm), was used as the tunable light source for spectral scanning around 405 nm. In order to map out the atomic transition line of Hg, the scanning step of the MOPO laser was set at 0.001 nm/step. The diode laser was custom-designed for single wavelength 404.657 nm to be employed for ringdown measurements of mercury. The laser diode was externally triggered to generate a series of laser pulses with a repetition rate of 10 Hz, a

typical linewidth of < 0.006 cm^{-1}, and a single pulse energy of 3 to 5 μJ. The laser wavelengths were monitored by a UV wavemeter (Burleigh WA-5500).

(ii) Plasma-CRDS setup: A ringdown cavity of length 50 cm was constructed using a pair of plano-concave mirrors. The reflectivity of the mirrors was measured to be 99.91% at 405 nm. The microwave plasma torch (MPT), positioned at the center of the cavity, was excited by a 2.45-GHz microwave power generator. The experiments were conducted at plasma power of 150 W. 99.99% pure argon gas (Airgas) was used for both the purposes, namely plasma support and as the sample carrier gas. In addition it was also used to back flow in the membrane tube connected to the desolvator. A constant supply of the argon gas was maintained for a sustained plasma. The argon gas flow rates in the three gas flow channels were 0.5, 0.5, and 1.0 liter per minute (lpm), respectively. The average electron energy in this microwave plasma torch was in the range of 3 to 5 eV, and the electron density was ~10^{12} electron cm^{-3} [35-36]. The laser beam path-length in the plasma was in the range of 2 to 5 mm, depending on the location of the laser beam in the plasma.

(iii) Sample injection: The samples were injected into the plasma in the form of aerosol using argon as the carrier gas. Mercury sample solutions of different concentrations were generated via dilutions of the standard 1000 μg ml^{-1} Hg aqueous solution (Absolute Standards, Inc.,) with a 2% nitric acid solution.

The liquid solution was first injected into an ultrasonic nebulizer (U-5000 AT^{+}, CETAC Technology) using a peristaltic pump. The sample uptake rate by the peristaltic pump was 1 mL min^{-1}. The nebulizer, operating at the heating temperature of 140 ^{0}C and cooling temperature of - 4 ^{0}C, generates fine wet aerosols of the mercury solution with an

efficiency of around 10%. The aerosols so generated, were carried to the MPT by a flowing stream of argon gas at the flow rate of 0.5L min^{-1}. In order to get rid of the excess moisture present with the sample, a desolvator membrane tube wrapped with a heating tape, was used to carry the aerosol sample + carrier gas mixture from the nebulizer outlet to the MPT. A back flow of argon, flow rate 0.5 L min^{-1}, was used to absorb the moisture separated out of the desolvator membrane. Furthermore, the aerosol + gas mixture coming out of the desolvator tube was passed through a box filled with moisture absorbing granules, to remove excess water vapor. Here, it would be worth mentioning that microwave plasmas are very sensitive to moisture. The presence of moistures destabilizes the plasma severely, which in turn could hamper its efficiency to atomize and excite the sample atoms present in the plasma.

4.5 Results and Discussion

4.5.1 SEIE-CRAS Using the Tunable MOPO Laser Source

The cavity ringdown spectra of Hg around the 404.657 nm transition line (the 405 nm line) obtained using the SEIE-CRAS technique is shown in Figure 4.3, which so far is the first report on laser absorption spectra of Hg at 405 nm using the electron impact excitation coupled with CRDS. In the present study, the lowest mercury concentration at which a distinct Hg absorption peak could be recognized was 75 μg ml^{-1}. Each data point in the scans, shown in Fig 4.3, is an average of 100 ringdown events. The baseline noise obtained with no plasma present in the ringdown cavity was 0.4%, whereas with plasma ON, operating at 150 W, the base line was recorded to be approximately 0.6%.

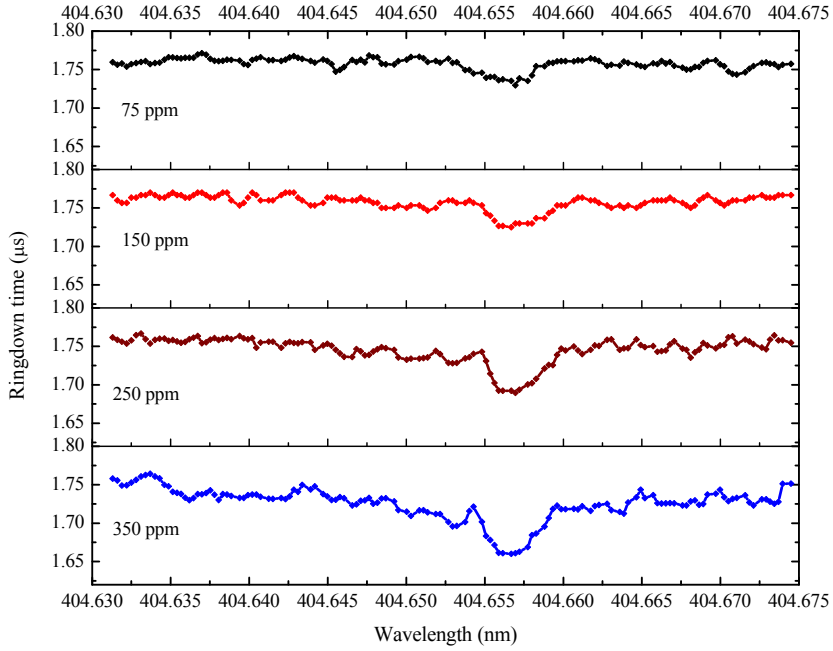

Figure 4.3 Absorption spectra of Hg around 405 nm using stepwise electron impact excitation-cavity ringdown absorption spectrometry

The ringdown scans were conducted from wavelengths around 404.630 nm to 404.675 nm. As shown in the figure, the absorption dip in the vicinity of 404. 65 nm became more and more apparent as the solution concentration of Hg was increased from 75 μg ml^{-1} to 350 μg ml^{-1}. The small kinks in the absorption dip suggest the probable presence of isotopes of mercury in the sample solution. The results in Fig. 4.3 show that the proposed method of the SEIE-CRAS to detect Hg at 405 nm is successfully demonstrated.

Once the Hg absorption spectra were obtained with the MOPO system, the ringdown system's response to different sample concentrations at the Hg absorption peak (404.657 nm) was also examined. Figure 4.4 shows the measured ringdown times versus

the different sample concentrations in the range of 50 to 500 μg ml^{-1}. Higher concentrations were not measured due to the radiation trapping effect of Hg [37-38]. The results in Figure 4.4 show that the plasma-CRDS system has a fast response to a change in the sample concentration. Typically, a response is observed in less than 30 seconds after the sample vapor is generated. This includes the 15 seconds required for the gas to flow through the sampling tubing and the time required by the software to average and fit the detected signal. As can be seen in Figure 4.4, the lowest detected concentration of the aqueous solution is 50 μg ml^{-1}, and the signal has good reproducibility as shown by the repeatable ringdown times measured in the presence of the blank solution (2% nitric acid solution) at the beginning and end of the entire measurement series.

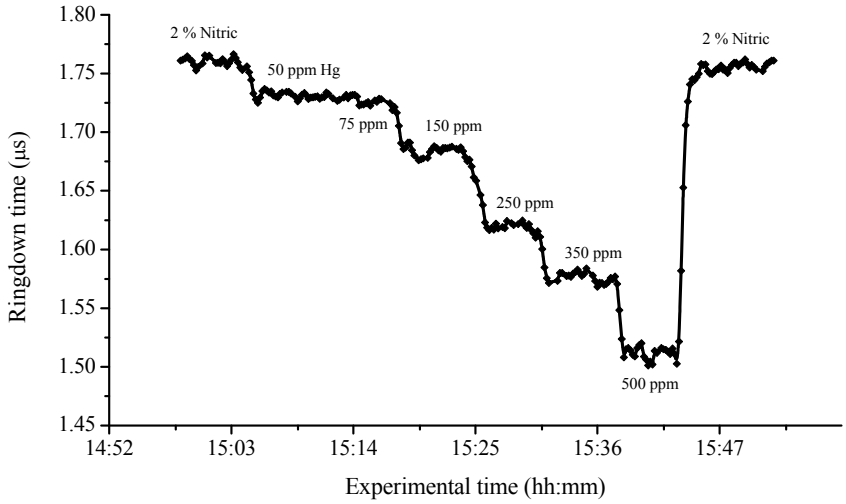

Figure 4.4 Ringdown measurements of Hg at 405 nm in the different solution concentrations with OPO system.

Note that the measured ringdown times reflect the absolute Hg number densities in the metastable state but may not proportionally reflect the concentrations of the Hg sample solutions used because of the multiple channel processes as illustrated in Figure 4.1. It is crucial for analytical instrumentation to examine this speculation, since the ultimate output of an analytical instrument displays the analyte's concentration in an actual sample solution of interest, such as the aqueous solution concentrations in this study. Figure 4.5 shows the calibration curve of the measured absorbance of Hg versus the sample solution concentration in the range of 50 – 500 μg ml^{-1}. Good linearity (R^2 = 0.997) was obtained. The linear behavior shown in Figures 4.5 supports the argument that under current experimental conditions, the absolute number density of Hg in the metastable state is proportional to the concentration of Hg sample solution. This result indicates that the Hg aqueous solutions can be analyzed through measuring the absolute number density of Hg in the metastable state using the SEIE-CRAS technique.

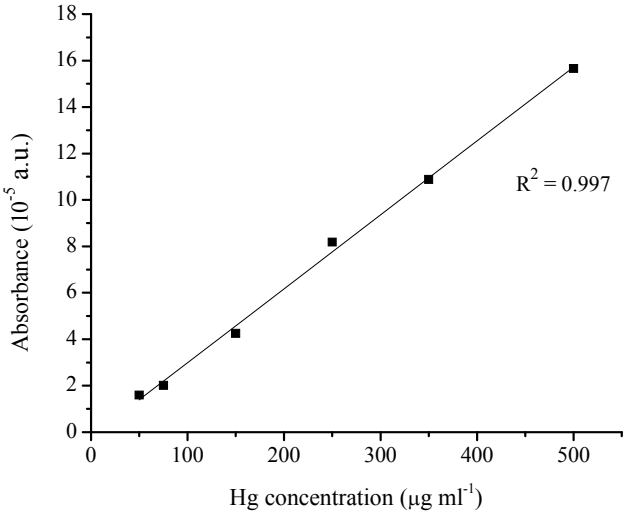

Figure 4.5 A calibration curve of Hg sample solutions

4.5.2 SEIE-CRAS Using the Palm-size 405 nm Diode Laser

The measurements of Hg at 405 nm were also carried out using the custom-designed, compact, and single wavelength diode laser. The purpose of this experiment was to validate the technological feasibility a portable plasma-ringdown Hg spectrometer using the palm-size laser source. The same wavemeter described above was used to monitor the diode laser wavelength to ensure the laser was operating at the Hg absorption peak, 404.657 nm. Figure 4.6 shows the measurement results of a 100 μg ml^{-1} aqueous solution using the 405 nm diode laser source. In the experiment, the laser head was not housed in a thermal controlled chamber. A minimal drifting of the laser wavelength around 404.657 nm generated large noise in the ringdown signals, as shown in Figure 4.6.

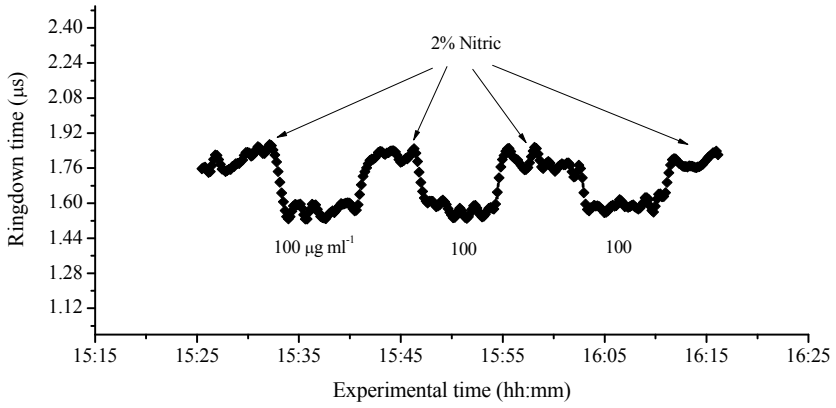

Figure 4.6 Ringdown measurements of 100 μg ml^{-1} of Hg at 405 nm with a palm-size diode laser

(Plasma power = 150 W; gas flow rates = 0.5, 0.5, 1.0 lpm)

However, the reproducibility of the signals was apparent. A similar calibration curve as shown in Figure 4.3 was also obtained using the diode laser. The results are

shown in Figure 4.7. The experimental detection sensitivity was estimated to be 50 μg ml^{-1}.

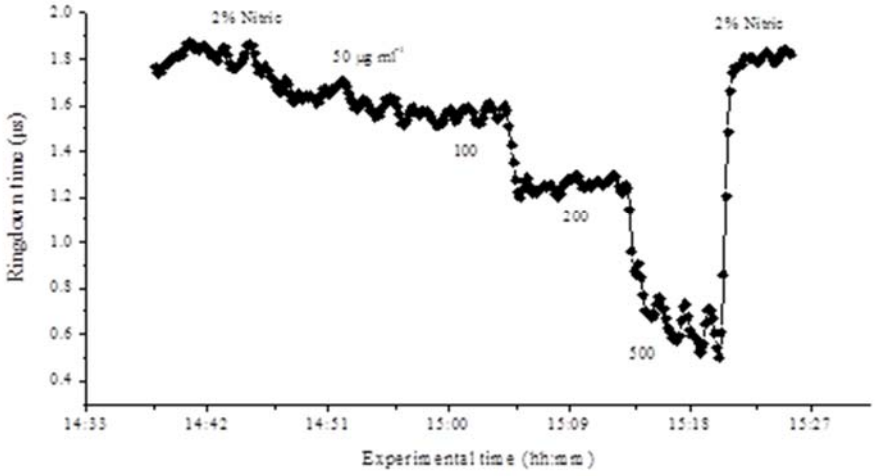

Figure 4.7 Measurements of Hg at 405 nm in the different solution concentrations with palm size diode laser.

The system's response to difference aqueous solution concentrations showed good linearity (R^2 = 0.996), as shown in Figure 4.8. The analytical merit of the data shown in Figures 4.6 – 4.8 will be improved in future studies. Yet, the results in Figures 4.6 – 4.8 demonstrate that mercury was successfully detected using the SEIE-CRAS technique with the palm-size laser source.

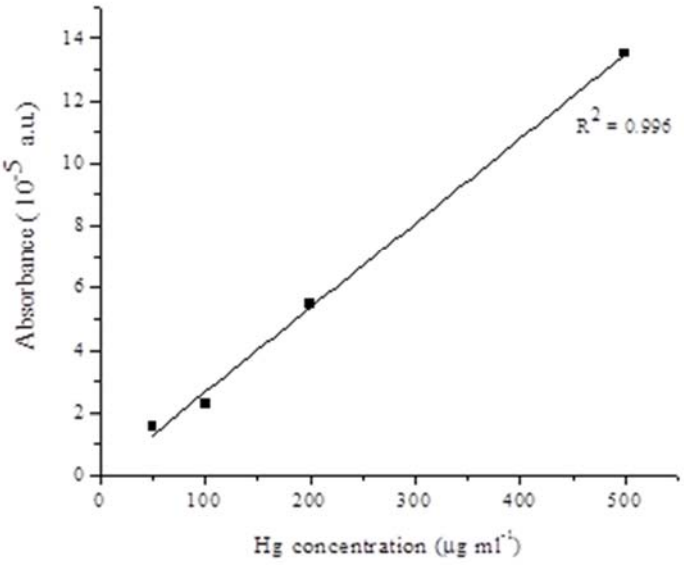

Figure 4.8 A calibration curve of Hg sample solutions at 405 nm with the diode laser

4.5.3 Measurement of Absolute Number Densities of Hg in the Metastable State

Absolute number densities of Hg measured in each of the sample concentrations were determined by inserting the measured ringdown times into Equation (4.4). The optimized laser pathlength in the plasma was 5 mm. No experimental data on the absorption cross section of Hg at 405 nm is available; however, the absorption cross section can be calculated based on the following equation [39-40]:

$$\sigma_{ij} = \frac{g_j}{g_i} \frac{\lambda^4}{4\pi^2 c} \frac{A_{ji}}{w_G} V(a,0)(\pi \ln 2)^{\frac{1}{2}} \tag{4.5}$$

where g_j and g_i are the upper and lower state degeneracies respectively; λ is the transition wavelength; c is the speed of light; A_{ji} is the spontaneous emission transition

rate; and w_G is the Gaussian component of the lineshape caused by Doppler broadening. Under the operational conditions of the atmospheric plasma, whose plasma gas temperature was ~ 2000 K, the lineshape is a predominantly Doppler broadened lineshape, and the value of $V(a,0)$ is close to 1 [41]. For the mercury 405 nm line, g_j/g_i = 3 and $A_{ji} = 2.1 \times 10^7$ s^{-1} [24]. This yields an absorption cross section of 4.5×10^{-13} cm^2 atom^{-1}. When a 50 μg ml^{-1} aqueous sample solution was introduced into the ultrasonic nebulizer, the measured ringdown times τ_0 and τ were 1.761 μs and 1.732 μs, respectively, from which the absolute number density of Hg in the 6s6p $^3P_0$ metastable state was determined to be 7.09×10^7 atoms cm^{-3} using the calculated absorption cross section. Similarly, the absolute number densities corresponding to other sample concentrations were also determined using the measured ringdown times. Table 4.1 lists the measured absolute number densities of Hg in the metastable state and the corresponding ringdown times, absorbance, sample solution concentrations, and total Hg in the plasma.

Table 4.1 The absolute number densities of Hg in the metastable state measured by the stepwise electron impact excitation-cavity ringdown absorption technique using the 405 nm line.

Hg sample concentration ($\mu g\ ml^{-1}$)	Total Hg number density in the plasma (atoms cm^{-3})	Ringdown time (μs)	Absorbance (10^{-5} a. u.)	Number density of the metastable state (atoms cm^{-3})	Ratios of total Hg in the plasma to Hg in the metastable state (± 10)
50	3.75×10^{11}	1.732	1.60	7.09×10^{7}	5300
75	5.62×10^{11}	1.724	2.02	8.97×10^{7}	6260
150	1.12×10^{12}	1.685	4.26	1.89×10^{8}	5930
250	1.87×10^{12}	1.621	8.19	3.64×10^{8}	5140
350	2.62×10^{12}	1.579	10.88	4.84×10^{8}	5410
500	3.75×10^{12}	1.511	15.66	6.96×10^{8}	5390

(The ringdown baseline was 1.761 μs when the plasma was ON)

As can been seen in Table 4.1, the lowest number density of Hg measured in the metastable state was 7.09×10^{7} atoms cm^{-3}, which corresponds to a concentration of 50 $\mu g\ ml^{-1}$ in the sample solution. Given the 0.75 ml per minute pumping rate of the sample solution into the ultrasonic nebulizer (with a 10% nebulizer efficiency) and the known sample introduction gas flow rate, the total Hg number density generated in the plasma can be estimated. Using the same estimation method as reported elsewhere [2, 12-13, 16], the total Hg number density in the plasma was 3.75×10^{11} atoms cm^{-3}. The estimated total Hg number densities in the plasma for other sample solutions are also listed in Table 4.1. Column 6 lists the ratios of the total number densities to the metastable state number densities. Comparison of this total number density with the measured absolute number density of Hg in the metastable state shows that the number density of Hg in the

metastable state is ~ 10^3 - 10^4 times lower than that of the ground state. These low metastable state number densities (10^7 - 10^8 atoms cm^{-3}) are not detectable using the conventional single-pass AAS technique [26].

4.5.4 The Detection Sensitivities of Hg at 405 nm and Comparisons to the Detection Sensitivities at 254 nm

The detection sensitivity of Hg can be defined as the detection sensitivity of Hg in aqueous solutions in terms of $\mu g\ ml^{-1}$ or the detection sensitivity of Hg in gas samples in terms of a partial gas volume, such as ppmv, ppbv or pptv. In this study, the achieved detection sensitivity in terms of the concentration of the aqueous sample solution is approximately 50 $\mu g\ ml^{-1}$, which corresponds to an equivalent detection sensitivity of a 1.2 ppmv of Hg in a gas sample. These detection sensitivities are significantly lower than 9.1 $ng\ ml^{-1}$ in aqueous solutions and 0.2 ppbv in gas samples, as previously reported in the measurements of Hg using the plasma-CRDS technique at 254 nm [15]. The low detection sensitivity of Hg at 405 nm suggests that the Hg 405 nm absorption line should be cautiously utilized if the pursuit of high detection sensitivity is a major analytical goal. In recent years, several studies have reported measurements of Hg using CRDS at 254 nm coupled with different Hg sources; different detection sensitivities were obtained due to the use of different Hg sources, mirror reflectivity, and ringdown cavity lengths [8, 14-15, 22, 42-44]. The details of the different detection sensitivities are listed in a table in a recent report [42]. However, to the best of our knowledge, neither an experimental detection sensitivity nor a theoretical one of Hg using the 405 nm line is available for a comparison with the results obtained in the present study.

It would be interesting to estimate and compare theoretical detection sensitivities of Hg using the 405 nm and 254 nm lines in a single optimized plasma-ringdown system. The optimized system is defined as an experimental setup that is built toward the best detection sensitivity by using ringdown mirrors of higher reflectivity at 405 nm and different configurations of the plasma source allowing a longer laser beam pathlength in the plasma. The minimum detectable absorbance of a ringdown system is given by [2-6]

$$\text{Minimum detectable absorbance} = \sigma_{abs} nl = (1-R)\frac{\sigma_\tau}{\tau} \tag{4.6}$$

where σ_τ is the standard deviation of ringdown time τ and $\frac{\sigma_\tau}{\tau}$ is defined as the ringdown baseline noise or the baseline stability, which is determined by the ringdown system alignment and the system's electronic noise limit. An experimentally achievable value of $\frac{\sigma_\tau}{\tau}$ for a plasma-CRDS system can be as low as 3×10^{-3} [12, 14]. Mirror reflectivity in the upper UV – VIS wavelength region is typically lower than that in the near-infrared, but it can realistically approach 99.99%. Inserting these two parameters into Equation (4.6) yields a minimum detectable absorbance of the plasma ringdown system of 3×10^{-7} (a. u.). From the calculated absorption cross section (4.5×10^{-13} cm^2 atom^{-1}) of Hg at 405 nm and the laser pathlength (l = 10 cm) in the plasma, the minimum detectable absorbance yields a number density of 6.66×10^4 atoms cm^{-3}, the lowest detectable number density of Hg. Although the laser path-length in the plasma is only 5 mm in the present study, a 10-cm laser pathlength in a slit plasma sheet has been reported [45]. The lowest detectable number density in the metastable state gives a theoretical

detection sensitivity of 50 ng ml^{-1}, which is equivalent to a detection sensitivity of 1.2 ppbv in gas samples, based on the determined relations shown in Table 4.1.

The calculated absorption cross section of Hg at 254 nm is 2.64×10^{-14} cm^2 $molecule^{-1}$ [15], which is slightly smaller than the earlier reported experimental value of 3.3×10^{-14} cm^2 $molecule^{-1}$ [43], but larger than the most recently reported experimental value of 2.4×10^{-14} cm^2 $molecule^{-1}$ [42]. Using the same mirror reflectivity (99.99%), the same baseline noise (3×10^{-3}), and the same laser pathlength (10 cm) in the aforementioned estimates, we obtain a detection sensitivity for Hg aqueous sample solution of approximately 200 pg ml^{-1} or a 4.8 pptv for Hg in gas samples if the 254 nm line is used. A comparison of the two estimated detection sensitivities shows that the detection sensitivity of Hg using the 254 nm line is theoretically ~ 250 times better than that when using the 405 nm line. The factor of 250 comes from the combined effect of the fact that the Hg number density in the lower state of the 254 nm transition is approximately 5000 times higher than the number density in the lower state of the 405 nm transition and that the absorption cross section of Hg at 254 nm is approximately twenty times smaller than that of 405 nm line. The details of the theoretical estimates of the detection sensitivities of the two transition lines and their comparisons are listed in Table 4.2. The data shown in Table 4.2 may be useful references when two Hg absorption lines are considered for different analytical applications, such as when instrument *portability* becomes a major concern, the detection sensitivities of 50 ng ml^{-1} in aqueous solution or 1.2 ppbv in gas samples may be still desirable in many field applications.

Table 4.2 Comparison of the theoretical detection sensitivities of Hg at 405 nm and at 254 nm.

Wavelength (nm)	Number density in the lower state	Laser path-length in the plasma (cm)	Ringdown baseline noise, $\frac{\sigma_\tau}{\tau}$	Mirror reflectivity	Absorption cross section (cm^2)	Detection sensitivities	
						In aqueous solutions	In gas samples
254	*n*	10	0.003	99.99%	2.4×10^{-14}	200 pg ml^{-1}	4.8 pptv
405	*n*/5000	10	0.003	99.99%	4.5×10^{-13}	50 ng ml^{-1}	1.2 ppbv

4.5.5 4.4.5. Discussion on Spectroscopic Interferences Using the SEIE-CRAS Technique at 405 nm

The issue of spectral interference when using the 405 nm line for Hg detection becomes much less critical than when using the 254 nm line, where two rovibrational transitions-$R_{21}(21)$ and $P_1(15)$ of the OH A-X (3-0) band are located [15, 46]. Under the plasma conditions, these two broadened molecular transitions are overlapped into a single peak centered at 253.650 nm. The Hg atomic transition, 253.657 nm, is located on the shoulder of this interference peak. When measurements of Hg using the 254 nm line approach the detection limit, this spectral interference becomes an important issue whereas the effect on high concentration measurements (the μg ml^{-1} - ng ml^{-1} levels) is negligible. Typical species generated in the atmospheric argon microwave plasma include OH, N_2^*, N_2^+, NO, NH, Ar, O, and H [36]. These species have none or negligible absorption at 405 nm. This fact offers interference-free measurements of Hg at 405 nm and is an advantage of using the 405 nm line. However, in real applications a sample solution often contains multiple elements, possible spectral interferences resulting from the absorption lines around 405 nm of the elements and their associated ions must be

considered. Table 4.3 lists all possible transition lines of elements and ions in the vicinity of the Hg 405 nm and 254 nm lines [24]. The full width at half maximum (FWHM) of the Hg absorption lines at 405 nm and 254 nm under the atmospheric pressure microwave plasma condition is approximately 0.0025 nm [15]. Theoretically, a minimum wavelength separation of 2 FWHM is required to resolve two transition lines. Experimentally, when a wavelength separation between two transition lines is less than 3 FWHM, the two transition lines can be barely resolved. Therefore, the elemental transition lines that have a wavelength separation of $\leq$ 5 FWHM are all listed in the table.

Table 4.3 Absorption lines of the elements and ions in the vicinity of ± 5 FWHM around the Hg transition lines at 405 nm and 254 nm.

(One FWHM of the Hg absorption linewidth at 254 nm or 405 nm under the atmospheric microwave plasma condition is approximately 0.0025 nm.)

Elements and ions	Transition wavelength (nm)	Distance to the Hg 405 nm line (nm)	Distance to the Hg 405 nm line (FWHM)
Transition lines in the vicinity of Hg 405.657 nm ± 5 FWHM			
Sc	404.648	0.009	4
Hg	404.657	0.000	0
Pr (II)	404.663	0.006	2
Se (III)	404.670	0.013	5
W (II)	404.670	0.013	5
W	404.670	0.013	5
Transition lines in the vicinity of Hg 253.657 nm ± 5 FWHM			
Fe	253.644	0.013	5
Pt	253.649	0.008	3
Co	253.649	0.008	3
Hg	253.657	0.000	0
W (II)	253.661	0.004	2
Fe (II)	253.667	0.010	4

As shown in Table 4.3, five elements and ions (Sc, Pr (II), Se (III), W, and W (II)) have absorption lines located within ± 5 FWHM away from the Hg line at 404.657 nm [24]. Similarly, five transition lines in the vicinity of the Hg 254 nm line are also identified and tabulated in Table 4.3. The information from Table 4.3 suggests that

although the detection of Hg at 405 nm has no plasma-associated spectral inferences, the laser wavelength must be accurately determined and locked when the system is employed to analyze the sample solutions that contain both Hg and other elements.

4.6 Conclusion

We introduce a new technique, namely, a stepwise electron impact excitation-cavity ringdown absorption spectrometry (SEIE-CRAS) to detect Hg at 405 nm. The technique can also be universally applied to study other analytes, including elements and isotopes, whose transitions originate from either a metastable state or an optically excited state. The atomic absorption spectra of Hg at 405 nm using SEIE-CRAS are reported and the measurement is achieved through the electron impact excitation of Hg to the metastable state and the cavity ringdown absorption of the 405 nm transition. The results indicate that the new approach is scientifically feasible and that the development of a *portable* mercury ringdown spectrometer using a compact laser source is technologically conceivable. One caution should be taken when the 405 nm line is utilized to detect Hg: the detection sensitivity at 405 nm is approximately 250-fold lower than the one using the 254 nm line if the same plasma-ringdown system (the same laser beam path-length and ringdown mirror reflectivity) is used. The detection sensitivity of 50 $\mu g\ ml^{-1}$ in aqueous solutions or 1.2 ppmv in gas samples of Hg is achieved in the current experimental system using the 405 nm line with the mirror reflectivity of 99.91% and the laser beam path-length of 5 mm. Using an optimized system with a mirror reflectivity of 99.99%, the laser beam path-length of 10 cm, and the ringdown baseline noise of 0.3%, the estimated detection sensitivity of Hg using the SEIE-CRAS technique at 405 nm is 50 $ng\ ml^{-1}$ in aqueous solutions or 1.2 ppbv in gas samples. The development of a *portable* Hg

ringdown spectrometer based on the SEIE-CRAS technique using the palm-size 405 nm diode laser toward the theoretical detection sensitivity is underway.

4.7 Acknowledgements

This work is supported by the National Science Foundation grant CBET-1066486 and the US Department of Energy grant DEFC01006.

4.8 References

1. G. P. Miller and C. B. Winstead, J. Anal. At. Spectrom., 1997, 12, 907.

2. C. Wang, J. Anal. At. Spectrom., 2007, 22, 1347.

3. K. W. Busch and M. A. Busch, ACS Symposium Series 720, Cavity-Ringdown Spectroscopy: An Ultratrace-Absorption Measurement Technique, Oxford University Press, 1999.

4. G. Berden, R. Peeters and G. Meijer, Int. Rev. Phy. Chem., 2000, 19, 565.

5. M. D. Wheeler, S. M. Newman, M. N. R. Ashfold and A. J. Orr-Ewing, J. Chem. Soc. Faraday Trans., 1998, 94, 337.

6. G. Berden and R. Engeln, Cavity Ring-Down Spectroscopy: Techniques and Application, Wiley Publication, West Sussex, PO 19 8SQ, United Kingdom, 2009.

7. C. B. Winstead, F. J. Mazzotti, J. Mierzwa and G. P. Miller, Anal. Commun., 1999, 36, 277.

8. S. Q. Tao, F. J. Mazzotti, C. B. Winstead and G. P. Miller, Analyst, 2000, 125, 1021.

9. P. Yalin, V. Surla, M. Butweiller and J. D. Williams, Appl. Opt., 2005, 44, 6496.

10. C. Wang, F. J. Mazzotti, G. P. Miller and C. B. Winstead, Appl. Spectrosc., 2002, 56, 386.

11. C. Wang, F. J. Mazzotti, G. P. Miller and C. B. Winstead, Appl. Spectrosc., 2003, 57, 1167.

12. Y. Duan, C. Wang and C. B. Winstead, Anal. Chem., 2003, 75, 2105.

13. C. Wang, S. P. Koirala, S. T. Scherrer, Y. Duan and C. B. Winstead, Rev. Sci. Instrum., 2004, 75, 1305.

14. Y. Duan, C. Wang, S. T. Scherrer and C. B. Winstead, Anal. Chem., 2005, 77, 4883.

15. C. Wang, S. T. Scherrer, Y. Duan and C. B. Winstead, J. Anal. At. Spectrom., 2005, 20, 638.

16. Y. Duan, S. T. Scherrer, S. P. Koirala, C. Wang and C. B. Winstead, Anal. Chim. Acta, 2005, 532, 47.

17. P. Sahay, S. T. Scherrer and C. Wang, Development of Ultra-Sensitive, Real-time Field-Deployable Mercury, Beryllium, and other Contaminants Plasma Ringdown Spectrometer, 2011 Waste Management Conference, Phoenix, AZ, Feb. 27 – March 3, 2011.

18. B. Welz and M. Schuber-Jacobs , Fresenius' Z., Anal.Chem., 1988, 33, 324.

19. R. Brown, D. J. Gray and D. Tye, Water Air Soil Pollut., 1995, 80, 1237.

20. U. Platt, D. Perner, A. M. Winer, G. W. Harris and J. N. Pitts, Nature, 1980, 285, 312.

21. W. Wang, R. H. Hammond, M. M. Feijer, C. H. Ahn, M. R. Beasley, M. N. Levenson and M. L. Bortz, Appl. Phys. Lett., 1995, 67, 1375.

22. R. T. Jongma, M. G. H. Boogaarts, I. Holleman and G. Meijer, Rev. Sci. Instrum., 1995, 66, 2821.

23. Note: personal communications with Toptica and Continuum; a frequency doubled 254 nm laser source costs more than $100 K.

24. NIST Atomic Spectra Database, http://physics.nist.gov/cgi-bin/ASD/lines1.pl

25. K. Becker and C. C. Lin, in Elementary Collision Process in Plasmas, a chapter in Low Temperature Plasmas: Fundamentals, Technologies, and Techniques, Eds. R. Hippler, H. Kersten, M. Schmidt and K. H. Schoenbach, WILEY-VCH Verlag GmbH & Co KGaA, Weinheim, Germany, 2008, 1, 47.

26. R. Uhl, O. Wolff, J. Franzke and U. Haas, Fresenius J. Chem., 2000, 366, 156.

27. H. Horiguchi and S. Tsuchiya, Bulletin of the Chem. Soc. of Japan, 1977, 50, 1661.

28. G. F. Hanne, V. Nickich and M, Sohn, J. Phys. B: At. Mol. Phys. 1985, 18, 2037.

29. T. Stacewicz, E. Bulska and A. Ruszczyńska, Spectrochim. Acta B, 2010, 65, 306.

30. C. Wang, P. Sahay and S. T. Scherrer, Phys. Lett. A, 2011, 375, 2366.

31. J. B. Boffard, G. A. Piech, M. F. Gehrke, L. W. Anderson and C. C. Lin, Phys. Rev. A,1999, 59, 2749.

32. G. F. Hanne, V. Nickich and M. Sohn, J. Phys. B: At. Mol. Phys., 1985, 18, 2037.

33. J. N. Bass, R. A. Berg and A. E. S. Green, J. Phys. B: At. Mol. Phys., 1974, 7, 1853.

34. M. H. Phillips, L. W. Anderson and C. C. Lin, Phys. Rev. A, 1981, 23, 2751.

35. M. Schmidt and H. Conrads, in Plasma Sources, a chapter in Low Temperature Plasmas: Fundamentals, Technologies, and Techniques, Eds. R. Hippler, H. Kersten, M. Schmidt and K. H. Schoenbach, WILEY-VCH Verlag GmbH & Co KGaA, Weinheim, Germany, 2008, 1, 363.

36. C. Wang, N. Srivastava, S. T. Scherrer, P.-R. Jang, T. S. Dibble and Y. Duan, Plasma Sources Sci. Technol., 2009, 18, 0250301.

37. M. T. Herd, J. E. Lawler and K. L. Menningen, J. Phys. D: Appl. Phys., 2005, 38, 3304.

38. K. L. Menningen and J. E. Lawler, J. Appl. Phys., 2000, 88, 3190.

39. A. E. Siegman, Laser, University Science Books, Mill Valley, CA, 1986.

40. G. F. Kirkbright and M. Sargent, Atomic Absorbance and Fluorescence Spectrometry, Academic Press, London, 1974.

41. A. A. Radzig and B. M. Smirnov, Reference Data on Atoms, Molecules, and Ions, Springer-Verlag, New York, 1985.

42. X. Faïn, H. Moosmüller and D. Obrist, Atmos. Chem. Phys., 2010, 10, 2879.

43. S. Spuler, M. Linne, A. Sappey and S. Snyder, Appl. Opt., 2000, 39, 2480.

44. C. C. Carter and G. P. Miller, Sensor Research and Development Corporation, A Cavity Ring-Down Spectroscopy Mercury Continuous Emission Monitor, Orono, Maine, 2004, 04473.

45. Y. Duan, C. Huang and Q. S. Yu, Rev. Sci. Instrum., 2007, 78, 015104.

46. J. Luque, LIFBASE (version 2.0).

CHAPTER V

A PORTABLE OES-CRDS DUAL-MODE PLASMA SPECTROMETER FOR MEASUREMENTS OF ENVIRONMENTALLY IMPORTANT TRACE HEAVY METALS: INITIAL TEST WITH ELEMENTAL HG*

5.1 Abstract

A portable optical emission spectroscopy-cavity ringdown spectroscopy (OES-CRDS) dual-mode plasma spectrometer is described. A compact, low-power, atmospheric argon microwave plasma torch (MPT) is utilized as the emission source when the spectrometer is operating in the OES mode. The same MPT serves as the atomization source for ringdown measurements in the CRDS mode. Initial demonstration of the instrument is carried out by observing OES of multiple elements including mercury (Hg) in the OES mode and by measuring absolute concentrations of Hg in the metastable state 6s6p $^3P_0$ in the CRDS mode, in which a palm-size diode laser operating at a single wavelength 405 nm is incorporated in the spectrometer as the light source. In the OES mode, the detection limit for Hg is determined to be 44 parts per billion (ppb). A strong radiation trapping effect on emission measurements of Hg at 254 nm is observed -

---

Note: The major contents of this chapter have been adapted from Review of Scientific Instruments, **83**, 095109 1-14, (2012). Copyright (2012), with permission from American Institute of Physics.

when the Hg solution concentration is higher than 50 parts per million (ppm). The radiation trapping effect suggests that two different transition lines of Hg at 253.65 nm and 365.01 nm be selected for emission measurements in lower (< 50 ppm) and higher concentration ranges (> 50 ppm), respectively. In the CRDS mode, the detection limit of Hg in the metastable state 6s6p $^3P_0$ is 2.24 parts per trillion (ppt) when the plasma is operating at 150 W with a sample gas flow rate of 480 mL min^{-1}; the detection limit corresponds to 50 ppm in Hg sample solution. The advantages of this novel spectrometer are two-fold: it has a large measurement dynamic range, from a few ppt to hundreds ppm and the CRDS mode can serve as calibration for the OES mode as well as providing high sensitivity measurements. Measurements of seven other elements, As, Cd, Mn, Ni, P, Pb, and Sr, using the OES mode are also carried out with detection limits of 1100, 33, 30, 144, 576, 94, and 2 ppb, respectively. A matrix on Hg measurement effect in the presence of other elements has been found to increase the detection limit to 131 ppb. These elements in lower concentrations can also be measured in the CRDS mode when a compact laser source is available to be integrated into the spectrometer in the future. This exploratory study demonstrates a new instrument platform using an OES-CRDS dual-mode technique for potential field applications.

5.2 Introduction

Real-time, *in situ* detection and quantification of environmentally toxic trace heavy metals have long been a matter of paramount importance. In the last few decades, a number of significant strides have been made toward the detection of hazardous elements based on various techniques, such as atomic absorption spectroscopy (AAS), optical emission spectrometry (OES), X-ray fluorescence, laser-induced fluorescence, mass

spectrometry, etc, [1-8]. Still, the whole process of contaminant detection and quantification chiefly relies on lab-based instruments: for example, gas chromatography-mass spectrometry (GC-MS), inductively coupled plasma-optical emission spectroscopy (ICP-OES), or ICP-MS techniques. As a routine procedure, samples are collected from sites, processed, and then sent to labs elsewhere for evaluation and testing. The entire process becomes both time-consuming and expensive. Although these lab-based instruments, viz. GC-MS, ICP-OES/MS, etc., are highly sensitive and capable of multi-element detection, the instrument systems are too bulky to be employed cost-effectively in the field study, manifesting the technological limitations of these instruments for real-time *in situ* monitoring of multiple elements.

In an attempt to address this issue, we are developing a portable microwave induced plasma (MIP) based OES and cavity ringdown spectroscopy (OES-CRDS) dual-mode spectrometer for real-time detection and quantification of environmentally toxic trace metals. A prototype instrument has been constructed; the design, operation, and the results obtained with the instrument have been reported in this work. The spectrometer can run in two modes: OES and CRDS. The OES mode is capable of measuring multi-element simultaneously, and the CRDS mode, being calibration free, measures the absolute concentrations, which can calibrate measurements in the OES mode. The choice of combining the MIP and CRDS techniques to construct this portable spectrometer is based on their respective advantages and current technology maturity levels.

OES has been one of the most convenient techniques for real-time monitoring of trace elements [9] and can also quantify species concentration when the system is calibrated. A microwave induced plasma, due to its compact size, low power

consumption, low gas flow rate, freedom from need for external cooling, and high excitation efficiency, has long been a subject of study in development of a field-deployable plasma emission source. The MIP-based OES has demonstrated its potential to be developed as a real-time continuous monitor [10]. Significant strides have been made for the MIP-OES in terms of plasma stability, size, power, and gas flow rate during the last decade. Detections of various environmentally important elements [11, 12], including Hg, Be [13], U [14], have been demonstrated by using a robust microwave plasma torch (MPT). A series of attempts at field monitoring using an MIP-OES system have been successfully demonstrated for trace metal emissions [15, 16] and air particulate monitoring [17]. The development of the MPT technology with time, its advantages over conventional MIP sources, and its application in OES, etc., can been seen in several previous reports [18-28]. The present status of MIP based analytical spectrometry, in terms of plasma source, instrumentation, analytical performance and applications, etc. have been discussed in detail in a recently published book [29]. Very recently, a fully computer controlled MPT-based OES system is being developed for multi-element analysis [30].

Recently, the incorporation of an MPT into a CRDS system (so called plasma-CRDS technique) has been demonstrated for the detection of elements and isotopes [31-35]. In this technique, the MPT is used as an atomization source and CRDS serves as a detector. To date, measurements of environmentally important elements, such as Pb, Sr, Mn, Hg, Hg isotopes, U isotopes, etc., in concentrations ranging from parts per million (ppm) to parts per trillion (ppt) levels using the plasma-CRDS technique have been reported [13, 32, 36-41]. However, except for one early study to demonstrate the

potential to develop a portable instrument using the plasma-CRDS technique, in which an external cavity diode laser operating at 679 nm was employed to measure Sr atomized in a low power ICP [42], no study has reported further progress in terms of instrumentation using plasma-CRDS. One major reason behind this fact is that there are two development hurdles: requirements of a compact, automated plasma source that can be electronically operated and a compact laser source that can be integrated into the plasma-CRDS instrument system. To date, a compact MPT can be manufactured into a system, which can be operated by a computer-based control for plasma power, gas flow rate, and auto-ignition of the plasma. Concurrently in the last few years wavelength of diode lasers has been extended to short-blue region and several transition lines of environmentally important elements can be detected using such compact diode lasers. The technology advancements in the two fields have motivated further exploration in plasma-CRDS instrumentation leading to a portable spectrometer for multi-element measurement in a large dynamic range for diverse field applications, even with capability of self-calibration.

In this work, we explore for the first time a combination of OES and CRDS in a single portable spectrometer. The objective of this work was to demonstrate operation of this new instrument and test its initial performance on measurements of Hg sample solutions. The instrument platform can be extended to measure other elements by using different laser sources. In this chapter, first, the instrument design, configuration, and its major parts are described (Section 5.3). Second, results and discussion are presented, in which measurements of Hg in the OES are reported (Section 5.4). In Section 5.5, operation and measurements in the CRDS mode of the instrument are described. The

Section 5.5 discusses the multi-element measurements using the OES mode. Finally, discussion of advantages and existing challenges in the dual-mode spectrometer is presented.

5.3 Instrument Design and Configuration

5.3.1 Instrument design

The central idea of the instrument design lies in that a single MPT is utilized as an emission source for the OES measurements (OES mode) and as an atomization source for CRDS measurements (CRDS mode); and these two operation modes are integrated into a single instrument platform. The automated operation of the MPT and the instrument packaging including the instrument frame, electronic control, MPT ignition, and OES data collection software, which were made by Elemetric Instrument LLC [30]. The system was purchased by our Laser Spectroscopy and Plasma Laboratory and then modified by incorporating an external sampling part and microwave plasma power generator, so that the system can be operated for OES measurements. Our further modification of the system includes addition of a CRDS portion by integrating a ringdown cavity and a compact laser source, and a ringdown control portion into the instrument platform to form a dual-mode OES-CRDS spectrometer. Figure 5.1(a) shows the OES-CRDS dual-mode spectrometer instrumentation layout. The spectrometer excluding the external sampling and the ringdown data acquisition portions has dimensions of 60 cm × 43 cm × 27 cm. The major instrument components are an MPT, plasma power generator, OES system, CRDS system, electronic control portions for OES and CRDS, and a sampling introduction portion. The following sections first describe the placements, operations, and functions of each of the major instrument components in

terms of the OES and CRDS modes, followed by description of technical aspects of co-arrangements of the two operating modes.

5.3.2 Optical Emission Spectroscopy Mode

The OES system contains several main parts: a microwave plasma power generator, MPT, nebulizer/gas flow unit, and a compact spectrometer (197 - 419 nm, resolution 0.12 nm). The MPT, as an atomization source, was housed inside a cylindrical cage. An external 2.45 GHz microwave plasma power generator (Saeram Inc.) delivered microwave power to the MPT. Plasma emissions were collected using a system of plano-convex lenses before feeding onto the detector head, which was connected to a pocket size spectrometer (Ocean Optics) via a section of optical fiber.

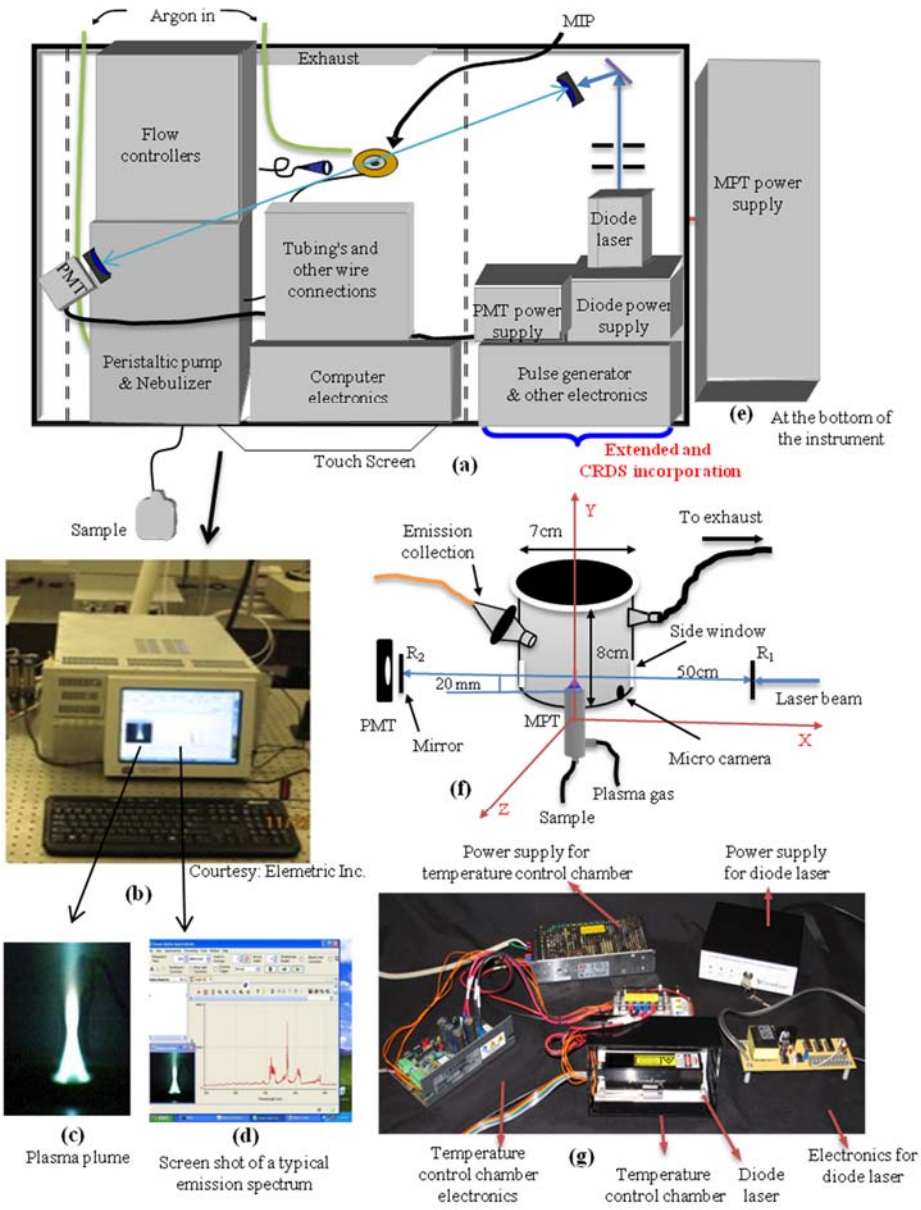

Figure 5.1 The instrumentation layout, schematic, design, and major components of the dual-mode spectrometer

The collected emission data were analyzed with the built-in software (Ocean Optics, Spectra Suite) on a laptop computer (Fig. 5.1(b)). The instrument when connected to the power generator and the plasma sampling portion was fully computer-controlled

through a touch screen built in the front panel of the instrument. The exhausts and the necessary slots for gas and the sample introductions were located in the rear panel. The instrument frame along with the power supply (50 cm × 48 cm × 13 cm) can be put on a cart and be readily moved from one place to another. The instrument frame has reserved enough space inside to house a built-in nebulizer and a compact plasma power generator, both of which are being developed. In this experiment, instead, we used an external ultrasonic nebulizer and an external power generator to test the spectrometer.

The microwave generator had a maximum output power of 200 W. The power generator was connected to the MPT via a 50-Ω coaxial cable. The MPT used in the present work was similar to the one discussed in previous reports [41, 43]. Plasma was supported by argon gas (99.99% purity, Airgas). The sample injection was made through the inner tube of the MPT, which was connected to the nebulizer by a thin tubing (Nalgene). A peristaltic pump (Miniplus 3, Gilson) was used to deliver a liquid sample into an ultrasonic nebulizer (U-5000 AT^{+}, CETAC Technologies), which converted aqueous samples into aerosol. The aerosol was carried away by argon gas to the MPT. The calibrated conversion efficiency of the aqueous samples to gas samples was 12-15% [42]. A membrane tubing (Perma Pure) wrapped with a heat tape connected to a desolvator (a box filled with moisture absorbing granules) was used to get rid of the excess moisture in the sample aerosol. A set of three-channel flow meters (Cole-Palmer) was used to control and regulate the gas flows to the MPT. The gas flow rates in the two plasma torch channels were adjustable through the touch screen. The ignition of plasma was initiated electronically via the touch screen.

Emissions generated by the plasma were collected using a telescope system consisting of two plano-convex lenses and then focused to the end of a 30-cm long fiber connected to an emission spectrometer that was interfaced with a charge coupled device (CCD) detector. A micro-camera was attached inside the cylindrical cage to display a live image of plasma plume on the touch screen. A typical image of the plasma is shown in Fig. 5.1(c). Variations in shape, color, and stability of the plasma were clearly monitored through the live image. Operating parameters, such as the plasma gas flow rate, sample gas flow rate, plasma power, etc. are listed in Table 5.1.

Table 5.1 Experimental parameters.

Instrument	Working parameters	Unit
Microwave power (forward)	150	W
Reflected power	7-10	W
Plasma gas flow	400-500	mL min^{-1}
Carrier gas flow	400-550	mL min^{-1}
Ar gas flow for membrane drier	0.5	L min^{-1}
Sample uptake	0.75	mL min^{-1}
Nebulizer heating temp	140	°C
Nebulizer cooling temp	-6	°C
Membrane desolvator temperature	60	°C
Emission spectral range	200-415	nm
Integration time	150	ms
Signal average	20	counts
Cavity length	50	cm
Absorption path length	2-4	mm
Mirror reflectivity	99.96	%
Baseline noise $(\frac{\sigma}{\bar{\tau}})$	Without Plasma: 0.30	%
	With Plasma: 0.50	%
Co-arrangements of OES and CRDS optical systems		
Emission collection location	Converging point of the plasma	20 mm above the torch orifice
Heat dissipation of plasma	Exhaust fan	DC-12 V, 0.9 Ampere
Side slit (window) width	7 mm × 4 mm	----
Laser position in the plasma	Just below the converging point	17-20 mm above the torch orifice
Spatial precision	± 0.5 mm	-----
Laser pulse frequency	10 Hz	-----

With the plasma switched on, the wall of the closed cylindrical housing becomes hot in a short while because of the plasma emissions. In the present system, the hot air inside the housing was drawn out with the help of an exhaust fan (DC-12 V, 0.9 amp)

through a metallic tube connected to the upper part of the housing (Fig. 5.1(f)). The speed of the exhaust fan must be optimized in order to minimize the turbulence in the plasma and to maintain plasma plume stability.

The stability of the plasma was examined prior to OES measurements. With the operating parameters listed in Table 5.1, a stable plasma was obtained at an operating plasma power ranging from 100 W to 200 W and an argon gas flow rate in between 400 mL min^{-1} and 500 mL min^{-1}. At comparatively lower powers (< 100 W), the plasma became slightly jittery. The shape and stability of the plasma can be optimized by adjusting the gas flow rates using the controller in the front panel. After a series of optimization procedures, the most stable emission signal was achieved when the plasma operated at 150 ± 25 W and a gas flow rate of 450 ± 25 mL min^{-1}. In the subsequent experiments, the plasma power was set at 150 W. When an analyte sample was introduced into the MPT, the gas flow rate was further adjusted to be in the range of 450 to 525 mL min^{-1}, depending on each of the individual sample solutions.

5.3.3 CRDS Mode

A schematic of the CRDS system assembled in the spectrometer is shown in Fig. 5.1(f). A ringdown cavity of 50-cm length was created using two plano-concave mirrors with a reflectivity 99.96% for wavelength of 404.65 nm. The MPT was located at the center between the two mirrors. A palm-size diode laser (CrystaLaser) operating at the single wavelength of 404.65 nm was used to excite the cavity.

The laser head was housed in an in-house thermal controlled chamber with a thermal stability of ± 0.2°C. The diode laser was triggered externally to generate laser pulses at 10 Hz. The pulse generator and the power supply of the diode laser were home

built and miniaturized to fit in the available space in the spectrometer. The photo-multiplier tube (PMT) was powered by an in-house compact power supply.

The layout of the ringdown cavity shown in Fig. 5.1 was configured such that the cavity length was maximized in the constrained space of the spectrometer and locations of the two mirror mounts allowed for fine adjustments using a long driver screw outside the instrument case when the system was completely covered. Two small (7 mm × 4 mm) side windows, diametrically opposite to each other, were created in the wall of the MPT chamber that housed the MPT, so that the laser beam could pass through the plasma plume. The measuring principle of the plasma-CRDS technique is based on [36, 41] and as discussed in chapters above

$$\tau = \frac{d}{c(1 - R + \beta_{plasma} l_s + \beta_{air}(d - l_s) + absorbance\ )} \tag{5.1}$$

where d is the cavity length, R is the mirror reflectivity, β_{plasma} and β_{air} represents the broadband scattering coefficients in the plasma and open air cavity, respectively; c and l_s are the speed of light and the laser beam pathlength through the plasma, respectively. In general, the scattering coefficients, β, vary slowly over the bandwidth of the cavity mirrors; losses occurring because of it can be incorporated into an effective reflectivity R_{eff}. The equation for ringdown time can then be expressed as

$$\tau = \frac{d}{c(1 - R_{eff} + absorbance\ \ )} \tag{5.2}$$

where the absorbance is determined in Equation (5.3) using two measured ringdown times,

$$A = \frac{d}{c}\left[\frac{1}{\tau} - \frac{1}{\tau_0}\right] \tag{5.3}$$

where τ and τ_0 are ringdown times with and without samples inside the cavity.

The absolute number density is determined by

$$n = \frac{A}{\sigma l_s} \tag{5.4}$$

where the absorption cross section $\sigma(\nu)$ at a particular transition frequency is known for some elements; unknown cross sections of other elements can be calculated [41, 44]. Under atmospheric plasma conditions, mechanisms for linewidth broadening are complicated. In such a scenario, the lineshape of the absorption line is a Voigt profile and the absorption cross section is be represented as [45, 46]

$$\sigma_{ij}(\nu) = \frac{g_j}{g_i}\frac{\lambda^4}{4\pi^2 c}\frac{A_{ji}}{\Delta\lambda_D}V(a,0)\sqrt{(\pi \ln 2)} \tag{5.5}$$

where g_j and g_i are the degeneracies of the upper and lower energy levels j and i, respectively, λ is the transition wavelength, and c is the speed of light. A_{ji} represents the spontaneous emission transition rate (also known as Einstein A coefficient). For most atomic/ionic transitions, these parameters are well documented in the literature. $\Delta\lambda_D$ is the Gaussian component of the broadened linewidth due to Doppler broadening. $V(a,0)$ is the Voigt function which is determined by the linewidth broadening mechanism. The parameter a is calculated using the ratio of Lorentzian and Gaussian components [32, 47]. In practice, the measured lineshape is typically a spatially-averaged and integrated lineshape along the particular line-of-sight; therefore, an averaged value of the cross

section is obtained. In the CRDS measurements of Hg at 405 nm in this work, the calculated absorption cross section, 4.5×10^{-13} cm^2 $atom^{-1}$, was used [44].

5.3.4 Co-arrangements of the OES and CRDS Optical Systems

Figure 5.1(f) shows the co-arrangements of the OES and the CRDS optical systems. With the plasma switched ON, OES and CRDS measurements were conducted simultaneously via two different computers. Plasma emissions were collected using a lens system focused at the converging point of the plasma column. The converging point was 20 mm above the torch orifice in this case. The choice of the converging point of the plasma for collecting emissions from an MIP-based excitation source has been discussed previously [43]. The converging point of MIP has the strongest emissions. At the same time, the collected signals from this point are more stable as compared to the signals collected from other points in the plasma. These two characteristics are important requirements for better detection sensitivity of the instrument.

The laser beam was coupled into the ringdown cavity through the two side-windows in the cylindrical cage and was aligned to pass through the plasma right beneath the converging point of the plasma column. Theoretically, the laser beam passing exactly through the converging point of the plasma has the largest probability of interacting with the plasma gas than at any other location in the plasma [43]. Under high temporal resolution [43], it can be seen clearly that the plasma plume consists of time-integrated filaments that converge at the converging point. Therefore, the laser beam has the highest possibility of interacting with plasma gas at this point. This arrangement is particularly important when the laser repetition rate is not high, i.e., 10 Hz, in the present work. The position of laser beam inside the plasma can be precisely controlled by adjusting the

plasma torch horizontally and vertically with a spatial precision of ± 0.5 mm. As illustrated in the Fig. 5.1(f), the laser beam lies in the horizontal X-Z plane oriented 90° to the plasma torch axis. In order to keep the size of the instrument compact, several parts of the instrument were miniaturized and their pictures are shown in Fig. 5.1(g).

The size of the side-windows through which the laser beam passed through the plasma chamber was critical to both the plasma stability and the ringdown stability. Once the ringdown system was aligned, the openness of the side windows was minimized by sealing other open portions to prevent plasma exhausts from leaking inside the instrument. With average over 100 ringdown events, the ringdown baseline stabilities were 0.3% and 0.5%, respectively, when the plasma was OFF and ON. The ringdown signals were observed on the oscilloscope and the ringdown time was displayed on a separate computer, simultaneously along with the OES measurements being conducted on the instrument computer (Fig. 5.1(b)). It must be noted that the ringdown measurements can also be controlled by the built-in computer of the instrument without interfering with the OES measurements when the ringdown software is installed in the built-in computer. This integration was not achieved in this exploratory study.

5.3.5 Protocol for CRDS Calibration Process

One of the merits of the instrument is self calibration. The system does not require an external calibration for measurements. The capability of the CRDS technique can be utilized to calibrate OES measurements to obtain the absolute number density. The protocol of the CRDS calibration is described below.

A set of samples of different unknown concentrations in a wide dynamic range will be used for simultaneous CRDS and OES measurements. For each sample, absolute

concentration of an element in gaseous phase present in the plasma is determined by CRDS using Eq. 5.4 With the known conversion efficiency of the nebulizer system, the element's concentration in the aqueous sample is obtained. At the same time, with the OES mode, the emission intensity of one or a set of selected transition lines of the element is recorded for the same sample. Repeating the measurements for each of the other samples of the element, we can obtain a calibration curve of the absolute density of the element vs. line intensity of the selected transition line of the element. Once a calibration is established, we can use the OES mode of the spectrometer to obtain absolute number density of the element. The absolute number density measurements using CRDS can be further validated by using a set of samples with known concentrations. At given experimental conditions, a set of validation data of the measured number densities of the element in the plasma vs. sample concentrations in aqueous samples can be obtained. This validation is often defined as calibration of the conversion efficiency of the sampling using a nebulizer [42].

5.4 Results and Discussion

5.4.1 Measurements of Hg in OES Mode

A stable plasma was sustained at 150 W with an argon gas flow rate of 450 mL min^{-1}. The height of the plasma (the bright part above the torch orifice) was around 30 mm. The emission collecting lens was focused at the converging point, which was 20 mm above the plasma torch orifice [43]. With pure plasma, the prominent emission bands of N_2, OH, N_2^+, and NO were observed as shown in Figure 5.2(a). The transitions from the OH (A-X) (0-0) band were utilized to estimate the plasma gas temperature (T_g) with the help of LIFBASE software [48]. Subsequently, the plasma gas temperatures were

estimated for the emissions obtained at different microwave powers. At 75 and 200 W, T_g were determined to be 2550 K and 3100 K, respectively, with a measurement uncertainty of ± 100 K. Figure 5.2(b) shows the variations of T_g estimated at different microwave plasma powers.

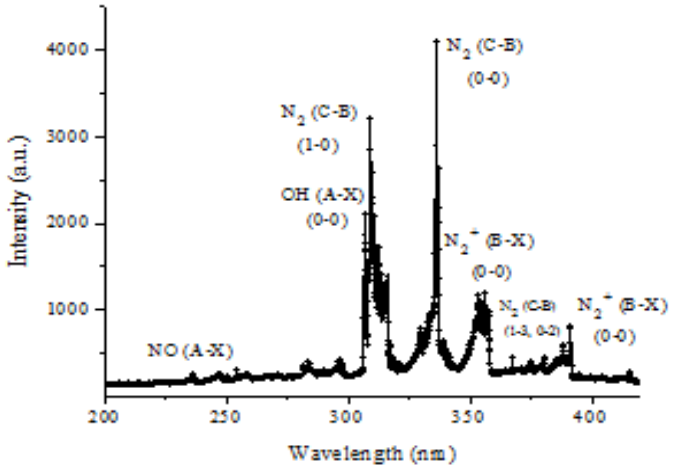

(a)

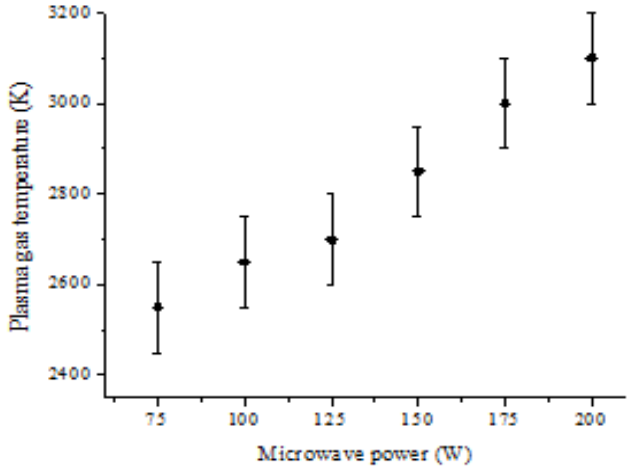

(b)

Figure 5.2 (a) Emission spectra of argon plasma at 150 W power and gas flow 450 mL min^{-1}. (b) Variation of plasma gas temperature with plasma power

Mercury sample solutions in the concentrations ranging from 500 ppb to 400 ppm were injected into the plasma through the sampling system. Emission spectra were recorded at each of the five different powers: 100, 125, 150, 175, and 200 W. A number

of transition lines corresponding to Hg(I) in the wavelength range of 200 to 410 nm were observed. Emission peaks were assigned based on the NIST atomic line database [49]. No transition line corresponding to ionic mercury Hg(II) was observed in this study.

The most prominent emission recorded for Hg was the 253.652 nm line, followed by 365.015 nm, 313.184 nm and others. Table 5.2 lists the prominent Hg emission lines obtained in this work in comparison to the ones documented in the NIST database.

Table 5.2 Comparison of emission intensities of Hg transition lines obtained in this work with those listed in the NIST atomic database.

Hg state	Wavelength (nm)	E_i (cm^{-1}) - E_k (cm^{-1})	Intensities in NIST		Intensity in this work	
			Ab. Int.	Rel. I (%)	Ab. Int.	Rel. I (%)
I	253.652	0 – 39412.237	900000	1	2862	1
I	296.728	37644.982 – 71336.005	3000	0.33	43	1.50
I	313.184	39412.237 – 71333.053	4000	0.44	89	3.10
I	365.015	44042.909 – 71431.180	9000	1.00	130	4.54
I	404.656	37644.982 – 62350.325	12000	1.33	28	0.97

The relative intensities (in percentage) listed in the fifth and seventh columns of the table were determined by the ratios of the emission intensities of Hg lines listed in the fourth and sixth columns to the intensity of the strongest line of Hg, i.e., 253.652 nm. It can be seen in the table that the second strongest transition according to the NIST database is the 404.656 nm ($5d^{10}6s7s \rightarrow 5d^{10}6s6p$) line, whereas in our experiment the second strongest transition is the 365.015 nm ($5d^{10}6s6d \rightarrow 5d^{10}6s6p$) line. Most of the emission lines observed in this experiment have higher relative intensity than those reported in NIST database. In the present low-power and low temperature plasma, the

electron density is on the orders of 10^{12} - 10^{15} electron cm^{-3} and the excitation temperature has a magnitude of 6000 – 9000 K [29, 43, 50-51], as compared to the much higher electron density and excitation temperature, e.g., 10^{15} - 10^{16} electron cm^{-3} and 10000 K and higher, respectively, in high power plasmas, such as ICP, high power arc, etc., which operates at a power of few kilowatts [51, 52]. In these high power discharges, atoms are readily excited to higher energy states, which consequently result in more ionic lines originating from higher energy levels. The stronger relative emission intensity in this low power MPT indicated that the use of the low power MPT as an atomization source provides an advantage over other high power plasma sources for OES measurements.

5.4.2 Effect of Microwave Power on Emission Spectra and Plasma Plume

The influence of plasma power on the emission spectra was investigated. Emission spectra of Hg were recorded at five different powers: 100, 125, 150, 175, and 200 W. The change in the power had no affect on the number of transition lines, i.e., increasing or decreasing the power from 100 W to 200 W, or vice-versa, did not generate any new emission line in the spectrum. The change in power, however, did affect the signal intensity (peak amplitude) of the transition lines. The peak amplitudes of the transition lines at 200 W were higher than the peak amplitudes at 100 W. The most significant influence of the power was on the shape and stability of the plasma plume. At lower power, the plasma was jittery, while at higher power, the plasma had a burning flame engulfing it. In both these cases, the emission intensities were highly fluctuating, imparting high noise to the signal. Since the signal to noise ratio is a crucial entity in OES based detection techniques, which can severely affect the limit of detection of elements,

and hence is an important feature of an instrument; we, therefore, also looked into the effects of power on the detection limit of Hg with this spectrometer in the Hg sample solution concentration range of 500 ppb - 400 ppm. To determine the detection limit (DL) for Hg, a calibration curve, intensity vs Hg concentrations, at 253.65 nm was obtained. The value of 3σ (three times the standard deviation) was substituted in the linear equation of the calibration curve to obtain the minimum detectable Hg concentration. The DLs obtained at different plasma powers are shown in Fig. 5.3.

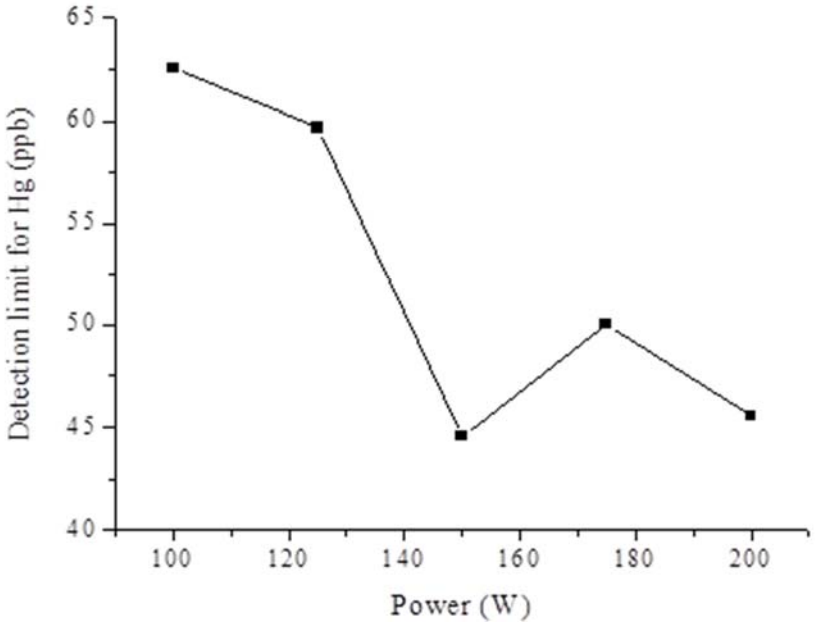

Figure 5.3 Variation in the detection limit of Hg, obtained at 253.65 nm, as a function of microwave power

The DLs obtained at different plasma powers were found to decrease with the increase in power. However, the lowest DL for Hg, 44 ppb, was obtained at 150 W microwave power. The reason for the lowest DL at 150 W can be attributed to the

combined effect of the best plasma shape and the stable plasma plume, hence, a higher signal to noise ratio at that power.

5.4.3 Effect of Radiation Trapping of 253.65 nm Transition Line on Hg Concentration Measurement.

Figure 5.4 shows the radiation trapping (RT) effect of the 254 nm line (the same transition line at 253.65 nm) at different Hg concentrations. With increase in Hg concentration from 10 ppm to 50 ppm, the emission intensity of the 254 nm line increased, so did other transition lines of Hg, as shown in insets (1) – (3) in Fig. 5.4. However, at concentrations higher than 50 ppm, the intensity of the 254 nm line started decreasing due to the RT effect, whereas intensities of the other transition lines continued to increase, showing absence of apparent RT effect, as shown in insets (4) – (6) in Fig. 5.4. These phenomena were the same even when the Hg concentration was increased to 400 ppm. Figure 5.5 shows the relative emission intensity of the Hg 254 nm line versus Hg sample concentration. The experimental curve in Fig. 5.5 shows that the emission intensity is approximately linear to the Hg concentration in the low concentration range (< 50 ppm), while at concentrations higher than 50 ppm, the RT effect alters the response trend severely. The strong radiation trapping effect of the Hg 254 nm transition line suggests that OES measurements of Hg using 254 nm line cannot provide quantitative information with regard to Hg sample concentration when it is higher than 50 ppm. The RT effect of the 254 nm line was observed repeatedly in each set of emission spectra and was consistent at all plasma powers examined.

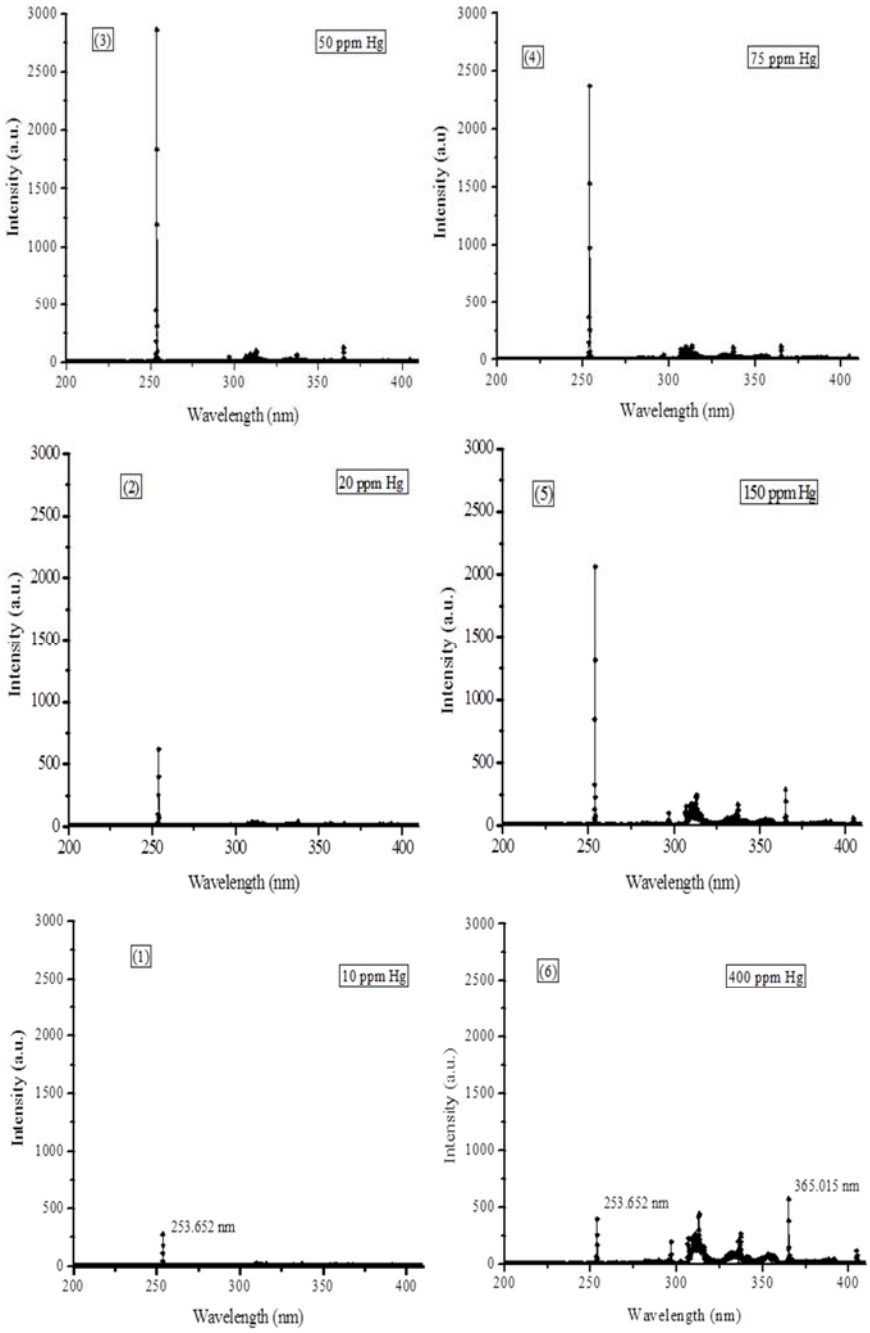

Figure 5.4 Emission spectra of Hg. (1) - (3) No RT effect at the concentrations lower than 50 ppm; (4) - (6) Apparent RT effect at concentrations higher than 50 ppm.

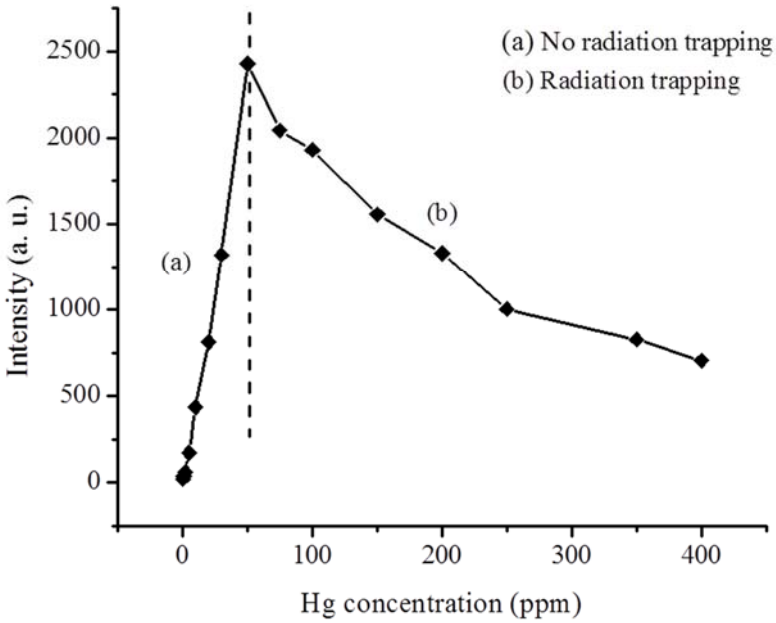

Figure 5.5 Variation of the emission intensity of the Hg 254 nm transition with Hg concentration.

The radiation trapping of the 254 nm Hg line was reported as early as 1959 as a part of theoretical modeling, followed by several experimental studies, which investigated the imprisonment of the Hg 254 nm emissions in various gaseous discharges [53-57]. However, only in a recent study, Hadidi *et al*. [58] reported the RT phenomena of the transition lines, 253.65 nm of the Hg ($6p\ ^3P_1 \rightarrow 6s^{21}S_0$) and 228.80 nm of the Cd ($5p\ ^1P_1 \rightarrow 5s^{21}S_0$), in the development of an on-line emission monitor using a similar microwave plasma. In that study, the plasma power was 1.5 kW, sample concentration was 10000 ppm, and the emission detector was located along the axial direction of the plasma torch. Interestingly in that study, no apparent RT effect was observed when the Hg emissions were collected in side view (perpendicular to the plasma axis). In the

present study, however, under the aforementioned experimental conditions, i.e., 150 W, 100 ppm Hg, the emissions were collected in perpendicular to the plasma axis and the RT effect was apparent when the Hg sample concentration was higher than 50 ppm, as shown in the figures 5.4.

Our observation supports that the RT effect of the Hg 254 nm transition line also exists in the perpendicular view of the plasma emissions, in addition to the axial view as reported previously [58]. This finding offers complimentary information on the RT of the Hg 254 nm line in the atmospheric microwave plasmas. The result provides a guideline for the instrument design, for example, which emission line of Hg should be selected for OES measurements and additional attention must be paid to the RT effect. Except for the strongest transition line at 253.65 nm, Hg has other strong transition lines at 296.72, 313.18, 365.01, and 404.65 nm observed in the present plasma. One of these lines can be selected for Hg OES measurements when Hg concentration is higher than 50 ppm so that the adverse effect of the RT is avoided.

The 365.01 nm line resulting from the $5d^{10}6s6d \rightarrow 5d^{10}6s6p$ transition was the second strongest emission line of Hg. No RT phenomenon was observed for this transition in the examined concentration range 50 - 400 ppm. Therefore, this line was selected to measure Hg at concentrations higher than 50 ppm and an experimental calibration curve was obtained. Figure 5.6(a) and 5.6(b) shows the calibration curves plotted at the wavelengths 253.65 and 365.01 nm, respectively. The calibration curve at 253.65 nm transition line, linearity $R^2 = 0.99$, Fig. 5.6(a), was carefully utilized for detections of Hg at concentrations lower than 50 ppm. As shown in Fig. 5.6(b), the calibration curve plotted at 365.01 nm transition line also shows good linearity ($R^2 =$

0.97) in the Hg sample concentration range of 50 - 400 ppm. As described previously, detection limit of the instrument for Hg using the 254 nm line was 44 ppb. These results suggest that two transition lines of Hg at 253.65 nm and 365.01 nm should be used for OES measurements of Hg at lower (< 50 ppm) and higher (> 50 ppm) concentrations, respectively. Combination of both Hg lines allows the spectrometer to be used for measurements of mercury in a large dynamic range, low ppm - hundreds ppm when operating in the OES mode.

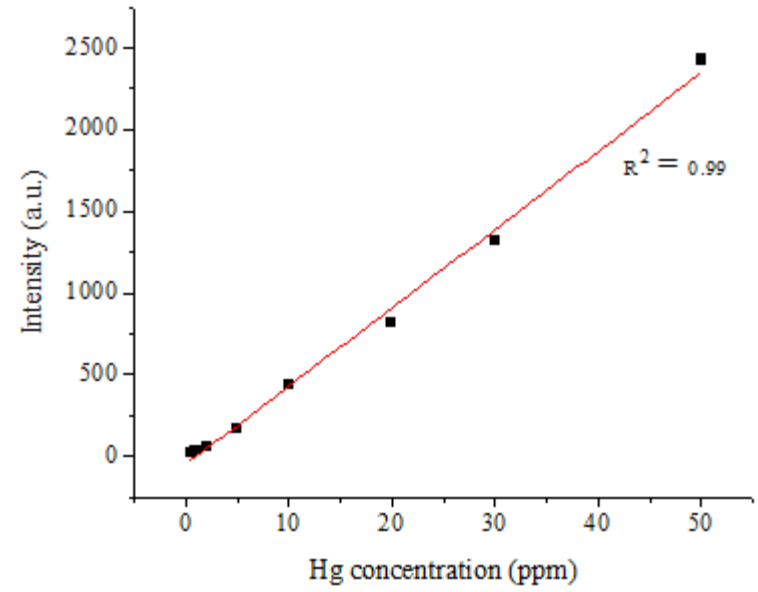

(a) 253.65 nm

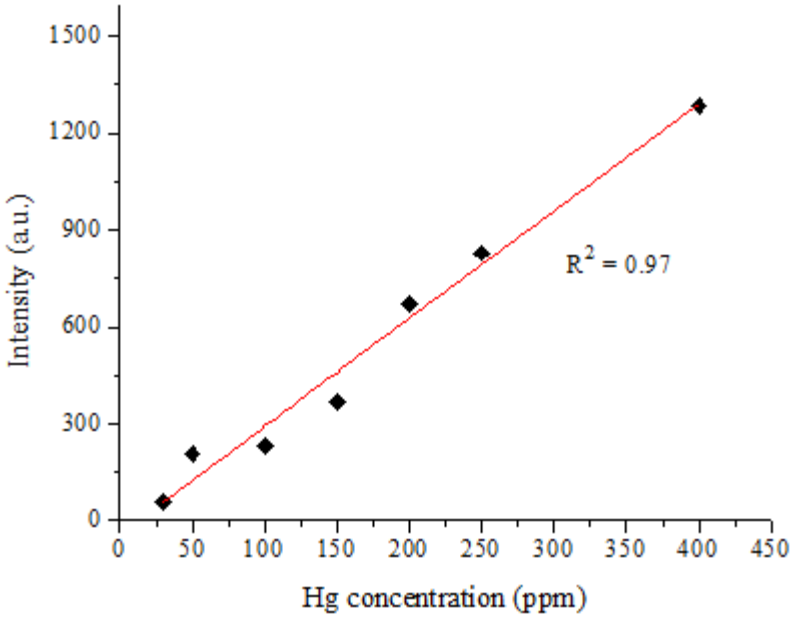

(b) 365.01 nm

Figure 5.6 Calibration curves using two transition lines of Hg.

5.5 CRDS Mode of the Spectrometer

Operation of the CRDS mode of the spectrometer is independent of the OES mode, except for sharing the same MPT source. In our previous study, we evaluated the technology capability of measuring Hg using the plasma-CRDS technique at 405 nm [44]. The Hg 405 nm absorption line belongs to the transition 6s6p $^3P_0 \rightarrow$ 6s7s $^3S_1$, originating from the upper metastable state. Hg distribution in the metastable state was populated through electron impact excitation [59]. In the development of the dual-mode spectrometer, we used the same approach of the electron impact excitation-CRDS to measure metastable state Hg at 405 nm to demonstrate the concept of the CRDS mode of the spectrometer. It should be noted that measurement of absolute Hg density in the 6s6p $^3P_0$ metastable state does not directly reflect the actual concentration of mercury in an aqueous sample and may not be of practical importance in environmental analysis in the present state; however the measured absolute number density in the metastable state can be correlated to the Hg concentration in the sample solution for given experimental conditions. Another practical reason to use the 405 nm line is that there is currently no such compact (palm-size) laser source that can be integrated into the present instrument platform for Hg measurements using other transitions such as the strong 254 nm line. This study showed that with the CRDS mode the instrument can achieve detection sensitivity for Hg of ppt levels and that it is technologically feasible to incorporated a palm-size diode laser into the present instrument configuration. The experimentation is described below.

Hg sample solutions were prepared at four different concentrations, 50, 100, 200, and 500 ppm, for the CRDS measurements. A typical response of the instrument to Hg

sample concentration is shown in Fig. 5.7(a). Absorbance was determined based on Equation (5.3). The corresponding calibration curve of the measurements was plotted in Fig. 5.7(b), which has good linearity ($R^2 = 0.95$) in the sample concentration range of 50 - 500 ppm.

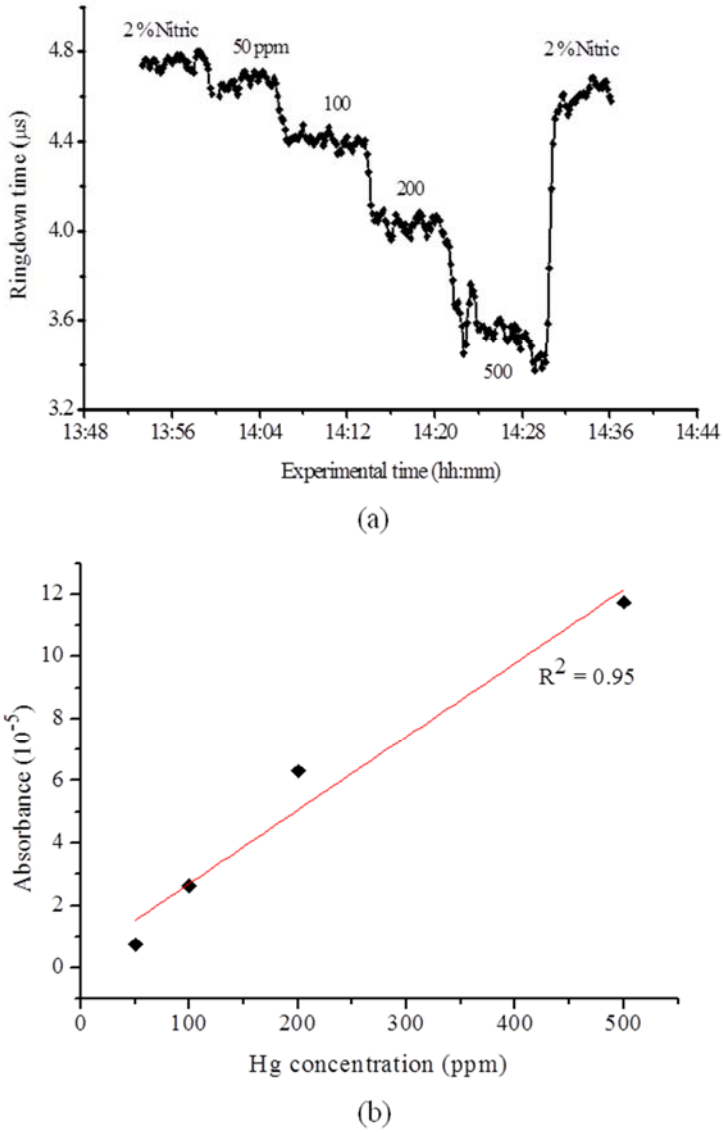

Figure 5.7 Measurements of Hg at different concentrations using the CRDS mode of the spectrometer at 405 nm.

(a) Response curve of the ringdown time versus Hg sample concentration in the range of 50 - 500 ppm. (b) Calibration curve (absorbance versus Hg sample concentration (ppm)) obtained using the data shown in (a).

The corresponding number densities of Hg in the metastable state were determined using Equation (5.4). The results are tabulated in Table 5.3. The number densities in the metastable state are on the orders of 10^7 - 10^8 atoms cm^{-3}. The minimum concentration of Hg in the sample solution measured was 50 ppm, which is related to a number density of 2.24 ppt in the 6s6p $^3P_0$ metastable Hg atoms in the plasma.

Table 5.3 Number densities of Hg in the metastable state measured by the CRDS mode of the spectrometer at 405 nm.

Hg sample concentration (ppm)	Absolute number density of Hg in the metastable state (atoms cm^{-3})	Concentration by volume in gas phase (ppt)
50	5.50×10^7	2.24
100	1.95×10^8	7.91
200	4.68×10^8	19.01
500	8.69×10^8	35.33

Population density of a metastable state is typically 10^4 - 10^5 times lower than the ground state population [60]. This is why the minimum detectable concentration of the sample solution was as high as 50 ppm. The low detection sensitivity for Hg using the 405 nm line does not mean a low sensitivity of the CRDS mode of the spectrometer. Several studies have reported that detection sensitivity of Hg using CRDS at 254 nm is as high as sub-ppt [40, 61-63]. Therefore, when a compact diode laser operating at 254 nm becomes available, it can be incorporated into this spectrometer for the detection of ultra-trace Hg down to ppt levels. With the same instrument platform, other elements,

including Cs, Be, Se, and U, can be measured using the CRDS when compact lasers sources are available for their strong transition lines.

5.6 Multi-element Measurements with OES Mode

In order to test the capability of multi-element measurement, Pb, As, Cd, Mn, Ni, P, and Sr, were also measured using the OES mode. The transition peaks and their corresponding energy levels were assigned based on the NIST and Harvard atomic databases [49, 64]. Similar to the Hg emission spectra, the relative intensity of the emission lines of different elements observed in the present experiment differs significantly from that reported in the NIST database. For example, for elements, such as Pb, Cd, and Mn, even the strongest lines observed in our experiments are different from those listed in the NIST. A database was created by conducting comparison of peak amplitude of the strongest emissions for all of the elements investigated in our experiments with those in the NIST; based on which, an appropriate transition line was carefully selected for an element to achieve the lowest detection limit, using calibration curves, with this instrument. As an example, Fig. 5.8 shows the calibration curves obtained using the Pb lines at 283.30, 368.34, and 405.78 nm, for which the detection limits for Pb were determined. Although the 368.34 nm line was the most prominent line obtained in this study, it did not yield the lowest detection limit. The lowest detection limit for Pb was determined to be 94 ppb at 405.78 nm, whereas the DL at 368.34 nm was determined to be 286 ppb. The higher DL using the 368.34 nm line was due to the higher background noise imposed by the N_2 (C-B) (1,3) and (0,2) bands existing in the region. DLs for other elements were determined by plotting calibration curves obtained using their prominent lines.

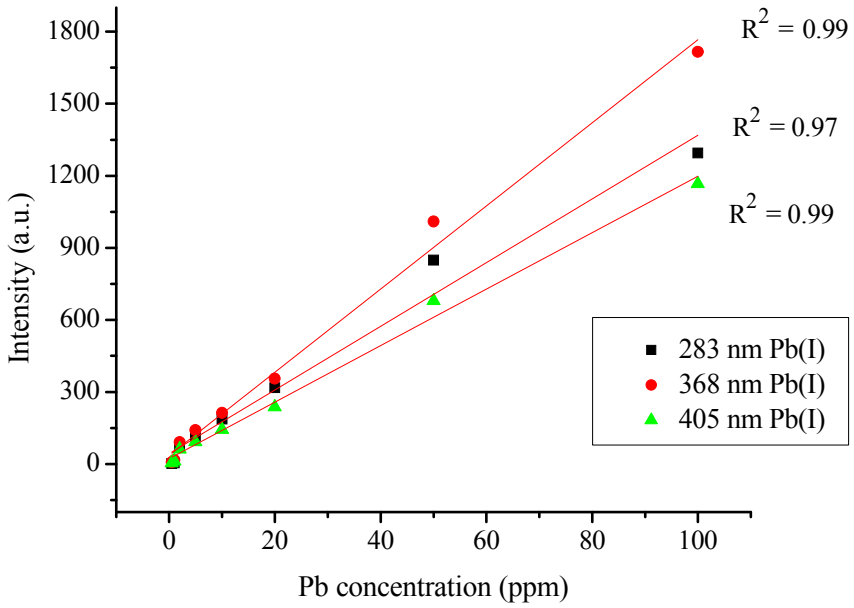

Figure 5.8 Calibration curves obtained using the prominent lines of Pb at 283 nm, 368 nm, and 405 nm.

It is worth noticing that possible spectral overlaps in the OES measurements of other elements need also be taken care in the selection of a transition line and pursuit of a low DL. For instance, the arsenic 234.98 nm transition line was the strongest, but it was located in the vicinity of a vibronic band of NO ($A\ ^2\Sigma^+ - X\ ^2\Pi$) system, which severely affected the DL of As. Therefore, a lowest DL for As of 1 ppm was obtained using the 228.81 nm line in the concentration range 1 - 500 ppm. The lowest DLs for other six elements, Cd, Mn, Ni, P, Pb, and Sr, achieved in the OES mode by carefully selecting the transition lines are listed in Table 5.4.

The spectral database created with OES mode of the spectrometer, by comparing the relative intensity ratios of spectral transition lines of the elements, namely As, Cd, Mn, Ni, and P, with the ones listed in the NIST database are tabulated in the Appendix A.

Table 5.4 Detection limits for As, Cd, Hg, Mn, Ni, P, Pb, and Sr obtained with the OES mode of the spectrometer.

Element	Gas flow Plasma/carrier (mL min^{-1})	Wavelength (nm)	Detection limit	R^2
As	500/446	228.81	1.1 ppm	0.98
		278.02	1.6 ppm	0.98
Cd	445/492	228.80	93 ppb	0.97
			45 ppb*	0.95
		326.10	33 ppb	0.98
			43 ppb *	0.96
Hg	500/480	253.65	44 ppb	0.99
			144 ppb *	0.94
Mn	475/462	257.61	47 ppb	0.99
		279.48	30 ppb	0.99
		403.30	81 ppb	0.99
Ni	462/517	300.24	144 ppb	0.99
		301.20	206 ppb	0.99
P	438/522	253.56	576 ppb	0.97
Pb	442/511	283.30	310 ppb	0.98
		368.34	286 ppb	0.99
			157 ppb*	0.96
		405.78	94 ppb	0.99
			440 ppb*	0.94
Sr	442/520	407.77	2 ppb	0.99
			21 ppb*	0.95

* In the presence of matrix; experiments were conducted at a plasma power of 150 W and plasma/carrier gas flow rates of 525/500 mL min^{-1}.

The presence of multi-element has been known to affect OES measurements of an element in terms of spectral interference, detection sensitivity, and accuracy [11, 21, 65-67]. Effort to study matrix effect of multiple elements on each individual element is exhaustive and beyond scope of this work. In this study, however, only matrix effects on Hg measurements were investigated. Hg concentration measurements in a mixture solution of Cd, Hg, Pb, and Sr elements were conducted in the OES mode. Hg samples in different concentrations, 2, 5, 10, 20, 30, and 40 ppm, were prepared by diluting standard (1000 ppm) sample solutions in a 2% nitric acid solution. Mixture solutions of Cd, Pb, and Sr in the same concentrations, but in different combinations, were added to the Hg sample solutions. The presence of the matrix elements, i.e. Cd, Pb, and Sr, in the Hg sample solutions was recognized by their characteristic transition lines appearing in the emission spectra. Figure 5.9 displays the screen shot showing a typical emission spectrum. Comparison of the case with the presence of the matrix elements with the case without the matrix elements showed that: (i) The increase rate of the emission intensity of Hg at 253.65 nm differed substantially in the presence of the matrix elements from the solutions without the matrix elements. (ii) Hg emission signal had higher fluctuations. (iii) The matrix effect had an adverse affect on the DL of Hg. In particular, the DL of Hg at 253.65 nm increased to 131 ppb, approximately 3 times higher than the DL, 44 ppb, without the matrix effects. The matrix effect may depend on several factors, such as analyte's penetration, vaporization effect, excitation potential and excitation cross section of the element, collisional quenching, collisional enhancement, electrons, atoms, and ion densities in the plasma, etc. [12]. A comprehensive study of matrix effect is a subject of future work, which is an important effort to further improve the instrument performance.

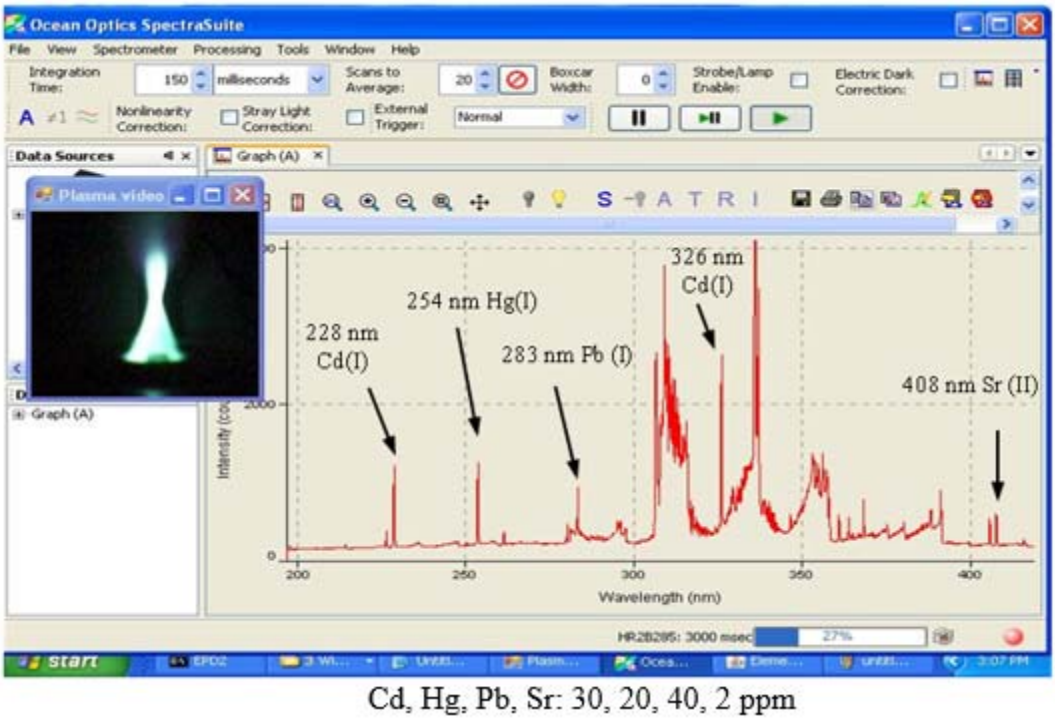

Figure 5.9 An example to show the capability of multi-element detection of the OES mode of the spectrometer

5.7 Advantages and Existing Challenges in the Dual-Mode Spectrometer

Advantages of this new dual-mode spectrometer are summarized below.

(1) A single MIP source for dual spectroscopy modes: A single MIP source was used in both OES and CRDS modes of the spectrometer. The robust MPT used as the microwave plasma source in the spectrometer is an efficient low-temperature excitation source for the optical emission studies. Apart from its efficient, excitation capability, it is also capable of maintaining a stable plasma continuously, even at low power (150 W) and low gas flow rates (450 mL min^{-1}) for a long period of time (7 - 9 hrs), an important requirement in real-time field monitoring of trace elements. At the same time, it can be used as an atomization source for the CRDS mode of the spectrometer. As demonstrated,

the plasma created by the MPT can also be efficiently used to atomize trace elements, such as Hg, Pb, As, U, Be, etc., present in liquid samples, followed by their detections in the CRDS mode.

(2) Different modes for different concentration ranges: As demonstrated in the emission studies of the various elements using the OES mode and ringdown measurements of the metastable Hg atoms using CRDS mode, the two modes of the spectrometer can be used in combination for detection of elements present in different concentration ranges. On the one hand, the OES mode can be used for the detection of elements in the concentration ranging from tens ppb to hundreds ppm. On other hand, the CRDS mode is capable of measuring absolute concentration as low as ppt levels.

(3) Self-calibration: Since the CRDS technique measures the absolute concentration of species; it does not need an external calibration. Using the CRDS mode to calibrate the OES measurements, the spectrometer is self-calibrated.

(4) Combination of modalities: The OES mode can measure multiple elements simultaneously, whereas the CRDS mode measures a single element each time. In field applications these two modalities are complementary. We may use the OES mode to indentify unknown elements and their relative concentration ranges and then use the CRDS mode to perform high sensitivity, absolute concentration measurements of a selected species.

(5) Instrumentation configurability: By extending the spectral response range of the spectrometer, many other elements can also be analyzed by the spectrometer. As demonstrated in the detection of the metastable Hg atoms using the 405 nm diode laser, a number of environmentally important elements, such as Hg (253.65 nm), Be (313.04

nm), As (419.08 nm), Cs (442.57 nm), Pb (405.78 nm), Se (241.35 nm), U (348.93 nm), etc., can also be measured using the CRDS mode when a compact diode laser at these wavelength becomes available.

Existing challenges in further development of the dual-mode spectrometer toward a standalone commercial instrument include two technology hurdles, requirements of a compact microwave plasma power generator that can be housed inside the spectrometer and a compact diode laser array that can be assembled in the spectrometer and cover multi-wavelength for CRDS measurements of multi-element in different wavelengths. Current sole source microwave plasma power generator used in the present study is too large to be housed inside the instrument frame and the operation of the plasma power generator is still manually controlled. Effort to scale down the size of the power generator is underway. Diode laser technologies advance rapidly, which will allow extension of diode laser wavelengths to near UV, where spectral fingerprints of most elements are located. A breakthrough in diode laser technology with this regard is conceivable. Electronic packaging of CRDS portion and its integration with the control electronics in the OES mode is not a technology issue since commercial CRDS spectrometers [68] for trace gases detection have demonstrated the instrumentation capability. We expect CRDS instrumentation for trace elements will soon be available when the two challenges are overcome.

5.8 Conclusion

A novel dual-mode OES-CRDS plasma spectrometer has been developed for measurements of multi-element. Selected environmentally important elements, As, Cd, Hg, Mn, Ni, P, Pb, and Sr, were successfully measured using the OES mode of the

spectrometer. Given the portability of the spectrometer, desirable DLs for As, Cd, Hg, Mn, Ni, P, Pb, and Sr, were determined to be 1100, 33, 44, 30, 144, 576, 94, and 2 ppb, respectively.

As an example, the operation of the instrument has been demonstrated by measurements of elemental mercury both with the OES mode and the CRDS mode. Operating in the CRDS mode, the spectrometer demonstrated measurements of Hg in the sample concentration range of 50 - 400 ppm using the 405 nm line, corresponding to an optical transition from the 6s6p $^3P_0$ metastable state. The absolute number densities of Hg in the metastable state were determined to be on the orders of 10^7 - 10^8 atom cm^{-3}, which corresponds to parts per trillion (ppt) with respect to the average number density of air under atmospheric condition. As pointed out earlier that the ppt level of detection of 6s6p $^3P_0$ metastable state of Hg in the plasma does not represents a ppt level of detection of Hg in the actual sample. However, the measurement of the Hg in the metastable state demonstrates the instrument's capability to achieve detection sensitivity in that range. We can expect that whenever a small size diode laser of a specific wavelength, corresponding to each of the different elements, e.g. 253.65 nm for Hg, 313.04 nm for Be, 419.08 nm for As, 442.57 nm for Cs, 405.78 nm for Pb, 241.35 nm for Se, 348.93 nm for U, and similarly for others, becomes available in the market, the diode laser can easily be incorporated into the spectrometer for highly sensitive measurements using the CRDS mode. The radiation trapping effect of the 253.65 nm transition line was observed to hamper Hg concentration measurements in the higher concentration region. The RT effect suggested that two different lines at 254 and and 365 nm should be selected for Hg OES measurements in the low concentrations (< 50 ppm) and high concentrations (> 50

ppm), respectively. The matrix effect due to the presence of other elements on OES measurements of Hg affected DL by a factor of three. One of the advantages of the dual-mode spectrometer is that the spectrometer has a large measuring dynamic range, potential from a few ppt to hundreds ppm for Hg when operating in combination of the two modes and the CRDS mode not only has a higher detection sensitivity but also can calibrate the OES to obtain absolute concentration of an element of interest. The demonstration of the integration of the OES and CRDS modes in a single portable spectrometer may extend the CRDS technology from current portable trace gas analysis to future portable trace element analysis, enabling many new field applications.

5.9 Acknowledgements

This work is supported by the US Department of Energy grant DEFC01006EW07040 and the National Science Foundation grant No. CBET-1066486.

5.10 References

1. Regulatory compliances Monitoring by Atomic Absorption Spectroscopy, edited by S. A. Katz and S. W. Jennings (Verlag Chemie International, Deerfield Beach, FL, 1983).

2. X-Ray Fluorescence Analysis, edited by T. G. Dzubay (Ann Arbor Science, Ann Arbor, MI, 1977).

3. Inductively Coupled Plasmas in Analytic Atomic Spectrometry, 2nd ed., edited by A. Montaser and D. W. Goligthly (VCH, New York, 1992).

4. C. C. Trassy and R. C. Diemjaszonek, J. Anal. At. Spectrom. 10, 661 (1995).

5. G. A. Meyer and K. W. Lee, Process Contr. Qual. 6, 187 (1994).

6. W. Flower, L. Peng, C. Woods, N. B. French, K. Hencken, H. Johnson, R. Renzi, and D. Trujillo, A Continuous Emissions Monitor for Metals: Field Demonstration of a Prototype Probe, SAND 95-8540 (Sandia National Laboratories, Livermore, CA, 1995).

7. S. Tanaka, N. Yasushi, N. Sto, T. Fudasawa, S. J. Santosa, K. Yamanaka, and T. Ootoshi, J. Anal. At. Spectrom. 13, 135 (1998).

8. C. Ludke, E. Hoffmann, and Skole, J., Fresnius', J. Anal. Chem. 350, 272 (1994).

9. M. W. Blades, P. Banks, C. Gill, D. Huang, C. Le Blanc, and D. Liang, IEEE Trans. Plasma Sci. PS-19, 1090 (1991).

10. A. T. Zander, Anal. Chem. 58, 1139A (1986).

11. K. Jankowski, J. Anal. At. Spectrom. 14, 1419 (1999).

12. K. Jankowski and M. Dreger, J. Anal. At. Spectrom. 15, 269 (2000).

13. Y. Su, Z. Jin, Y. Duan, M. Koby, V. Majidi, J. A. Olivares, and S. P. Abeln, Anal. Chim. Acta 422, 209 (2000).

14. Y. Duan, S. T. Scherrer, S. P. Koirala, C. Wang, and C. B. Winstead, Anal. Chim. Acta 532, 47 (2005).

15. P. P. Woskov, D. Y. Rhee, P. Thomas, D. R. Cohn, J. E. Surma, and C. H. Titus, Rev. Sci. Instrum. 67, 3700 (1996).

16. P. P. Woskov, K. Hadidi, P. Thomas, K. Green, and G. Flores, Waste Manag. 20, 395 (2000).

17. Y. Duan, Y. Su, Z. Jin, and S. P. Abeln, Anal. Chem. 72, 1672 (2000).

18. A. T. Zander and G. M. Hieftje, Appl. Spectrosc. 35, 357 (1981).

19. M. Selby, R. Rezaaiyaan, and G. M. Hieftje, Appl. Spectrosc. 41, 5749 (1987).

20. O. T. Akinbo and J. W. Carnahan, Appl. Spectrosc. 52, 1079 (1998).

21. Q. Jin, G. Yang, A. Yu, J. Liu, H. Zhang, and Y. Ben, Abstracts Book of Pittcon'85, abstract no. 1171 1985.

22. Q. Jin, F. Wang, C. Zhu, D. M. Chambers, and G. M. Hieftje, J. Anal. At. Spectrom. 5, 487 (1990).

23. Q. Jin, C. Zhu, M. Borer, and G. M. Hieftje, Spectrochim. Acta B 46, 417 (1991).

24. Q. Jin, W. Yang, F. Liang, H. Zhang, A. Yu, Y. Cao, J. Zhou, and B. Xu, J. Anal. At. Spectrom. 13, 377 (1998).

25. J. A. C. Broekaert and V. Siemens, Spectrochim. Acta B 59, 1823 (2004).

26. B. Rosenkranz and J. Bettmer, Tr. Anal. Chem. 19, 138 (2000).

27. Y. Duan, Y. Su, Z. Jin, and S. P. Abeln, Rev. Sci. Instrum. 71, 1557 (2000).

28. K. J. Jankowski, E. Reszke, J. A. Broekaert, and U. Enge, in Microwave Plasma Systems in Optical and Mass Spectroscopy: Encyclopedia of Analytical Chemistry (John Wiley & Sons, Ltd, 2011).

29. K. J. Jankowski and E. Reszke, Microwave Induced Plasma Analytical Spectrometry (RSC Publishing, Cambridge, UK, 2011)

30. Elemetric Instrument LLC.

31. G. P. Miller and C. B. Winstead, J. Anal. At. Spectrom. 12, 907 (1997).

32. C. Wang, F. J. Mazzotti, G. P. Miller, and C. B Winstead, Appl. Spectrosc. 56, 386 (2002).

33. Cavity-Ringdown Spectroscopy: An Ultratrace-Absorption Measurement Technique, edited by K. W. Busch and M. A. Busch, ACS Symposium Series (720 Oxford University Press, 1999).

34. G. Berden, R. Peeters, and G. Meijer, Int. Rev. Phy. Chem. 19, 565 (2000).

35. M. Mazurenka, A. J. Orr-Ewing, R. Peverallb, and G. A. D. Ritchie, Annu. Rep. Prog. Chem. Sect. C 101, 100 (2005).

36. C. Wang, C. Winstead, and Y. Duan, Method and apparatus for elemental and isotope measurements and diagnostics-microwave induced plasma-cavity ring-down spectroscopy, U.S. Patent NO. 7,054,008 (May, 2006).

37. C. Wang, F. J. Mazzotti, G. P. Miller, and C. B Winstead, Appl. Spectrosc. 57, 1167 (2003).

38. Y. Duan, C. Wang, and C. B. Winstead, Anal Chem, 75, 2105 (2003).

39. Y. Duan, C. Wang, S. T. Scherrer, and C. B. Winstead, Anal. Chem. 77, 4883 (2005).

40. C. Wang, S. T. Scherrer, Y. Duan, and C. B. Winstead, J. Anal. At. Spetrom. 20, 638 (2005).

41. C. Wang, J. Anal. At. Spectrom. 22, 1347 (2007).

42. C. Wang, S. P. Koirala, S. T. Scherrer, Y. Duan, and C. B. Winstead, Rev. Sci. Instrum. 75, 1305 (2004).

43. C. Wang, N. Srivastava, S. T. Scherrer, P-Rey Jang, T. S. Dibble, and Y. Duan, Plasma Sources Sci. Technol. 18, 025030 (2009).

44. C. Wang, P. Sahay, and S. T. Scherrer, J. Anal. At. Spectrom. 27, 284 (2012).

45. A. E. Siegman, Laser (University Science Books, Mill Valley, CA, 1986).

46. G. F. Kirkbright and M. Sargent, Atomic Absorbance and Fluorescence Spectrometry (Academic Press, London, 1974).

47. A. A. Radzig and B. M. Smirnov, Reference Data on Atoms, Molecules, and Ions (Springer-Verlag, New York, 1985).

48. J. Luque, LIFBASE (Version 2.0).

49. NIST Atomic Database: http://physics.nist.gov/PhysRefData/ASD/lines_form.html.

50. M. Schmidt and H. Conrads, in Plasma Sources, in Low Temperature Plasmas: Fundamentals, Technologies, and Techniques, edited by R. Hippler, H. Kersten, M. Schmidt and K. H. Schoenbach (WILEY-VCH Verlag GmbH & Co KGaA, Weinheim, Germany, 2008), p.363.

51. C. Tenderoa, C. Tixiera, P. Tristanta, J. Desmaisona, and P. Leprinceb, Spectrochim. Acta B 61, 2 (2006).

52. C. O. Laux, T. G. Spence, C. H. Kruger, and R. N. Zare, Plasma Sources Sci. Technol. 12, 125 (2003).

53. P. J. Walsh, Phys. Rev. 116, 511 (1959).

54. K. Wani, J. Appl. Phys. 68, 5052 (1990).

55. M. Baeva and D. Reiter, Plasma Chem. Plasma Process. 23, 371 (2003).

56. Radiation Trapping in Atomic Vapors, edited by A. F. Molisch and B. P. Oehry, (Oxford, Clarendon, 1998).

57. M. T. Herd, J. E. Lawler, and K. L. Menningen, J. Phys. D: Appl. Phys. 38, 3304 (2005).

58. K. Hadidi, P. P. Woskov, K. Green, and P. Thomas, J. Anal. At. Spectrom. 15, 601 (2000).

59. C. Wang, P. Sahay, and S. T. Scherrer, Phys. Lett. A 375, 2366 (2011).

60. K. Becker and C. C. Lin, in Elementary Collision Process in Plasmas, in Low Temperature Plasmas: Fundamentals, Technologies, and Techniques, edited by R. Hippler, H. Kersten, M. Schmidt and K. H. Schoenbach, (WILEY-VCH Verlag GmbH & Co KGaA, Weinheim, Germany, 2008), p.47.

61. S. Q. Tao, F. J. Mazzotti, C. B. Winstead, and G. P. Miller, Analyst 125, 1021 (2000).

62. C. C. Carter, A Cavity Ring-Down Spectroscopy mercury continuous emission monitor, sensor research and development corporation (Orono, Maine 04473, 2004), p.118

63. X. Faïn, H. Moosmüller, and D. Obrist, Atmos. Chem. Phys. 10, 2879 (2010).

64. R. L. Kurucz, Harvard Atomic Data Base http://www.cfa.harvard.edu/amp/ampdata/kurucz23/sekur.html.

65. J. H. Urh and J.W. Carnahan, Appl. Spectrosc. 40, 877 (1986).

66. W. Yang, H. Zhang, A. Yu, and Q. Jin, Microchem. J. 66, 147 (2000).

67. Z. Zhang and K. Wagatsuma, Spectrochim. Acta B 57, 1247 (2002).

68. C. Wang, N. Srivastava, B. A. Jones, and R. B. Reese, Appl. Phys. B 92, 259 (2008).

CHAPTER VI

ABSOLUTE MEASUREMENTS OF ELECTRON IMPACT EXCITATION CROSS-SECTIONS OF ATOMS USING CAVITY RINGDOWN SPECTROSCOPY

6.1 Abstract

A new method of using cavity ringdown spectroscopy (CRDS) technique to measure apparent electron impact excitation cross sections (EIECS) for different energy levels of an atom is described. The method involves measurements of absolute population densities of energy levels of concern using high sensitivity CRDS, leading to an analytical expression of EIECS as a function of the population densities. Determination of EIECS in this method does not require an external calibration. The proposed method is validated by determining EIECS of the metastable levels of Hg ($6s6p\ ^3P_0$) and Ne ($2p^5 3s\ ^3P_2$), and the results are in good agreement with cross sections reported in the literature. The population densities in both cases were extracted from published data. This method exhibits promising potential for absolute measurements of EIECS of metastable energy levels.

6.2 Introduction

Measurements of electron impact excitation cross section (EIECS) of regular energy levels (optical transitions allowed) or metastable energy levels (optical transitions forbidden) are generally carried out with the electron energy loss technique, optical

emission spectroscopy (OES) technique, or theoretical calculations [1-5]. In 1981, Lin *et al.* introduced a method based on laser induced fluorescence (LIF) spectroscopy along with OES to measure absolute EIECS of metastable levels. This method has remained to be one of the most extensively used experimental methods of measuring EIECS over the last 30 years although their latest advancement has evolved the method further to use OES only [1,6]. On the other hand, the conventional single-pass absorption spectroscopy technique attempted once for EIECS measurements has been abandoned and is not pursued these days [7-8].

The measurement of EIECS using the LIF-OES method chiefly relies on measuring relative intensities of the emission lines [1]. The absolute EIECS is determined with the help of an external calibration process. Typically the method requires one first to express the cross section of a desired energy level in terms of a known excitation cross section, emission line intensities, electron energy, etc. Then, a change in the emission line intensities is recorded with change in electron energy; consequently an excitation function is obtained. Afterwards a known cross section is used to determine the absolute EIECS of the desired energy level at the respective electron energies. This process requires not only emission line intensities to be measured, but also the cross section of another energy level to be known for the purpose of calibration.

In our previous work [9], we demonstrated a new method to determine EIECS using cavity ringdown spectroscopy (CRDS) along with OES. The method involved solving a set of steady state population rate equations using the CRDS measured population density of one of the energy levels and the intensity ratio of two different emission lines. The experiments were conducted with atmospheric pressure microwave

plasma. The apparent EIECS of three energy levels of mercury (Hg), namely 6s6p $^3P_0$, 6s6p $^3P_1$, and 6s7s $^3S_1$, were determined simultaneously. The motivation of the previous work was to explore an alternative method of determining the absolute cross sections using CRDS. In this work, we present a modified version of the method described previously to measure EIECS of an atom [9]. The present method is explained with a three energy level system, as an example. An analytical solution for EIECS has been derived from the steady state population rate equations; and the solution turns out to be a function of the population densities of the desired excited state and the ground state. Under the assumption that electron impact excitation is the dominant mechanism responsible for the density population of the energy levels, the population density of the excited level has a linear relationship to the ground state population density (Eq. 6.8). In such case, EIECS can be directly determined if the two population densities are known, i.e. in this case, experimentally determined by CRDS, and the method does not require an external calibration process. We applied the proposed method to determine EIECS in the two published cases: (i) EIECS of the 6s6p $^3P_0$ metastable level of Hg using data from our previous work [10] and (ii) EIECS of the $2p^5 3s$ $^3P_2$ metastable level of Ne with the data reported in the literature [11].

6.3 The Method

The method is described with a three-energy level system, as shown in Fig. 6.1. In this particular example, we assume that energy levels *a* and *b* are two excited levels with the energy level *a* being metastable (optical transitions not allowed) and the energy level *b* is a regular excited level (optical transitions allowed). The ground state is represented by *g*. The target atoms, present in the ground state *g*, are exposed to a beam of mono-

energetic electrons. As a result, some of the atoms in the ground state are excited to the higher energy levels *a* and *b* by the electron impact excitation mechanism. The metastable level *a* being optically forbidden does not radiate. However, the spontaneous transition $b \rightarrow a$ results in radiation at wavelength λ. The atoms in the metastable level *a* is further pumped to the higher level *b* with a cavity ringdown laser beam at the wavelength λ.

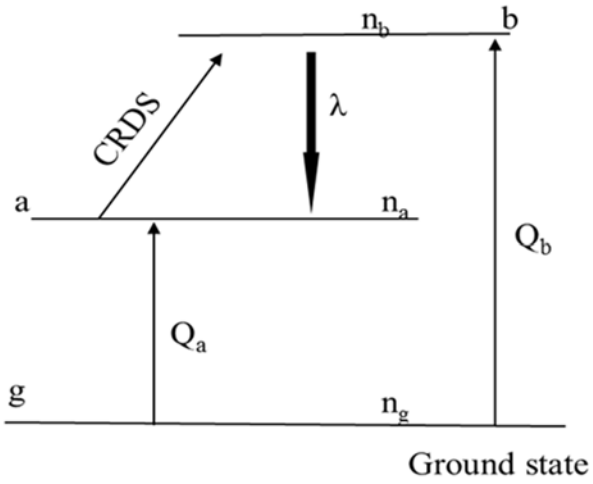

Figure 6.1 Schematic of a simple three-energy level system.

Under the assumption that the excitation process is due solely to electron impact excitation mechanism and that the excited energy level de-excites to lower energy levels only through optical emission processes, namely spontaneous or stimulated emissions, at any given time the population rate equations for the energy levels *a* and *b* can be given as [1],

$$\frac{dn_a}{dt} = n_g\left(\frac{J}{e}\right)Q_a^{dir} + \sum_{\substack{j>a \\ j\neq b}} n_j A_{ja} + n_b A_{ba} - B_{ab}\rho(\nu)n_a + B_{ba}\rho(\nu)n_b - n_a A_a \tag{6.1}$$

$$\frac{dn_b}{dt} = n_g\left(\frac{J}{e}\right)Q_b^{dir} + \sum_{j>b} n_j A_{jb} + B_{ab}\rho(\nu)n_a - B_{ba}\rho(\nu)n_b - n_b A_b \tag{6.2}$$

where n_a, n_b, and n_g are the population densities in the energy levels a, b, and the ground state, respectively. The term $\left(\frac{J}{e}\right)$ is a measure of electron flux in the electron beam, where J is the electron current density and e is the electron charge. A_{ij} and B_{ij} are the spontaneous and stimulated Einstein coefficients corresponding to the lower energy level i and the upper energy level j. $\rho(\nu)$ is the energy density of the laser beam at frequency ν.

Under steady state condition, we have

$$n_g\left(\frac{J}{e}\right)Q_a^{A} + n_b A_{ba} - B_{ab}\rho(\nu)n_a + B_{ba}\rho(\nu)n_b - n_a A_a = 0 \tag{6.3}$$

$$n_g\left(\frac{J}{e}\right)Q_b^{A} + B_{ab}\rho(\nu)n_a - B_{ba}\rho(\nu)n_b - n_b A_b = 0 \tag{6.4}$$

where $Q_a^{A} = Q_a^{dir} + \sum_{j>a,\, j\neq b} Q_{ja}$ is known as the apparent cross section for the energy level a, with the cascaded term $\sum_{j>a,\, j\neq b} n_j A_{ja}$ replaced by $\sum_{j>a,\, j\neq b} Q_{ja}$ that is known as the optical cross sections. From Eq. (6.3) and Eq. (6.4) we have

$$n_a = \frac{n_g\left(\frac{J}{e}\right)\left[Q_a^A + \frac{Q_b^A(A_{ba} + B_{ba}\rho)}{(A_b + B_{ba}\rho)}\right]}{A_a + B_{ab}\rho - \frac{B_{ab}\rho(A_{ba} + B_{ba}\rho)}{(A_b + B_{ba}\rho)}} \tag{6.5}$$

In a CRDS experiment, more than 99% of the incident laser power is reflected back, and only a fraction (<1%) of the incident beam energy interacts with the absorbing molecules inside the cavity. This results in a significant reduction in the magnitude of the term $B_{ab}\rho$ inside the cavity in comparison to outside the cavity.

In our CRDS system, the ringdown laser beam from the OPO (optical parametric oscillator) system at 404.65 nm has a typical photon density outside the cavity of on the order of 10^{17} photons cm^2 s^{-1}, corresponding to a beam energy of $B_{ba}\rho \sim 10^4$ s^{-1} inside the cavity. So are for the other CRDS systems, the beam energy inside a ringdown cavity remains approximately of the same order. Typically, the spontaneous emission rates (Einstein constant A) A_b and A_{ba} are on the orders of 10^8 and 10^7 s^{-1}, respectively. Therefore, in a CRDS measurement, we can consider

$$A_b + B_{ba}\rho \approx A_b \text{ and } A_{ba} + B_{ba}\rho \approx A_{ba}$$

Therefore, Eq. (6.5) is modified to be

$$n_a = \frac{n_g\left(\frac{J}{e}\right)\left(Q_a^A + \frac{Q_b^A A_{ba}}{A_b}\right)}{A_a + B_{ab}\rho\left(1 - \frac{A_{ba}}{A_b}\right)} \tag{6.6}$$

Since the optical transition cross section from the energy level *b* to *a* is given as $Q_{ba} = \frac{Q_b^A A_{ba}}{A_b}$,

Eq. (6.6) can be further modified to

$$n_a = \frac{n_g\left(\frac{J}{e}\right)\left(Q_a^A + Q_{ba}\right)}{A_a + B_{ab}\rho\left(1 - \frac{A_{ba}}{A_b}\right)} \tag{6.7}$$

Note that the aforementioned definition of Q_a^A, i.e. $Q_a^A = Q_a^{dir} + \sum_{j>a, j\neq b} Q_{ja}$, does not include the optical cross section term Q_{ba}. Therefore, the term $\left(Q_a^A + Q_{ba}\right)$ in Eq. (6.7) is actually the total apparent cross section of energy level *a*, denoted as Q_a^{App}. Therefore, from Eq. (6.7) we have

$$n_a = \frac{n_g\left(\frac{J}{e}\right)Q_a^{App}}{A_a + B_{ab}\rho\left(1 - \frac{A_{ba}}{A_b}\right)} \tag{6.8}$$

When the laser is off, i.e. $\rho = 0$, from Eq. (6.8), we have

$$n_a(off) = \frac{n_g\left(\frac{J}{e}\right)Q_a^{App}}{A_a} \tag{6.9}$$

The expression in Eq. (6.9) is the same as should be expected from the steady state condition of excitation and de-excitation of energy levels.

In Eq. (6.8), the terms in the denominator on the right hand side are experimental parameters. The electron current density J is also known. The excitation cross section empirically depends on the energy of the colliding electrons. Therefore, as long as the current density and the energy of the electrons remain constant and electron impact excitation remains the dominant mechanism of excitation, the population density n_a should depend linearly on the ground state population density n_g. Therefore, if the two population densities are known, the absolute cross section Q_a^{App} can be determined analytically from the slope of the linear plot between n_a and n_g. From Eq. (6.8), the slope m of the linear plot between n_a and n_g is obtained as

$$m = \frac{\left(\frac{J}{e}\right) Q_a^{App}}{A_a + B_{ab}\rho\left(1 - \frac{A_{ba}}{A_b}\right)} \tag{6.10}$$

Therefore, the cross section Q_a^{App} can be determined as

$$Q_a^{App} = \frac{m\left[A_a + B_{ab}\rho\left(1 - \frac{A_{ba}}{A_b}\right)\right]}{\left(\frac{J}{e}\right)} \tag{6.11}$$

6.4 Applicability of the Method

In order to evaluate this method, instead of setting up an experiment to measure n_a and n_g, we extracted n_a and n_g from two published cases, as an example, to demonstrate applicability of this method by determining the absolute cross section Q_a^{App}. The two

examples are the measurements of apparent cross section of the metastable 6s6p $^3P_0$ level of Hg and the metastable $2p^5 3s$ $^3P_2$ level of Ne.

6.5 Case 1- Apparent EIECS of Metastable 6s6p $^3P_0$ Level of Hg

In case 1, we compare the EIECS of metastable 6s6p $^3P_0$ level of Hg determined in this work with that determined in our previous work [9]. In the previous work, EIECS of the 6s6p $^3P_0$ level of Hg was determined with a plasma-CRDS system, where the metastable Hg atoms were generated in the plasma. A microwave plasma was used as an excitation source for Hg atom generation as well as the source of energetic electrons in the experiment. For this type of atmospheric pressure argon microwave plasma operated at 150 W, typically the electron energies are in the range of 0.5 - 10 eV and electron number density on the order of ~10^{12} - 10^{14} cm^{-3}. The determination of the cross sections in that work was accomplished with the help of both the CRDS and OES measurements [9]. A set of steady state population rate equations for a four-energy level system was solved with the help of the measured population density of the 6s6p $^3P_0$ metastable level and the ratio of the two emission lines at 253.65 and 404.65 nm. The cross section for the metastable level of Hg was determined to be $(1.7 \pm 0.4) \times 10^{-17}$ cm^2.

However, in this work, EIECS of the same 6s6p $^3P_0$ level of Hg has been determined solely from the number densities of the 6s6p $^3P_0$ level and ground energy level of Hg without using the additional OES measurements. The population densities of these two energy level have been represented by n_a and n_g, respectively, in the subsequent text. The absolute population density n_a present in the plasma was measured using the CRDS technique at a laser wavelength of 404.65 nm. The measured population density of this metastable 6s6p $^3P_0$ level Hg was on the order of 10^7 - 10^8 cm^{-3} when total Hg atoms

on the order of 10^{11} - 10^{12} cm^{-3} were injected into the plasma [10]. Using the n_a and n_g data from our previous work [10], we plotted a graph of the population density n_a versus n_g, as shown in Fig. 6.2.The plot between n_a and n_g in Fig. 6.2 attained good linearity of $R^2 = 0.99$ and a slope $m = 2 \times 10^{-4}$ (a.u.). Using the other known parameters of the microwave plasma used in the experiment, conducted in the works of [9] and [10], such as the electron flux $\left(\frac{J}{e}\right)$ $(= n_e v) \sim 5.2 \times 10^{21}$ cm^{-2} s^{-1}, corresponding to 5 eV electrons, and others as listed in Table 6.1, the apparent cross section Q_a^{App} for the metastable 6s6p $^3P_0$ level of Hg is determined to be $(3.03 \pm 0.15) \times 10^{-17}$ cm^2 based on Eq. (6.11). This number is certainly an approximation because the plasma is not a mono-energetic source of the electrons, and the electron number density inside the plasma is not uniformly distributed. However, the cross section of the 6s6p $^3P_0$ level of Hg determined by this method is still on the same order of magnitude, within the range 1.0×10^{-17} - 8.0×10^{-17} cm^2 as reported in the literature [9,12,13].

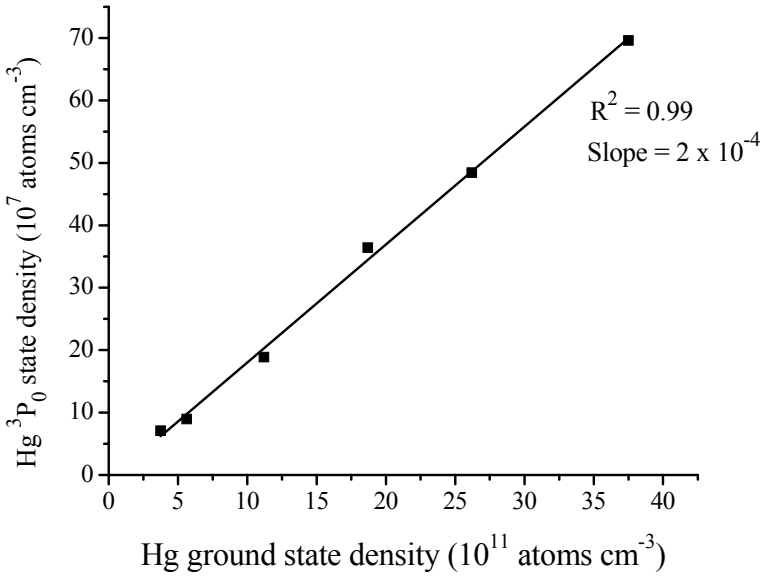

Figure 6.2 The population density of the metastable 6s6p $^3P_0$ level Hg versus the ground state population density measured using the CRDS technique in the microwave plasma.

[Data obtained from Ref. 10.]

6.5.2 Case 2-Apparent EIECS of Metastable $2p^5 3s\ ^3P_2$ Level of Ne.

In case 2, we applied the method described in this work to determine the EIECS of metastable $2p^5 3s\ ^3P_2$ level of Ne. The absolute EIECS of the $2p^5 3s\ ^3P_2$ (also represented as $1s_5$ in Paschen's notation) level of Ne at different electron energies were reported earlier by Phillips *et al.* [1,14]. Their measurement technique involved the excitation of the ground state Ne atoms, which were confined in a closed chamber at a reduced pressure of 1 - 25 mT, to the $1s_5$ level via a mono-energetic beam of electrons. The Ne atoms in the $1s_5$ level were further pumped to the higher level $2p_2$ via laser absorption at 588.2 nm. The change in the fluorescence intensity of the transition $2p_2 \rightarrow 1s_5$ with the change in the electron energy was recorded; consequently, an excitation

function was obtained. After performing a calibration using the results in Ref. 15, the apparent cross sections Q_a^{App} for the metastable $1s_5$ level of Ne were determined for different electron energies. The cross section increases rapidly from 1×10^{-19} cm^2 at threshold, to the maximum, i.e. 3.3×10^{-18} cm^2, at an electron energy of 25 eV. After that maximum, the cross section gradually decreases with increase in the electron energy.

To determine the EIECS of the same metastable $1s_5$ level of Ne with the method described in this work, we used the population densities of $1s_5$ and ground level of Ne reported in Ref. 11. In that work, the ground state population densities n_g were determined based on the ideal gas law, $P = n_g k T_g$, where P is the chamber pressure, k is the gas constant, and T_g is the gas temperature. The experimental system was an inductively coupled Ne plasma operated at 600 W power at five different pressures, namely 5, 10, 15, 20, and 25 mT. The chamber pressures were measured by an ion gauge for two different ranges of pressures inside the chamber. In that work, the gas temperature T_g for the Ne plasma was approximated with an Ar plasma operated under similar experimental conditions. The gas temperature increased from 500 to 620 K when the pressure in the chamber was increased from 5 to 25 mT. Corresponding to each n_g determined at the five different pressures in the Ne plasma, the metastable population densities n_a were also measured using white light absorption spectroscopy [11,16].

Now we extract the parameters from the experimental system and use their measured n_a and n_g to determine the apparent excitation cross section based on Eq. (6.11). First, we assume that n_a was not determined by the white light absorption spectroscopy technique as reported in Chapter 11 in Ref. 11. Instead we use CRDS at the same wavelength, 588.2 nm, as used in Ref. 1, to determine the number density n_a present in a

pure Ne inductively coupled plasma (ICP). The energy density term $B_{ab}\rho = 2 \times 10^6$ s^{-1} [1] is reduced to 2×10^4 s^{-1} inside the ringdown cavity if the mirror reflectivity in the CRDS system is 99%. The electron number density was estimated from the electron energy distribution function (EEDF) obtained for the same Ne plasma by averaging the electron density over the pressure range 10 - 25 mT [Chapter 12 in Ref.11]. Here it should be noted that an ICP is not a mono-energetic source of electrons. The EEDF showed that the electron energies in the ICP were in the range of 0 - 35 eV. The maxima, i.e. the highest electron number density, lies around 5 eV [11]. The EEDF further exhibited that there was a sharp decrease at 20 eV. Therefore, we chose the intermediate electron energy, 20 eV, and another electron energy at 25 eV where the cross section was the largest [1,14], to determine the EIECS of the $1s_5$ level of Ne using this method and compared them with the reported values in the literature. The averaged number density of the electrons at 20 and 25 eV were estimated to be 4.75×10^9 cm^{-3} and 2.80×10^9 cm^{-3}, respectively [11]. The parameters, such as A_b and A_{ba}, were obtained from the NIST atomic database [17], where A_a was estimated by considering the collisional quenching of the metastable levels under the given experimental conditions. The values of all of the parameters used are listed in Table 6.1.

Table 6.1 Experimental parameters; comparison of EIECS of metastable level of Hg and Ne determined in this work and that reported in literature.

Energy level	A_a (sec^{-1})	$B_{ab}\rho$ [(a)] (sec^{-1})	A_{ba} (sec^{-1})	A_b (sec^{-1})	Slope	Electron energy (eV)	EIECS- this work (cm^2)	EIECS-literature reported (cm^2)
6s6p $^3P_0$ Hg	7.9×10^8 [(b)]	1.3×10^5	2.1×10^7	1.24×10^8	2×10^{-4}	5	3.03×10^{-17}	1.0×10^{-17} - 8.8×10^{-17} [(c)]
$2p^53s$ $^3P_2$ Ne	1.9×10^4 [(b)]	2×10^4	2.3×10^7	4.7×10^8	6×10^{-5}	20 25	1.9×10^{-18} 2.9×10^{-18}	1.5×10^{-18} - 3.0×10^{-18} [(d)] 3.3×10^{-18} [(d)]

(a) Inside the ringdown cavity (i.e. after reducing 99%); (b) Estimated; (c) From Refs. 9, 12, 13; (d) From Refs. 14,18.

The linear plot between n_a and n_g yielded a slope of 6×10^{-5} (a.u.) ($R^2 = 0.98$), as shown in Fig. (6.3). Using Eq. 6.11, the apparent cross sections Q_a^{App} for the $1s_5$ level of Ne at 20 and 25 eV were determined to be 1.9×10^{-18} and 2.9×10^{-18} cm^2, respectively.

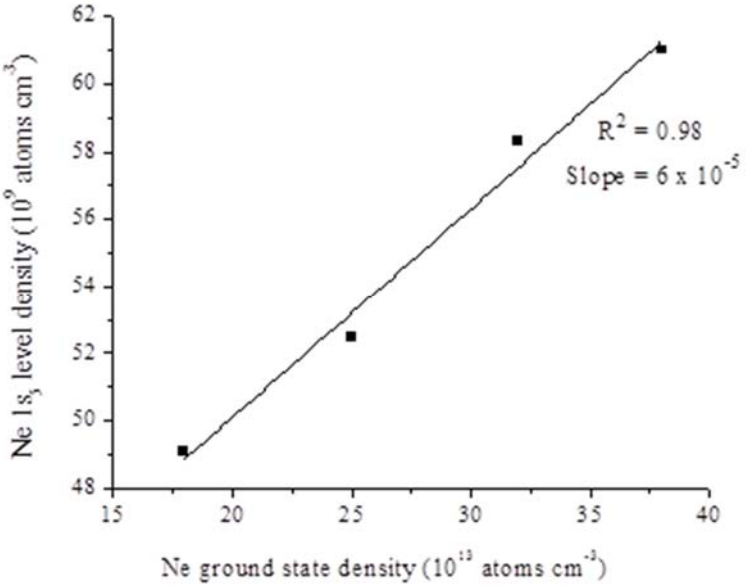

Figure 6.3 The population density of the metastable $2p^5$ 3s $^3P_2$ level Ne versus the ground state population density measured in a pure Ne plasma in the inductively coupled plasma

[from Chapter 11 in Ref. 11].

The cross section at the electron energy of 20 eV, 1.9×10^{-18} cm^2, determined in this work, falls between 1.5×10^{-18} cm^2 by Phillips *et al.* [1,14] and 3.0×10^{-18} cm^2 by Milatz *et al.* [14,18]. Similarly, the cross section, 2.9×10^{-18} cm^2 , determined at the electron energy of 25 eV is also in good agreement with the reported cross section at 25 eV, 3.3×10^{-18} cm^2 that is the largest cross section of the $1s_5$ level of Ne [1,14,18].

6.6 Discussion

From Eq. (6.11), the apparent cross section Q_a^{App} is determined as

$$Q_a^{App} = \frac{n_a\left[A_a + B_{ab}\rho\left(1 - \frac{A_{ba}}{A_b}\right)\right]}{n_g\left(\frac{J}{e}\right)} \tag{6.12}$$

Therefore, the maximum error in the measurement of Q_a^{App} using the proposed method can be estimated as

$$\frac{\Delta Q_a^{App}}{Q_a^{App}} = \frac{\Delta n_a}{n_a} + \frac{\Delta n_g}{n_g} + \frac{\Delta \rho}{\rho} + \frac{\Delta J}{J} \quad . \tag{6.13}$$

The first term on the right hand side represents the error in the measurement of the population density using the CRDS technique; the second term is the error in the measurement of the ground state population density; the third and the fourth terms are the errors in the measurements of the laser beam energy density and the electron current density, respectively.

Typically, the error associated with measurements using the CRDS technique is ≤ 0.5%. The errors in determining the experimental parameters ρ and J can be within 5%. Therefore, an accurate measurement of the ground state population density is crucial. In the scenario when the ground state population density is not known, a second cavity ringdown system can be employed to measure the ground state population.

It should be noted that, in the development of this method, there is no specific restriction on the nature of the energy level *a*, i.e. whether the energy level *a* is a metastable state or a regular optically excited state; therefore, theoretically this method can be used to determine EIECS of any excited level. However, in the case of optically allowed transition levels, there exists a possibility of radiation trapping of the resonance radiation with an increase in the ground state population density, which may affect the EIECS measurement. Another case is that the cascading effect in the high electron energy range also starts to contribute significantly to the population densities of the excited levels. In such cases, the electron impact excitation mechanism may not remain the sole dominant process of excitation. Therefore, one needs to be careful when applying this method to those cases. Nevertheless, the results in this work suggest that this method can be efficiently applied to measure EIECS of metastable energy levels in a low electron energy range. On the other hand, the CRDS technique is capable of making accurate measurements at high pressure and high temperature; therefore the measurement of EIECS using the CRDS method can be done even under extended experimental conditions. The method is independent of the nature of the source of excitation; an electron gun, plasmas, or discharge can be readily incorporated into the CRDS system.

6.7 Conclusions

A new method of measuring the apparent electron impact excitation cross section (EIECS) of atoms has been described. The cavity ringdown spectroscopy (CRDS) measurement of absolute population densities of the energy levels is the key step in the process. Unlike the previous optical methods of measuring EIECS, this method does not use relative emission line intensities. The EIECS is explicitly expressed in an analytic solution of the steady state population rate equations as a function of population number densities that are measured absolutely by CRDS. The method was validated via the determination of EIECS of the metastable 6s6p $^3P_0$ level of Hg and the metastable $2p^5$ 3s $^3P_2$ level of Ne atoms. The results from the current study suggest that the method has potential to be used as an alternative means to measure EIECS, even without the need of a calibration process.

6.8 Acknowledgements

This work is supported by the National Science Foundation through Grant # CBET-1066486.

6.9 References

1. M.H. Phillips, L.W. Anderson, C.C. Lin, Phys. Rev. A 23 (1981) 2751.

2. G.F. Hanne, V. Nickich, M. Sohn, J. Phys. B: At. Mol. Phys. 18 (1985) 2037.

3. A.R. Filippelli, C.C. Lin, L.W. Anderson, J.W. McConkey, Adv. At. Mol. Opt. Phys. 33 (1994) 1.

4. A. Chutjian, D.C. Cartwright, Phys. Rev. A 23 (1981) 2178.

5. K. Blum, Density Matrix Theory and Applications, Plenum, New York, 1981, pp. 37-81.

6. R.O. Jung, J.B. Boffard, L.W. Anderson, C.C. Lin, Phys. Rev. A 80 (2009) 062708 1.

7. T. Hadeishi, Ph.D. Dissertation, University of California, Berkeley, 1962.

8. A.A. Mityureva, N.P. Penkin, Opt. Spektrosk. 55 (1983) 393.

9. C. Wang, P. Sahay, S.T. Scherrer, Phys. Lett. A 375 (2011) 2366.

10. C. Wang, P. Sahay, S. T. Scherrer, J. Anal. At. Spectrom. 27 (2012) 284.

11. R.O. Jung, PhD Dissertation, University of Wisconsin, Madison, 2010.

12. S.D. Rockwood, Phys. Rev. A 8 (1973) 2348.

13. J.N. Bass, R.A. Berg, A.E.S. Green, J. Phys. B: At. Mol. Phys 7 (1974) 1853.

14. M.H. Phillips, L.W. Anderson, C.C. Lin, Phys. Rev. A 32 (1985) 2117.

15. F.A. Sharpton, R.M. st John, C.C. Lin, F.E. Fajen, Phy. Rev. A 2 (1970) 1305.

16. J.B. Boffard, R.O. Jung, C.C. Lin, A.E. Wendt, Plasma Sources Sci. Technol. 18 (2009) 035017 1.

17. NIST Atomic Database: http://physics.nist.gov/PhysRefData/ASD/lines_form.html.

18. M.W. Milatz, L.S. Ornstein, Physica (Utrecht) 2 (1935) 355.

CHAPTER VII

FUTURE RESEARCH RECOMMENDATIONS

7.1 Accomplishment and Future Research Recommendations

The present study demonstrated fundamentals of a novel concept 'Electron impact excitation-cavity ringdown down spectroscopy' (EIE-CRDS). The basic principle of the technique was described in detail and some of the potential applications were demonstrated. The technique was employed for measuring electron impact excitation cross sections in an electron-atom collision process. In the present study, the method was demonstrated by measuring the excitation cross sections of first few excited levels of mercury. Further, the technique was also employed for the purpose of element detection and analysis.

After it has been established in this study that cavity ringdown spectroscopy can be used as an alternative tool to study electron impact excitation process; this technique can be extended to other measurements as well. As an immediate continuation of the present work the following future works are suggested. Subsequently, other applications can also be explored.

Suggested future works.

- Explore the EIE-CRDS technique with different excitation sources.
- To demonstrate the applicability of the EIECS measurement method on other metastable levels.
- Eventually the EIE-CRDS can be used for creating excitation cross section database for different elements.
- Instrument development: To demonstrate *in situ* element detection.
- To extend it for the detection and measurement of other elements, such as Pb, As, Be, etc.

APPENDIX A

A COMPARISON OF EMISSION INTENSITIES OF THE PB, AS, P, CD, MN AND NI TRANSITION LINES OBTAINED IN THIS WORK WITH THOSE IN THE NIST ATOMIC DATABASE

Table A.1 Pb

Pb State	Wavelength (nm)	E_i (cm^{-1}) - E_k (cm^{-1})	Intensity in NIST		Intensity in this work	
			Ab Int.	Rel. I (%)	Ab Int.	Rel. I (%)
I	261.417	7819.26 – 46060.83	900	0.94	555	32.34
I	280.199	10650.32 – 46328.66	25000	26.31	612	35.66
I	283.305	0 – 35287.22	35000	36.84	1270	74.00
I	357.272	21457.79 – 49439.61	35000	36.84	98	5.71
I	363.956	7819.26 – 35287.22	50000	52.63	1019	59.38
I	368.346	7819.26 – 34959.90	70000	73.68	1716	1
I	373.993	21457.79 – 48188.63	25000	26.31	82	4.77
I	405.780	10650.32 – 35287.22	95000	1	1167	68.00

Table A.2 As

As State	Wavelength (nm)	E_i (cm^{-1}) - E_k (cm^{-1})	Intensity in NIST		Intensity in this work	
			Ab Int.	Rel. I (%)	Ab Int.	Rel. I (%)
I	228.812	10914.86 – 54605.49	350	1	515	96.44
I	234.984	10592.66 – 53135.75	350	1	534	1
I	236.967	18647.66 – 60834.94	6	1.71	51	9.55
I	245.653	10914.86 – 51610.39	170	48.57	130	24.34
I	249.261	10592.66 – 50693.89	40	11.42	149	42.57
I	274.500	18186.32 – 54605.49	40	11.42	81	23.41
I	278.022	18647.66 – 54605.49	170	48.57	521	97.56
I	286.044	18186.32 – 53135.75	100	28.57	311	58.23

Table A.3 P

P State	Wavelength (nm)	E_i (cm^{-1}) - E_k (cm^{-1})	Intensity in NIST		Intensity in this work	
			Ab Int.	Rel. I (%)	Ab Int.	Rel. I (%)
I	213.546	11361.02 – 58174.366	400	42.10	190	39.83
I	214.914	11361.02 – 57876.574	400	42.10	52	10.78
I	253.560	18748.01 – 58174.366	950	1	482	1
I	255.326	18722.71 – 57876.574	750	78.94	257	53.31
IV	336.446	226898.14 – 256611.97	570	60.00	246	51.03
IV	337.112	226898.14 – 256553.36	400	42.10	125	25.93

Table A.4 Cd

Cd State	Wavelength (nm)	E_i (cm^{-1}) - E_k (cm^{-1})	Intensity in NIST		Intensity in this work	
			Ab Int.	Rel. I (%)	Ab Int.	Rel. I (%)
II	214.411	0 – 46618.55	1000	66.67	162	4.42
II	226.502	0 – 44136.08	1000	66.67	870	23.74
I	228.802	0 – 43692.47	1500	1	3552	96.94
I	326.105	0 – 30656.13	300	20	3664	1
I	346.620	30650.13 – 59497.89	1000	66.67	897	24.48
I	361.050	31826.99 – 59516.01	1000	66.67	1081	29.50

Table A.5 Mn

Mn State	Wavelength (nm)	E_i (cm^{-1}) - E_k (cm^{-1})	Intensity in NIST		Intensity in this work	
			Ab Int.	Rel. I (%)	Ab Int.	Rel. I (%)
II	257.610	0-38806.67	12000	63.15	3173	1
II	259.373	0 – 38543.08	6200	32.63	2883	90.86
II	260.568	0 – 38366.18	4300	22.63	2108	66.43
I	279.482	0 – 35769.97	6200	32.63	3044	95.93
I	279.827	0 – 35725.85	5100	26.84	2642	83.26
I	280.106	0 – 35689.98	3700	19.47	1624	51.18
II	293.306	9472.97 – 43557.14	1100	5.78	394	12.41
II	293.930	9472.97 – 43484.64	1500	7.89	545	17.17
II	294.920	9472.97 – 43370.51	1900	10.00	684	21.55

Table A.5 (Continued)

I	322.809	17052.29 – 48021.43	1000	5.26	206	6.49
II	344.199	14325.86 – 43370.51	720	3.78	132	4.16
I	353.212	18402.46 – 46706.09	1100	5.78	179	5.64
I	354.780	18531.64 – 46710.15	1300	6.84	237	7.46
I	354.803	18531.64 – 46708.33	110	0.57	241	7.59
I	380.672	17052.29 – 43314.23	3200	16.84	219	6.90
I	382.351	17282.00 – 43428.58	2100	11.05	194	6.11
I	383.436	17451.52 – 43524.08	1300	6.84	117	3.68
I	403.307	0 – 24788.05	19000	1	1671	52.66

Table A.6 Ni

Ni State	Wavelength (nm)	E_i (cm^{-1}) - E_k (cm^{-1})	Intensity in NIST		Intensity in this work	
			Ab Int.	Rel. I (%)	Ab Int.	Rel. I (%)
I	232.003	0 – 43089.578	2600	31.70	176	11.57
I	300.249	204.787 – 33500.822	4000	48.78	885	58.22
I	301.200	3409.937 – 36600.791	3700	45.12	689	45.32
I	305.082	204.787 – 32973.376	3500	42.68	524	34.47
I	305.764	1713.087 – 34408.55	1900	23.17	273	17.96
I	310.155	879.816 – 33112.334	2600	31.70	756	49.73
I	313.411	1713.087 – 33610.890	2900	35.36	411	27.03
I	323.296	0 – 30922.734	1100	13.41	109	7.17
I	336.957	0 – 29668.918	2900	35.36	236	15.52
I	338.057	3409.937 – 32982.260	3300	40.24	375	24.67
I	339.299	204.787 – 29668.918	3300	40.24	449	29.53
I	341.476	204.787 – 29480.989	8200	1	1110	73.02
I	344.626	879.816 – 29888.477	4800	58.53	462	30.39
I	345.847	1713.087 - 30619.414	5000	60.97	412	27.10
I	346.165	204.787 – 29084.456	5000	60.97	590	38.81
I	349.296	879.816 – 29500.676	5500	67.07	678	44.60
I	351.505	879.816 – 29320.762	6600	80.48	819	53.88
I	352.454	204.787 – 28569.203	8200	1	1520	1
I	356.637	3409.937 – 31441.635	5000	60.97	251	16.51
I	361.939	3409.937 – 31031.020	6600	80.48	617	40.59